Advanced Space-division Multiplexing for Optical Communications

Ingerslev, Kasper

Publication date:
2018

Document Version
Publisher's PDF, also known as Version of record

Citation (APA):
Ingerslev, K. (2018). *Advanced Space-division Multiplexing for Optical Communications*. Technical University of Denmark.

PhD thesis

Advanced Space-division Multiplexing for Optical Communications

Author:
Kasper Ingerslev

Supervisors:
Prof. Toshio Morioka
Prof. Karsten Rottwitt

High-Speed Optical Communications
Department of Photonics Engineering
Technical University of Denmark

November 2018

DTU Fotonik
Department of Photonics Engineering

Technical
University of
Denmark

Preface

This PhD thesis is submitted as partial fulfillment of the requirements to obtain the PhD degree at the Technical University of Denmark (DTU). The work contained in this thesis has been carried out at the Department of Photonics Engineering at DTU (DTU Fotonik) in the High-Speed Optical Communications Group, during the period from November 2015 to November 2018. The work has been supervised by Prof. Toshio Morioka, co-supervised by Prof. Karsten Rottwitt and funded by the Danish National Research Foundation (DNRF) Center of Excellence, Silicon Photonics for Optical Communications (SPOC).

Three months of work, from April 2018 through July 2018, was carried out, as an intern at the National Institute of Information and Communications Technology (NICT), Network System Research Institute, Photonic Network System Laboratory in Koganei, Tokyo, Japan. At NICT, I would like to thank Georg Rademacher, Ruben S. Luís, Benjamin J. Puttnam and Werner Klaus for supervision, and for making my stay enjoyable. Furthermore, I would like to thank Yoshinari Awaji and Naoya Wada for making my stay possible.

Much of the work throughout this thesis, concerning Orbital Angular Momentum (OAM) Modes has been done in collaboration with Prof. Siddharth Ramachandran and Patrick Gregg from Boston University, USA, who visited DTU in September 2016. This was a big help for me in getting my work on OAM modes started, and thus I would like to thank them. I would also like to thank Poul Kristensen at OFS Fitel for fabricating the used OAM fibers, and for scientific discussion.

At DTU, I would like to thank my supervisors Prof. Toshio Morioka, and Prof. Karsten Rottwitt and my group leader Prof. Leif Katsuo Oxenløwe. I would like to thank Francesco Da Ros, Michael Galili, and Hao Hu for helping me in the laboratory. Also at DTU, I would like to thank the High-Speed Optical Communications Group and the Fiber Optics, Devices & Nonlinear Effects Group.

Further, I would like to thank the funding agencies Otto Mønsteds Fond, Oticon Fonden and Fabrikant P.A. Fiskers Fond for helping me funding travel during the PhD, and thereby making it possible to participate in conferences. Finally, I would like to thank DNRF for funding this PhD project.

Kasper Ingerslev

Abstract

Single-mode optical fibers are widely used for data transmission, and form the backbone of our communications infrastructure. However, these fibers have a finite capacity, which we are approaching.

The most promising solution to increase the capacity of optical fibers is the use of space-division multiplexing (SDM), where several spatial paths in a single optical fiber are used to enable simultaneous data transmission of several independent data streams for each carrier wavelength.

This thesis examines SDM using orbital angular momentum (OAM) modes, and linearly polarized (LP) modes. A special air-core optical fiber supporting stable propagation of OAM modes is characterized, and used in a communications experiment. This resulted in simultaneous transmission of 12 OAM modes in the air-core fiber, without the need of multiple-input multiple-output signal processing.

Raman amplification of OAM modes in the air-core fiber is explored, using different pumping schemes, and is found to be a solution in order to amplify OAM modes in the transmission fiber.

Finally, the complexity of SDM systems is addressed, through a novel SDM receiver structure, which significantly reduces the number of components needed to receive an SDM signal. The receiver is demonstrated using a system based on LP mode multiplexing in a fiber supporting 3 modes.

Resume

Optiske fibre der kun understøtter en enkelt transversal bølgetype er rygraden i vores kommunikationsinfrastruktur. Disse fibre har dog en endelig kapacitet, som vi nærmer os.

Derfor er der brug for nye optiske fibre, og den mest lovende løsning på kapacitetsproblemet er rumlig multioverføring, hvor flere veje i samme fiber bliver brugt til at overføre uafhængige data på samme tid, og på samme bølgelængde.

Denne afhandling beskæftiger sig med rumlig multioverføring med optiske bølgetyper der har orbitalt angulært moment, samt lineært polariserede bølgetyper. En speciel optisk fiber, med en luftkerne, der understøtter stabil transmission af bølgetyper med orbitalt angulært moment, bliver karakteriseret, og anvendt i et kommunikationseksperiment. Dette resulterer i samtidig datatransmission på 12 bølgetyper med orbitalt angulært moment, uden at der er behov for signalbehandling med flere indgange og flere udgange.

Raman forstærkning af bølgetyperne i denne luftkernefiber bliver undersøgt, med flere forskellige pumpekonfigurationer, og det konkluderes at Ramanforstrækning giver mulighed for at forstærke bølgetyper med orbitalt angulært moment i luftkernefiberen.

Kompleksiteten af kommunikationssystemer der benytter sig af rumlig multioverføring er typisk høj. I denne afhandling præsenteres en ny type modtager til denne type af systemer. Modtageren reducerer antallet af komponenter der kræves for at kunne modtage et rumligt multioverført signal. Den bliver demonstreret i et kommunikationseksperiment hvor der benyttes et system basseret på multioverføring i en optisk fiber der understøtter 3 bølgetyper.

Contents

List of publications

Basis of the thesis

- K. Ingerslev, G. Rademacher, R. S. Luis, B. J. Puttnam, W. Klaus, T. A. Eriksson, S. Shinada, Y. Awaji, R. Maruyama, K. Aikawa, T. Morioka, and N. Wada, "A Scalable SDM Receiver Enabled by Few-Mode Domain Spectral Filtering and LO-Signal Mixing," in *(Submitted to) Optical Fiber Communication Conference,* (Unpublished, 2019).
- K. Ingerslev, G. Rademacher, R. S. Luis, B. J. Puttnam, W. Klaus, S. Shinada, Y. Awaji, K. Rottwitt, T. Morioka, L. K. Oxenløwe, and N. Wada, "Free-Space Few-Mode Kramers-Kronig Receiver," in *Photonics in Switching and Computing (PSC) 2018,* (2018).
- K. Ingerslev, P. Gregg, M. Galili, F. Da Ros, H. Hu, F. Bao, M. A. Usuga Castaneda, P. Kristensen, A. Rubano, L. Marrucci, K. Rottwitt, T. Morioka, S. Ramachandran, and L. K. Oxenløwe, "12 mode, WDM, MIMO-free orbital angular momentum transmission," Optics Express **26**, 20225 (2018).
- K. Ingerslev, P. Gregg, M. Galili, P. Kristensen, S. Ramachandran, K. Rottwitt, T. Morioka, and L. K. Oxenlowe, "Raman amplification of OAM modes," in *4th International Conference on Optical Angular Momentum (ICOAM 2017),* (2017).
- K. Ingerslev, P. Gregg, M. Galili, P. Kristensen, S. Ramachandran, K. Rottwitt, T. Morioka, and L. K. Oxenlowe, "Raman amplification of OAM modes," in *2017 Conference on Lasers and Electro-Optics Europe & European Quantum Electronics Conference (CLEO/Europe-EQEC),* (IEEE, 2017), pp. 1–1.
- K. Ingerslev, P. Gregg, M. Galili, F. Da Ros, H. Hu, F. Bao, M. A. U. Castaneda, P. Kristensen, A. Rubano, L. Marrucci, S. Ramachandran, K. Rottwitt, T. Morioka, and L. K. Oxenløwe, "12 Mode, MIMO-Free OAM Transmission," in *Optical Fiber Communication Conference,* (OSA, 2017), p. M2D.1.

Outside the scope of the thesis

- K. Rottwitt, J. G. Koefoed, K. Ingerslev, and P. Kristensen, "Inter-modal Raman amplification of OAM fiber modes," (Invited)(Submitted to) APL Photonics (2018).

- H. Hu, F. Da Ros, M. Pu, F. Ye, K. Ingerslev, E. Porto da Silva, M. Nooruzzaman, Y. Amma, Y. Sasaki, T. Mizuno, Y. Miyamoto, L. Ottaviano, E. Semenova, P. Guan, D. Zibar, M. Galili, K. Yvind, T. Morioka, and L. K. Oxenløwe, "Single-source chip-based frequency comb enabling extreme parallel data transmission," Nature Photonics **12**, 469–473 (2018).

- D. Cozzolino, D. Bacco, B. Da Lio, K. Ingerslev, Y. Ding, K. Dalgaard, P. Kristensen, M. Galili, K. Rottwitt, S. Ramachandran, and L. K. Oxenløwe, "Fiber-based high-dimensional quantum key distribution with twisted photons," in *CLEO Pacific Rim 2018,* (2018), p. PDP.1.

- D. Cozzolino, D. Bacco, B. Da Lio, K. Ingerslev, Y. Ding, K. Dalgaard, P. Kristensen, M. Galili, K. Rottwitt, S. Ramachandran, and L. K. Oxenløwe, "Fiber based high-dimensional quantum communication with twisted photons," arXiv:1803.10138 (2018).

- J. M. Baumann, K. Ingerslev, Y. Ding, and T. Morioka, "On-chip mode-division-multiplexing extends single-fiber communications capacity," Laser Focus World **54**, 43–46 (2018).

- D. Cozzolino, D. Bacco, K. Ingerslev, Y. Ding, K. Dalgaard, K. Rottwitt, and L. K. Oxenløwe, "High-dimensional quantum key distribution with OAM-fibre," in *4th International Conference on Optical Angular Momentum (ICOAM 2017),* (2017).

- H. Hu, F. Da Ros, F. Ye, M. Pu, K. Ingerslev, E. P. da Silva, M. Nooruzzaman, Y. Amma, Y. Sasaki, T. Mizuno, Y. Miyamoto, L. Ottaviano, E. Semenova, P. Guan, D. Zibar, M. Galili, K. Yvind, L. K. Oxenløwe, and T. Morioka, "Single-Source AlGaAs Frequency Comb Transmitter for 661 Tbit/s Data Transmission in a 30-core Fiber," in *Conference on Lasers and Electro-Optics,* (OSA, 2016), p. JTh4C.1.

- K. Ingerslev, S. H. M. Larsen, and K. Rottwitt, "S-imaging of Bessel-like Beams," in *Australia and New Zealand Conference on Optics and Photonics (ANZCOP 2013),* (2013).

Acronyms

ASE amplified spontaneous emission.

AWG arbitrary waveform generator.

BER bit error rate.

CW continuous wave.

DP dual polarization.

DSP digital signal processing.

ECL external cavity laser.

EDFA erbium doped fiber amplifier.

EVM error vector magnitude.

FEC forward error correction.

FMF few-mode fiber.

FUT fiber under test.

FWHM full width at half maximum.

GMI generalized mutual information.

HD-FEC hard-decision forward error correction.

HOM higher-order mode.

KK Kramers-Kronig.

LDPC low-density parity-check.

LO local oscillator.

LP	linearly polarized.
MDL	mode dependent loss.
MDM	mode-division multiplexing.
MIMO	multiple-input multiple-output.
MMF	multi-mode fiber.
MPI	multipath interference.
ND	neutral density.
OAM	orbital angular momentum.
OSA	optical spectrum analyzer.
OSNR	optical signal to noise ratio.
PBS	polarizing beam splitter.
PD	photodetector.
PDM	polarization division multiplexing.
QAM	quadrature-amplitude modulation.
RF	radio frequency.
SAM	spin angular momentum.
SD-FEC	soft-decision forward error correction.
SDM	space-division multiplexing.
SLM	spatial light modulator.
SMF	single-mode fiber.
SNR	signal to noise ratio.
TDFA	thulium doped fiber amplifier.
TE	transverse electric.
TM	transverse magnetic.
VOA	variable optical attenuator.
WDM	wavelength-division multiplexing.

List of figures

List of tables

Chapter 1

Introduction

The low loss silica optical fiber was first proposed in 1966 [1] and was realized in practice in 1970 [2]. Since then, optical networks have been continuously developed, and the capacities have been increased. Today, optical networks are the backbone of our communications infrastructure, and the high bandwidth of optical fibers have enabled many business models that would otherwise not have been possible, such as services based on video streaming.

During the years, optical communications systems have been improved. Starting from single wavelength systems in the 1980s, the erbium doped fiber amplifier (EDFA) was developed [3], followed by wavelength-division multiplexing (WDM), which was implemented in the 1990s. In the 2000s, higher order modulation, combined with digital coherent technologies has been the enabling technology behind the capacity improvements. While these technologies have increased the amount of data that can be transmitted in the single-mode fiber (SMF), and while this fiber has been continuously developed over the years, in order to reduce loss and tailor dispersion, it has been fundamentally the same fiber.

The Shannon limit [4], relates the achievable information rate to the signal to noise ratio (SNR). Thus, in order to transmit more data, the SNR must be increased. In practice, it is very hard to reduce the noise, which in turn requires an increase in signal power. The optical fiber, however, is a nonlinear medium, and thus a high power signal undergoes a nonlinear phase shift. This gives rise to the nonlinear Shannon limit [5], which can be seen as a compromise between the SNR and the nonlinear distortions. This means that there is a capacity limit for the SMF, and the closer we get to this limit, the harder it is to improve the data-rates [6, 7]. One of the methods for increasing capacities has been to use more of the optical spectrum, expanding outside the C-band, and thereby avoid increasing the power per wavelength. However, any optical fiber has a power limit, where the core of the fiber will fuse, and be permanently destroyed [8]. Thus, the maximum capacity of the SMF will eventually be reached, in the so-called capacity crunch [9, 10], and new optical fibers will be required.

The most promising solution to further increase the transmission capacities in optical fibers is space-division multiplexing (SDM) [11–13]. In SDM systems, multiple spatial propagation paths are used to transmit independent data streams at the same carrier wavelength, in the same fiber. Suitable fibers for SDM are either multi-core fibers [14, 15], where several fiber cores are arranged inside a common cladding or few-mode fibers (FMFs) and multi-mode fibers (MMFs) [16], where a single fiber core is designed to support several orthogonal modes that can carry independent signals. This type of SDM is also known as mode-division multiplexing (MDM). Hybrid few-mode multi-core fibers have also been demonstrated and showed strong potential, currently holding the record for maximum data-rate in a single fiber [17]. Furthermore SDM may also reduce the energy consumption per bit, through SDM resource sharing.

Within MDM, several types of modes can be used as a basis to carry data. Modes are usually split into two classes, vector modes, and linearly polarized (LP) modes. LP modes exist in step-index or graded-index fibers, where the index contrast is weak, and are two-fold degenerate in polarization. It should be mentioned that in this case, vector modes are still the true eigenmodes, however, they appear in bands of near-degenerate modes, which to good approximation can be treated as LP modes.

These modes usually experience significant coupling during fiber propagation, and thus communications systems using higher order LP modes usually rely on multiple-input multiple-output (MIMO) equalization [18].

Alternatively, vector modes can be used to carry data. These modes generally require special optical fibers with e.g. elliptical cores, to break the symmetry [19], or strong refractive index contrasts. However, if these fibers are properly engineered, propagation with very little coupling can be achieved. This is especially true in the case of orbital angular momentum (OAM) modes [20,21], that have been shown to be propagation stable over long distances [22].

In this thesis, MDM is explored, with a focus on OAM modes. The modes of an optical fiber are derived, starting from the Maxwell equations, and an air-core optical fiber designed for OAM modes is characterized numerically and experimentally. A transmission experiment with 12 OAM modes propagating simultaneously in the air-core OAM fiber is performed, and Raman amplification of these modes is investigated. Finally, communications using LP modes is explored through transmission experiments, with a focus on reducing the complexity of MDM systems.

1.1 Overview of thesis

Chapter 2: Contains the derivation of full vectorial modes in optical fibers, starting from Maxwell's equations. The scalar approximation, leading to LP modes is introduced. Finally, OAM modes are introduced, and the transformation from HE and EH modes to OAM modes is presented.

Chapter 3: Presents the air-core OAM fiber. The modes of this fiber are solved, and the properties are discussed. Methods of exciting pure OAM modes in this fiber are presented, and the fiber samples are characterized.

Chapter 4: Presents and characterizes a communications system using 12 OAM modes in the air-core fiber as SDM channels, is presented and characterized.

Chapter 5: Investigates Raman amplification of OAM modes in the air-core fiber. Several experiments are performed, characterizing the Raman interaction between one or several signals in pure OAM modes, and pumps in either pure OAM modes, or superpositions of modes.

Chapter 6: Demonstrates a novel few-mode Kramers-Kronig (KK) receiver, for communications systems using FMF for LP modes. This design reduces the number of components required to build a coherent few-mode receiver, by utilizing SDM resource sharing.

Chapter 7: Concludes the thesis.

Chapter 2

Modes in optical fibers

This chapter examines the topic of transverse modes in optical fibers, starting from the Maxwell equations, the eigenvalue equations for light propagation in optical fibers are derived. The eigenmode problem is solved analytically in the scalar case. In the full vectorial case, the equations are discretized, allowing numerical solutions for any refractive index profile with cylindrical symmetry. Finally, the concept of orbital angular momentum (OAM) modes is explained.

2.1 Wave guide theory

2.1.1 Basic formulation

The propagation of light in optical fibers is governed by the Maxwell equations in matter [23],

$$\nabla \cdot \boldsymbol{D} = \rho_{\mathrm{f}}, \tag{2.1}$$

$$\nabla \cdot \boldsymbol{B} = 0, \tag{2.2}$$

$$\nabla \times \boldsymbol{E} = -\partial_t \boldsymbol{B}, \tag{2.3}$$

$$\nabla \times \boldsymbol{H} = \boldsymbol{J}_{\mathrm{f}} + \partial_t \boldsymbol{D}, \tag{2.4}$$

where $\boldsymbol{E}$ and $\boldsymbol{H}$ are the electric and magnetic vector fields, respectively. $\boldsymbol{D}$ is the electric displacement field and $\boldsymbol{B}$ is the magnetic induction. ρ_{f} is the free charge density, and $\boldsymbol{J}_{\mathrm{f}}$ is the free current density. Bold symbols denote vector quantities, while t is time, and ∂_t denotes partial differentiation with respect to time. Assuming a linear, isotropic material, the relationships between the $\boldsymbol{E}$ and $\boldsymbol{D}$ fields, and the $\boldsymbol{B}$ and $\boldsymbol{H}$ fields, respectively, are given by the constitutive relations

$$\boldsymbol{D} = \varepsilon_0 \varepsilon \boldsymbol{E}, \tag{2.5}$$

$$\boldsymbol{H} = \frac{1}{\mu_0 \mu} \boldsymbol{B}, \tag{2.6}$$

where ε is the permittivity, and μ is the permeability, and $\varepsilon_0 = 8.854 \times 10^{-12}\,\mathrm{F/m}$ is the vacuum permittivity and $\mu_0 = 4\pi \times 10^{-7}\,\mathrm{H/m}$ is the vacuum permeability. Restricting the analysis to dielectric media, the permeability is unity, and there are no free charges and free currents

$$\mu = 1, \tag{2.7}$$
$$\rho_\mathrm{f} = \boldsymbol{J}_\mathrm{f} = 0. \tag{2.8}$$

Thus, the Maxwell equations can now be written in terms of $\boldsymbol{E}$ and $\boldsymbol{H}$, when assuming that ε has no time dependence

$$\nabla \cdot (\varepsilon \boldsymbol{E}) = 0, \tag{2.9}$$
$$\nabla \cdot \boldsymbol{H} = 0, \tag{2.10}$$
$$\nabla \times \boldsymbol{E} = -\mu_0 \partial_t \boldsymbol{H}, \tag{2.11}$$
$$\nabla \times \boldsymbol{H} = \varepsilon_0 \varepsilon \partial_t \boldsymbol{E}. \tag{2.12}$$

These equations can be solved in order to determine the electric field distribution in optical fibers [24]. In order to do this, the equations are translated to the frequency domain, by assuming a harmonic time dependence

$$\boldsymbol{E}(\boldsymbol{r}, t) = \boldsymbol{E}(\boldsymbol{r}) \exp(-i\omega t), \tag{2.13}$$
$$\boldsymbol{H}(\boldsymbol{r}, t) = \boldsymbol{H}(\boldsymbol{r}) \exp(-i\omega t), \tag{2.14}$$

the time derivatives in the Maxwell equations can be done explicitly. This leads to

$$\nabla \times \boldsymbol{E} = i\omega\mu_0 \boldsymbol{H}, \tag{2.15}$$
$$\nabla \times \boldsymbol{H} = -i\omega\varepsilon_0 \varepsilon \boldsymbol{E}. \tag{2.16}$$

Since the electric field can be calculated from the magnetic field, and vice versa, it is advantageous to restrict calculations to one of them. To make this choice, the boundary conditions for the $\boldsymbol{E}$ and the $\boldsymbol{H}$ field are examined

$$\varepsilon_1 E_1^\perp = \varepsilon_2 E_2^\perp, \qquad E_1^\| = E_2^\|, \tag{2.17}$$

$$\mu_1 H_1^\perp = \mu_2 H_2^\perp, \qquad H_1^\| = H_2^\|, \tag{2.18}$$

where $\perp$ denotes the field component that is perpendicular to the boundary, and $\|$ denotes the field component that is parallel to the boundary [23]. From these equations, it is seen that the $\boldsymbol{H}$ field is continuous across a step in ε, while the $\boldsymbol{E}$ field is discontinuous. Therefore the $\boldsymbol{H}$ field is chosen. An eigenvalue equation for $\boldsymbol{H}$ is obtained by taking the curl of both sides of Eq. (2.16)

$$\nabla \times \nabla \times \boldsymbol{H} = -i\omega\varepsilon_0 \nabla \times (\varepsilon \boldsymbol{E}). \tag{2.19}$$

Exploiting the relation,

$$\nabla \times (\varepsilon \boldsymbol{E}) = \varepsilon(\nabla \times \boldsymbol{E}) + \nabla\varepsilon \times \boldsymbol{E}, \tag{2.20}$$

and Eq. (2.15) is used to eliminate the $\nabla \times \boldsymbol{E}$ term

$$\nabla \times \nabla \times \boldsymbol{H} = k_0^2 \varepsilon \boldsymbol{H} - i\omega\varepsilon_0(\nabla\varepsilon \times \boldsymbol{E}), \tag{2.21}$$

where it is used that $\varepsilon_0\mu_0 = 1/c^2$, where c is the speed of light in vacuum, and $k_0 = \omega/c$. Now Eq. (2.16) is used to eliminate $\boldsymbol{E}$

$$\nabla \times \nabla \times \boldsymbol{H} = k_0^2 \varepsilon \boldsymbol{H} + \frac{\nabla\varepsilon}{\varepsilon} \times \nabla \times \boldsymbol{H}. \tag{2.22}$$

The vector identity

$$\nabla \times \nabla \times \boldsymbol{H} = \nabla(\nabla \cdot \boldsymbol{H}) - \nabla^2 \boldsymbol{H}, \tag{2.23}$$

can be used with Eq. (2.10) to get

$$-\nabla^2 \boldsymbol{H} = k_0^2 \varepsilon \boldsymbol{H} + \frac{\nabla\varepsilon}{\varepsilon} \times \nabla \times \boldsymbol{H}. \tag{2.24}$$

In addition, a straight waveguide is assumed, which leads to a known z dependence of the fields

$$\boldsymbol{H} = \boldsymbol{H}_\perp \exp(i\beta z - i\omega t), \tag{2.25}$$

where β is the propagation constant in the z direction. As with the time derivatives, this allows the z derivative on the left side of Eq. (2.24) to be done explicitly

$$\nabla_\perp^2 \boldsymbol{H} + k_0^2 \varepsilon \boldsymbol{H} + \frac{\nabla\varepsilon}{\varepsilon} \times \nabla \times \boldsymbol{H} = \beta^2 \boldsymbol{H}. \tag{2.26}$$

To continue, it is convenient to expand $\boldsymbol{H}$ in components, and thus, a choice of coordinate system is needed. In this case, a straight waveguide with azimuthal symmetry is studied, and this assumption is mathematically stated as $\partial_\phi\varepsilon = \partial_z\varepsilon = 0$. In order to study this case, cylindrical coordinates are chosen, such that

$$\boldsymbol{H} = \begin{bmatrix} H_r \\ H_\phi \\ H_z \end{bmatrix}. \tag{2.27}$$

It is noted that this assumption excludes fibers such as photonic crystal fibers and polarization maintaining fibers, but simplifies the problem. This leads to the expansion

$$\begin{aligned} &\begin{bmatrix} \frac{1}{r}\partial_r\left(r\partial_r H_r\right) + \frac{1}{r^2}\partial_\phi^2 H_r - \frac{H_r}{r^2} - \frac{2}{r^2}\partial_\phi H_\phi \\ \frac{1}{r}\partial_r\left(r\partial_r H_\phi\right) + \frac{1}{r^2}\partial_\phi^2 H_\phi - \frac{H_\phi}{r^2} + \frac{2}{r^2}\partial_\phi H_r \\ \frac{1}{r}\partial_r\left(r\partial_r H_z\right) + \frac{1}{r^2}\partial_\phi^2 H_z \end{bmatrix} + k_0^2\varepsilon \begin{bmatrix} H_r \\ H_\phi \\ H_z \end{bmatrix} \\ &\qquad + \frac{1}{\varepsilon}\begin{bmatrix} 0 \\ -\partial_r\varepsilon\frac{1}{r}\left(\partial_r(rH_\phi) - \partial_\phi H_r\right) \\ \partial_r\varepsilon\left(\partial_z H_r - \partial_r H_z\right) \end{bmatrix} = \beta^2 \begin{bmatrix} H_r \\ H_\phi \\ H_z \end{bmatrix}. \end{aligned} \tag{2.28}$$

The 6 fields (E and H in 3 dimensions), are uniquely determined through two of these [25]. H_r and H_ϕ are chosen, because they decouple from H_z, allowing calculation of H_r and

H_ϕ without calculating H_z. Finally, the fields radial and angular dependence must be separated. This is done as

$$\Psi = R(r)\Phi(\phi), \tag{2.29}$$

where Ψ represents any field component, $R(r)$ is the radial dependence and $\Phi(\phi)$ is the angular dependence. The angular dependence, and the differential of the angular dependence, must be 2π periodic, and can therefore be taken as either

$$\Phi(\phi) = \cos(m\phi), \qquad \text{or} \qquad \Phi(\phi) = \sin(m\phi), \tag{2.30}$$

where m is an integer. It is seen that to ensure separation of the variables, the choice of either sin or cos must be opposite for H_r and H_ϕ, respectively. This choice simply leads to a rotation of the mode, and thus a degeneracy, since an azimuthal symmetric fiber is assumed. Thus $\partial_\phi^2\Phi = -m^2\Phi$ and $\partial_\phi\Phi = -m\Phi$ in the cosine case or $\partial_\phi\Phi = m\Phi$ in the sine case. Using this, one arrives at the final full-vectorial eigenvalue equations for the $\boldsymbol{H}$ field

$$\partial_r^2 H_r + \frac{1}{r}\partial_r H_r - \frac{m^2+1}{r^2}H_r \pm \frac{2m}{r^2}H_\phi + k_0^2\varepsilon H_r = \beta^2 H_r, \tag{2.31}$$

and

$$\partial_r^2 H_\phi + \frac{1}{r}\partial_r H_\phi - \frac{m^2+1}{r^2}H_\phi \pm \frac{2m}{r^2}H_r + k_0^2\varepsilon H_\phi + \frac{\partial_r\varepsilon}{\varepsilon r}\left[\pm m H_r - H_\phi - r\partial_r H_\phi\right] = \beta^2 H_\phi, \tag{2.32}$$

where the top sign $(+)$ corresponds to H_r having a sine dependence, and H_ϕ having a cosine dependence, while the bottom $(-)$ sign corresponds to H_r having a cosine dependence, and H_ϕ having a sine dependence. When these field components are calculated, one can calculate the four remaining field components using the following equations [25]

$$H_z = \frac{i}{\beta}\left(\frac{1}{r}\partial_r(rH_r) \mp \frac{m}{r}H_\phi\right), \tag{2.33}$$

$$E_r = \frac{i}{\omega\varepsilon_0\varepsilon}\left(\frac{\pm m}{r}H_z - i\beta H_\phi\right), \tag{2.34}$$

$$E_\phi = \frac{i}{\omega\varepsilon_0\varepsilon}\left(i\beta H_r - \partial_r H_z\right), \tag{2.35}$$

$$E_z = \frac{i}{\beta}\left(E_r\frac{\partial_r\varepsilon}{\varepsilon} + \frac{1}{r}[\partial_r(rE_r) \pm mE_\phi]\right). \tag{2.36}$$

In addition to the field equations, boundary conditions are needed in order to obtain a solution. By definition, the field strength of a guided mode, must be zero far away from the fiber core. At $r = 0$, the boundary conditions for a fiber with cylindrical symmetry are [26]

$$\partial_r H_r(0) = \partial_r H_\phi(0) = 0, \qquad \text{for} \qquad m = 1, \tag{2.37}$$

$$H_r(0) = H_\phi(0) = 0, \qquad \text{for} \qquad m \neq 1. \tag{2.38}$$

The solutions to this set of equations are known as fiber modes, and are typically divided into transverse electric (TE) modes, where $E_z = 0$, transverse magnetic (TM) modes, where $H_z = 0$, and hybrid (HE and EH) modes, where none of the field components are zero. TE and TM modes only exist for $m = 0$. This finalizes the derivation of the equations for a straight, dielectric waveguide, with cylindrical symmetry.

2.1.2 Scalar approximation

If the fiber is assumed to have a weak index contrast, such that $\partial_r \varepsilon \approx 0$ it is possible to simplify the equations, by applying the so-called scalar approximation.

Starting from Eq. (2.26), it is seen that by applying the scalar approximation, the entire $\frac{\nabla\varepsilon}{\varepsilon} \times \nabla \times \boldsymbol{H}$ term vanishes. Thus the equation reduces to

$$\nabla_\perp^2 \Psi + k_0^2 \varepsilon \Psi = \beta^2 \Psi, \tag{2.39}$$

where $\boldsymbol{H}$ has been replaced by Ψ, since the exact same equation can be derived for the $\boldsymbol{E}$ field. It is noted that this also results in the $\boldsymbol{E}$ field now being continuous. As previously done, this can be written in cylindrical coordinates

$$\partial_r^2 \Psi + \frac{1}{r} \partial_r \Psi + \frac{1}{r^2} \partial_\phi^2 \Psi + k_0^2 \varepsilon \Psi = \beta^2 \Psi. \tag{2.40}$$

And as in the full-vectorial case, the solution is separated as shown in Eq. (2.29), leading to

$$\partial_r^2 R + \frac{1}{r} \partial_r R - \frac{m^2}{r^2} R + k_0^2 \varepsilon R = \beta^2 R. \tag{2.41}$$

This equation can be solved analytically for a fiber with a single step-index, but it can also be solved, like the full vectorial version, using the finite difference method, for a fiber with any index profile. In the step-index case, the solution is split into two, one in the core, and one in the cladding. To do this, the new variables κ and σ are introduced as

$$\kappa = \sqrt{k_0^2 \varepsilon_c - \beta^2}, \qquad \sigma = \sqrt{\beta^2 - k_0^2 \varepsilon_{cl}}, \tag{2.42}$$

where ε_c and ε_{cl} are the core and cladding dielectric constants, respectively. This leads to

$$r^2 \partial_r^2 R + r \partial_r R + (r^2 \kappa^2 - m^2) R + k_0^2 \varepsilon R = \beta^2 R, \quad 0 \leq r < a, \tag{2.43}$$

$$r^2 \partial_r^2 R + r \partial_r R - (r^2 \sigma^2 + m^2) R + k_0^2 \varepsilon R = \beta^2 R, \quad r > a, \tag{2.44}$$

where a is the core radius. These equations are recognized as forms of Bessel's equation, which has Bessel functions as solutions. By requiring that the mode has finite energy, the core solution must be finite for $r = 0$ and the cladding solution must go to zero for $r \to \infty$. Therefore the solution becomes

$$\Psi = A J_m(\kappa r) \Phi(\phi), \quad 0 \leq r < a, \qquad \Psi = B K_m(\sigma r) \Phi(\phi), \quad r > a, \tag{2.45}$$

where J_m is the Bessel function of the first kind, and K_m is the modified Bessel function of the second kind. The final problem is to find corresponding values of κ and σ, and thus

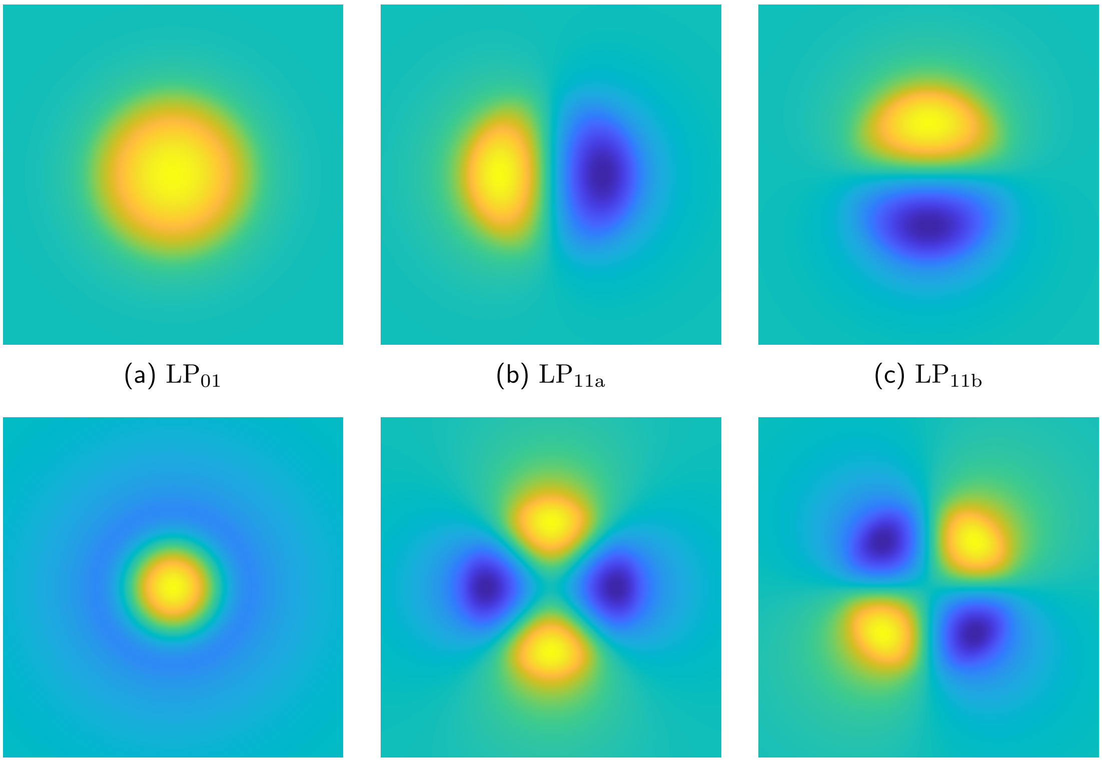
(a) LP_{01} (b) $\mathrm{LP}_{11\mathrm{a}}$ (c) $\mathrm{LP}_{11\mathrm{b}}$

(d) LP_{02} (e) $\mathrm{LP}_{21\mathrm{a}}$ (f) $\mathrm{LP}_{21\mathrm{b}}$

Figure 2.1: Simulated field distributions of the first 6 LP modes in a step-index fiber. Each of these modes are two-fold degenerate in polarization.

finding β. This can be done by requiring the fields to be continuous and differentiable across the boundary between the core and the cladding, which leads to

$$\frac{\kappa J_{m-1}(\kappa a)}{J_m(\kappa a)} = -\frac{\sigma K_{m-1}(\sigma a)}{K_m(\sigma a)}. \tag{2.46}$$

Thus, one can calculate β from the fiber parameters, by using Eq. (2.42) and Eq. (2.46). The field distributions can then be found by using Eq. (2.45). This leads to the so-called linearly polarized (LP) modes, where the LP_{ml} mode corresponds to the solution to the problem with the used m value and l zero crossings. The field distributions of the first 6 LP modes in a step-index fiber are shown in Fig. 2.1.

2.1.3 Solving modes for a measured refractive index profile

In practice, the designed refractive index profile may deviate slightly from the actual produced refractive index profile. This happens when e.g. when dopants diffuse, creating rounded index steps. Therefore, the refractive index profile of a fiber or a preform is measured, and the guided modes must be solved on the basis of the measurement results, rather than the idealized design profile. This is typically done using the finite difference frequency domain method. In order to use this method, the eigenvalue equations, Eq. (2.31) and Eq. (2.32) need to be discretized. Thus, the following finite differences are applied [27]

$$\partial_r \Psi = \frac{\Psi(r+\Delta r) - \Psi(r-\Delta r)}{2\Delta r}, \tag{2.47}$$

$$\partial_r^2 \Psi = \frac{\Psi(r+\Delta r) + \Psi(r-\Delta r) - 2\Psi(r)}{(\Delta r)^2}, \tag{2.48}$$

where Ψ can be any field component. Transferring these to a grid with i points and step size $\Delta r = h$, yields

$$\partial_r \Psi = \frac{\Psi_{(i+1)} - \Psi_{(i-1)}}{2h}, \tag{2.49}$$

$$\partial_r^2 \Psi = \frac{\Psi_{(i+1)} + \Psi_{(i-1)} - 2\Psi_{(i)}}{h^2}. \tag{2.50}$$

The discretization for Eq. (2.31) then becomes

$$\begin{aligned}\left[\frac{1}{h^2} + \frac{1}{2hr_{(i)}}\right] H_{r,(i+1)} + \left[\frac{1}{h^2} - \frac{1}{2hr_{(i)}}\right] H_{r,(i-1)} \\ + \left[k_0^2 \varepsilon_{(i)} - \frac{m^2+1}{r_{(i)}^2} - \frac{2}{h^2}\right] H_{r,(i)} \pm \frac{2m}{r_{(i)}^2} H_{\phi,(i)} = \beta^2 H_{r,(i)}.\end{aligned} \tag{2.51}$$

When discretizing Eq. (2.32) the term with the ε derivative, also needs to be discretized. The other terms are the same as before, except now H_r and H_ϕ has swapped places. Thus, the discretization for Eq. (2.32) becomes

$$\begin{aligned}\left[\frac{1}{h^2} + \frac{1}{2hr_{(i)}} - \frac{\varepsilon_{(i+1)} - \varepsilon_{(i-1)}}{4h^2\varepsilon_{(i)}}\right] H_{\phi,(i+1)} + \left[\frac{1}{h^2} - \frac{1}{2hr_{(i)}} + \frac{\varepsilon_{(i+1)} - \varepsilon_{(i-1)}}{4h^2\varepsilon_{(i)}}\right] H_{\phi,(i-1)} \\ + \left[k_0^2 \varepsilon_{(i)} - \frac{m^2+1}{r_{(i)}^2} - \frac{2}{h^2} - \frac{\varepsilon_{(i+1)} - \varepsilon_{(i-1)}}{2h\varepsilon_{(i)} r_{(i)}}\right] H_{\phi,(i)} \\ \pm \frac{m}{r_{(i)}} \left[\frac{2}{r_{(i)}} + \frac{\varepsilon_{(i+1)} - \varepsilon_{(i-1)}}{2h\varepsilon_{(i)}}\right] H_{r,(i)} = \beta^2 H_{\phi,(i)}.\end{aligned} \tag{2.52}$$

It is seen that in a given point, the equations depend on the previous, and the following point. This obviously gives complications when treating the last point i_{end} and the first point i_1. Provided that the mode is guided, and that the numerical domain is big enough $\Psi_{(i_{\text{end}}+1)} = 0$ in addition, discretization of Eqs. (2.37) and (2.38) yields that if $m = 1$ then $\Psi_0 = \Psi_1$ and if $m \neq 1$ then $\Psi_0 = 0$. For ε, it is assumed that $\varepsilon_0 = \varepsilon_1$ and $\varepsilon_{\text{end}+1} = \varepsilon_{\text{end}}$.

Using the boundary conditions and Eqs. (2.51) and (2.52) it is possible to set up a discretization matrix for the problem. This has the form

$$\begin{bmatrix} \alpha_{r,(1)} & \alpha^{+}_{r,(1)} & 0 & 0 & 0 & \dots & \alpha_{\phi,(1)} & 0 & 0 & 0 & 0 \\ \alpha^{-}_{r,(2)} & \alpha_{r,(2)} & \alpha^{+}_{r,(2)} & 0 & 0 & \cdots & 0 & \alpha_{\phi,(2)} & 0 & 0 & 0 \\ 0 & \ddots & \ddots & \ddots & 0 & \cdots & 0 & 0 & \ddots & 0 & 0 \\ 0 & 0 & \alpha^{-}_{r,(i)} & \alpha_{r,(i)} & \alpha^{+}_{r,(i)} & \cdots & 0 & 0 & 0 & \alpha_{\phi,(i)} & 0 \\ \vdots & \vdots & \vdots & \vdots & \vdots & & \vdots & \vdots & \vdots & \vdots & \vdots \\ \beta_{\phi,(1)} & \beta^{+}_{\phi,(1)} & 0 & 0 & 0 & \dots & \beta_{r,(1)} & 0 & 0 & 0 & 0 \\ \beta^{-}_{\phi,(2)} & \beta_{\phi,(2)} & \beta^{+}_{\phi,(2)} & 0 & 0 & \cdots & 0 & \beta_{r,(2)} & 0 & 0 & 0 \\ 0 & \ddots & \ddots & \ddots & 0 & \cdots & 0 & 0 & \ddots & 0 & 0 \\ 0 & 0 & \beta^{-}_{\phi,(i)} & \beta_{\phi,(i)} & \beta^{+}_{\phi,(i)} & \cdots & 0 & 0 & 0 & \beta_{r,(i)} & 0 \end{bmatrix} \begin{bmatrix} H_{r,(1)} \\ H_{r,(2)} \\ \vdots \\ H_{r,(i)} \\ \vdots \\ H_{\phi,(1)} \\ H_{\phi,(2)} \\ \vdots \\ H_{\phi,(i)} \end{bmatrix}, \tag{2.53}$$

where

$$\alpha_{r,(i)} = k_0^2 \varepsilon_{(i)} - \frac{m^2+1}{r_{(i)}^2} - \frac{2}{h^2}, \tag{2.54}$$

$$\alpha^{+}_{r,(i)} = \frac{1}{h^2} + \frac{1}{2hr_{(i)}}, \tag{2.55}$$

$$\alpha^{-}_{r,(i)} = \frac{1}{h^2} - \frac{1}{2hr_{(i)}}, \tag{2.56}$$

$$\alpha_{\phi,(i)} = \pm \frac{2m}{r_{(i)}^2}, \tag{2.57}$$

$$\beta_{\phi,(i)} = k_0^2 \varepsilon_{(i)} - \frac{m^2+1}{r_{(i)}^2} - \frac{2}{h^2} - \frac{\varepsilon_{(i+1)} - \varepsilon_{(i-1)}}{2h\varepsilon_{(i)} r_{(i)}}, \tag{2.58}$$

$$\beta^{+}_{\phi,(i)} = \frac{1}{h^2} + \frac{1}{2hr_{(i)}} - \frac{\varepsilon_{(i+1)} - \varepsilon_{(i-1)}}{4h^2 \varepsilon_{(i)}}, \tag{2.59}$$

$$\beta^{-}_{\phi,(i)} = \frac{1}{h^2} - \frac{1}{2hr_{(i)}} + \frac{\varepsilon_{(i+1)} - \varepsilon_{(i-1)}}{4h^2 \varepsilon_{(i)}}, \tag{2.60}$$

$$\beta_{r,(i)} = \pm \frac{m}{r_{(i)}} \left[\frac{2}{r_{(i)}} + \frac{\varepsilon_{(i+1)} - \varepsilon_{(i-1)}}{2h\varepsilon_{(i)}} \right]. \tag{2.61}$$

However, if modes with $m = 1$ are chosen, then α and β are adjusted such that

$$\alpha_{r,(1)} = \beta_{\phi,(1)} = k_0^2 \varepsilon_{(i)} - \frac{m^2+1}{r_{(i)}^2} - \frac{1}{h^2} - \frac{1}{2hr_{(i)}} \qquad \text{if} \qquad m = 1. \tag{2.62}$$

The generated discretization matrix is solved in e.g. Matlab, and is the basis for several of the fiber characteristics presented in Ch. 3.

2.2 OAM modes

It was experimentally demonstrated in 1936 [28], based on theoretical predictions from 1909 [29] that light can carry angular momentum. This type of angular momentum is known as spin angular momentum (SAM), typically denoted S, or in optics, simply circular polarization, here denoted

$$\sigma^{\pm} = \frac{1}{\sqrt{2}} \left(\hat{x} \pm i\hat{y} \right), \tag{2.63}$$

where $\hat{x}$ and $\hat{y}$ are unit vectors in the Cartesian coordinate system.

Much later, in 1992, it was further demonstrated that a beam with a phase dependence of

$$\boldsymbol{E}(r, \phi) \propto \exp(iL\phi), \tag{2.64}$$

carries an OAM of $L\hbar$ per photon [30]. This helical phase profile is the defining feature of an OAM mode. The total angular momentum of a light beam is thus

$$J = L + S, \tag{2.65}$$

as is also known from atomic physics [30].

In free-space, and in the paraxial approximation, L and S are separable [31], although this is not the case in general. In some cases, SAM and OAM may couple through spin-orbit interaction [32]. This can happen at e.g. large refractive index steps in optical waveguides, or in high numerical aperture beams, resulting from tight focusing.

2.2.1 From HE and EH modes to OAM modes

As described in Sec. 2.1, the HE and EH modes are degenerate in pairs with identical radial dependence, and either $\sin(m\phi)$ or $\cos(m\phi)$ radial dependence. This difference in radial dependence corresponds to a rotation, leading to two degenerate modes, with orthogonal local polarization everywhere in the transverse plane. Since the fields are real, the local polarization is linear, i.e. the x and y components of the electrical field are in phase, such that the temporal evolution of the electrical field in a given spatial point is linear.

In order to go from these modes, to OAM modes, i.e. modes with a $\exp(iL\phi)$ phase dependence, the basis for the polarization is changed as in Eq. (2.63). This leads to the following superpositions

$$\text{OAM}, \text{a}^{\pm}_{L,m} = \text{HE}^{\text{e}}_{L+1,m} \pm i\text{HE}^{\text{o}}_{L+1,m}, \tag{2.66}$$

$$\text{OAM}, \text{aa}^{\pm}_{L,m} = \text{EH}^{\text{e}}_{L-1,m} \pm i\text{EH}^{\text{o}}_{L-1,m}, \tag{2.67}$$

where $\text{OAM}, \text{a}^{\pm}_{L,m}$ denotes the spin-orbit aligned OAM modes, indicating that L and σ has the same sign, and $\text{OAM}, \text{aa}^{\pm}_{L,m}$ denotes the spin-orbit anti-aligned OAM modes. These superpositions are illustrated in Fig. 2.2. In this work, only modes with a single ring are used, thus setting $m = 1$. Additionally it is noted that $\text{EH}_{0,m}$ modes do not exist, and thus for $L = \pm 1$ the anti-aligned modes do not exist. Fig. 2.2 also illustrates how the LP_{11} modes are created as superpositions of the TM_{01}, $\text{HE}^{\text{e}}_{21}$, $\text{HE}^{\text{o}}_{21}$, and TE_{01} vector modes. Note that the $\text{HE}^{\text{e}}_{21}$ and $\text{HE}^{\text{o}}_{21}$ modes are degenerate, and that the transformation to OAM modes is simply a basis change, from linear to circular polarization, and thus the OAM modes are true vector modes. The LP_{11} modes, on the other hand, are superpositions of non-degenerate vector modes, and are therefore not propagation stable, and are not solutions to the full-vectorial eigenvalue problem.

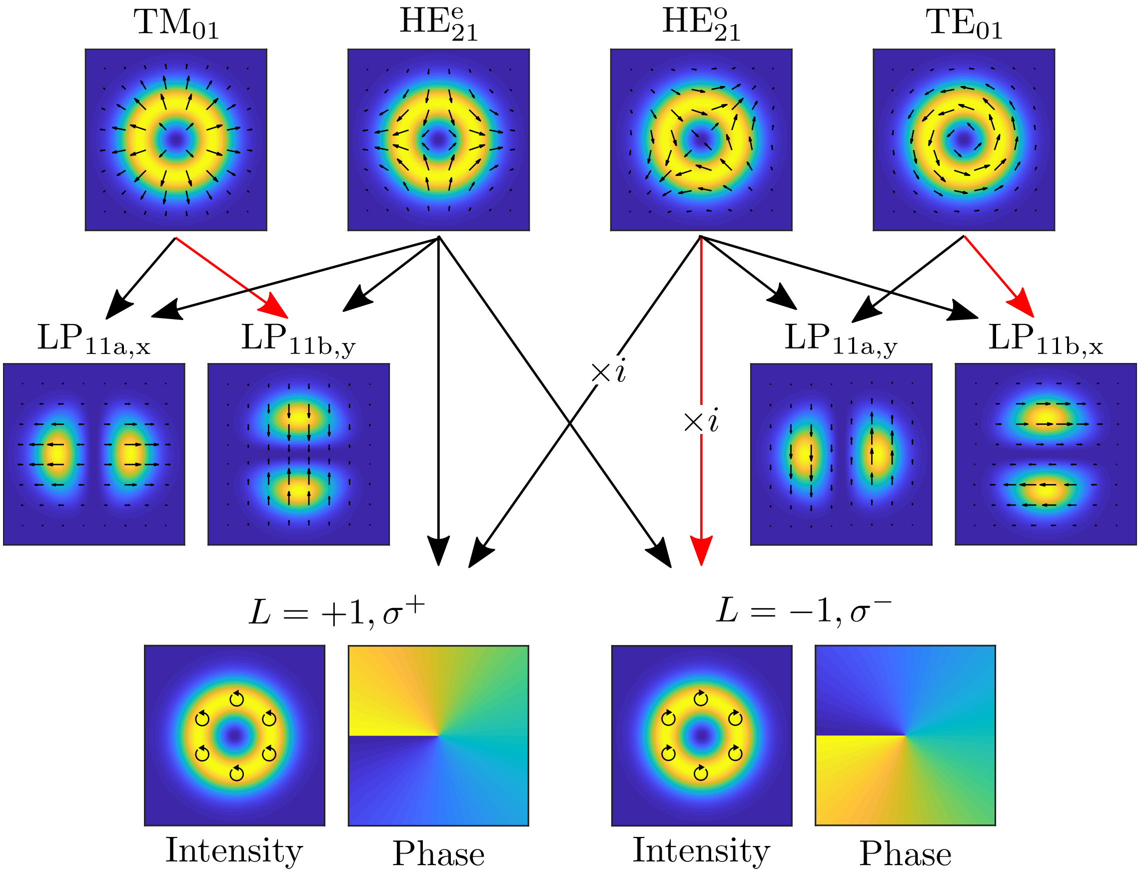

Figure 2.2: Illustration of how superpositions of the TM_{01}, HE^e_{21}, HE^o_{21}, and TE_{01} vector modes, create the LP_{11} modes, and how a basis change from linear to circular polarization transforms the HE_{21} modes to OAM modes. Black arrows indicates addition, and red arrows indicates subtraction.

Chapter 3

Air-core OAM fiber

This chapter briefly explains the history of OAM modes in optical fibers, before moving on to analyze the air-core OAM fiber, used throughout this thesis, in detail.

The modes of the air-core OAM fiber are solved numerically, and experimental setups for excitation of OAM modes in this fiber are presented and analyzed using Fourier optics. Finally, the fiber samples are characterized experimentally.

3.1 Introduction

While standard multi-mode fibers (MMFs) can guide hundreds of modes, including the HE and EH modes that form OAM modes, these fibers do not allow the modes to propagate stably. This happens because the HE and EH modes are near degenerate, thus forming LP modes. In order to achieve stable propagation of OAM modes, the near-degeneracy must be broken. This has been achieved in several optical fibers with ring-cores, and was first demonstrated with the "Vortex" fiber [33]. The Vortex fiber was initially designed for stable propagation of the TE_{01} and TM_{01} modes. However, breaking the degeneracy of the LP_{11}, group, also means that the HE_{21} mode becomes propagation stable, which led to the realization that the Vortex fiber can guide OAM modes [34]. This fiber went on to be used in the first OAM based fiber communications system [35]. Other groups have also performed communications experiments in similar fibers [36], demonstrating that these modes are propagation stable on the order of kilometers.

While these experiments have utilized OAM modes, the multiplicity has been limited, and thus other fiber designs have been developed, increasing the number of guided OAM modes. To achieve this, so-called air-core fibers have been developed. These fibers guide light in a doped ring core, using a central air-hole to provide a large refractive index contrast, maximizing the number of guided OAM orders, without increasing the number of radial mode orders m. This principle was first shown in [37], demonstrating 36 states from $L = 0$ to $L = \pm 9$, however this was achieved in 85 cm of fiber. In [38], the air-core fiber principle was also used, creating a fiber that guides $L = \pm 5$, $L = \pm 6$ and $L = \pm 7$ leading to a total of 12 OAM modes over a distance of 1.2 km. This design was further developed into a fiber supporting 24 OAM modes, by making the guiding ring thinner and increasing the diameter [39]. However, this results in significant spin-orbit coupling, such that L and σ are no longer independent variables. This means that while this fiber design can propagate more modes, it requires more equipment to excite a pure eigenmode, and therefore it is impractical for mode-division multiplexing (MDM).

3.2 Modes in the air-core OAM fiber

In this thesis, several experiments have been performed using the air-core fiber, manufactured by OFS-fitel Denmark [38]. This section describes the fiber design and properties in detail. The measured refractive index profile of the air-core fiber is plotted in Fig. 3.1.

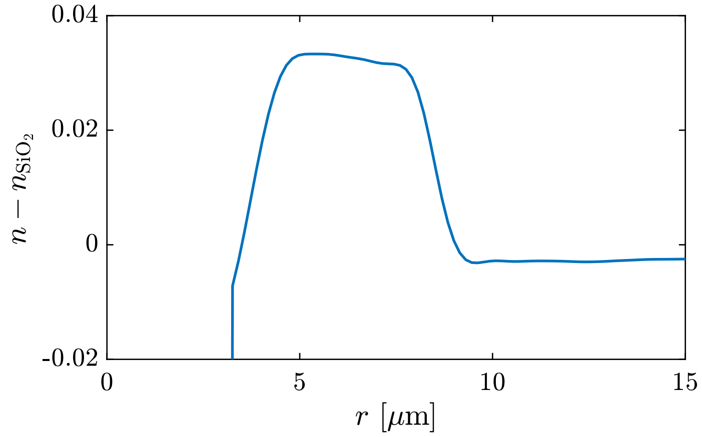

Figure 3.1: Refractive index profile of the air-core OAM fiber. Provided by Patrick Gregg.

By using the theory described in Sec. 2.1.3, some of the fiber properties can be calculated. In Fig. 3.2 the calculated effective refractive indices n_{eff} of the guided modes in the air-core fiber are shown, as a function of wavelength. The colored lines denote the desired OAM modes, while the dashed black lines denote other guided modes in the fiber. The desired 12 modes are the $L = \pm 5, \sigma^{\pm}$, $L = \pm 5, \sigma^{\mp}$, $L = \pm 6, \sigma^{\pm}$, $L = \pm 6, \sigma^{\mp}$, $L = \pm 7, \sigma^{\pm}$, and $L = \pm 7, \sigma^{\mp}$. The modes come in degenerate pairs, and thus only 6 lines are shown. It is seen that the aligned and anti-aligned modes with a given topological charge, L have similar refractive indices, while modes with different $|L|$ show a large separation in effective refractive index. At a wavelength of 1550 nm, the splitting in effective index is $\Delta n_{\mathrm{eff}} \sim 5 \times 10^{-3}$, while the aligned and anti-aligned pairs have $\Delta n_{\mathrm{eff}} \sim 6 \times 10^{-5}$, $\Delta n_{\mathrm{eff}} \sim 1 \times 10^{-4}$, and $\Delta n_{\mathrm{eff}} \sim 1.5 \times 10^{-4}$ for $|L| = 5$, $|L| = 6$, and $|L| = 7$, respectively. The distance in n_{eff} to the nearest neighboring mode influences the propagation stability of the mode, since it dictates the magnitude of a fiber perturbation that can couple light between modes. Thus, the $|L| = 7$ modes are expected to be more stable than the $|L| = 5$ modes. It is also seen that the $|L| = 6$ modes have other modes (dashed black lines) close by. This may affect the propagation stability of this set of modes, especially at shorter wavelengths, where it is seen that the distance is shorter. Allowing for manufacturing tolerances, and other small perturbations, the lines could shift slightly.

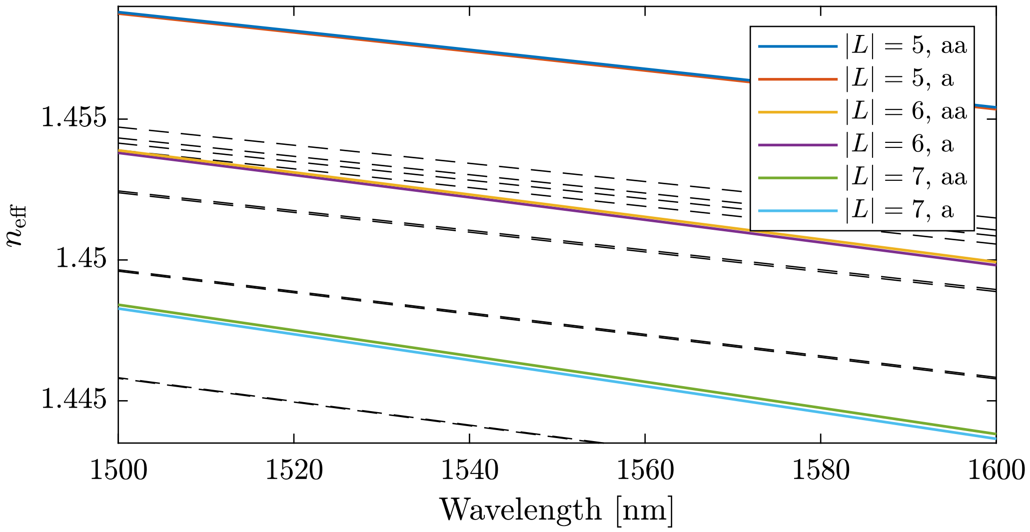

Figure 3.2: Calculated effective refractive indices of guided modes in the air-core fiber. The colored lines denote the desired OAM modes, while the dashed black lines denote other guided modes in the fiber.

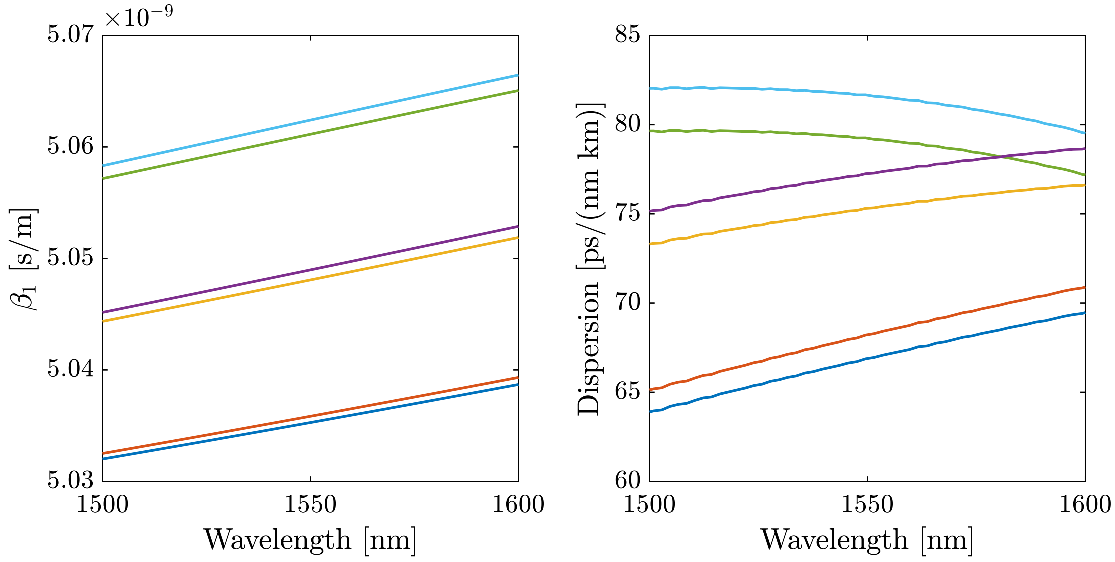

(a) Inverse group speed.

(b) Dispersion.

Figure 3.3: Derived properties for the air-core fiber.

Table 3.1: Relative arrival times for 1550 nm pulses launched into different fiber modes in the 1.2 km air-core fiber.

Mode	**Time [ns]**
$\lvert L\rvert = 5$, aa	0
$\lvert L\rvert = 5$, a	0.7
$\lvert L\rvert = 6$, aa	15.4
$\lvert L\rvert = 6$, a	16.5
$\lvert L\rvert = 7$, aa	31.1
$\lvert L\rvert = 7$, a	32.6

By differentiating the data in Fig. 3.2, the inverse group speed and the dispersion of the fiber are found. These are plotted in Fig. 3.3. The inverse group speed can be used to calculate the time it takes for a pulse of light to propagate through the fiber. It is seen that like the n_{eff}, the modes all have unique values of inverse group speed. This can be used for so-called time of flight measurements, where the mode content is characterized by launching a short pulse, and detecting the output time with a fast detector and a fast oscilloscope. The calculated relative arrival times are shown in Tab. 3.1.

The dispersion in the fiber is large, compared to standard optical fibers, with values ranging from $67\,\text{ps}\,\text{nm}^{-1}\,\text{km}^{-1}$ to $82\,\text{ps}\,\text{nm}^{-1}\,\text{km}^{-1}$ at 1550 nm. However, due to the short fiber length of 1.2 km, the accumulated dispersion is low, and thus, it does not result in any problems when using the fiber for optical communications.

3.3 Excitation of OAM modes in fiber

In order to utilize OAM modes in the air-core fiber, it is important to be able to excite the modes effectively, with minimal loss and crosstalk.

Here, a system where a fiber coupled laser source is coupled to the air-core fiber using an spatial light modulator (SLM), or a q-plate [40], as shown in Fig. 3.4, is analyzed. The setup consists of a fiber coupled external cavity laser (ECL), followed by a fiber polarization controller and a reflective silver collimator with a focal length of 15 mm. This creates a collimated beam in free-space, with a $1/\exp(2)$ intensity diameter of 3.5 mm.

In the case where an SLM is used (Fig. 3.4(a)), a computer generated hologram, consisting of a superposition of an azimuthal phase dependence, matching the desired OAM mode, and a spherical lensing phase is displayed on the SLM. This is given by

$$\theta_{\text{SLM}}(r, \phi) = L\phi - \frac{\pi}{\lambda f} r^2, \tag{3.1}$$

where (r, ϕ) are the spatial coordinates, λ is the wavelength, and f is the desired focal length. The beam is steered, and aligned to the fiber, using two silver mirrors, before passing through a quarter wavelength plate, creating the desired circular polarization. This is done because the SLM can only phase modulate horizontal linear polarization. Finally, the light is focused into the fiber using an aspheric lens.

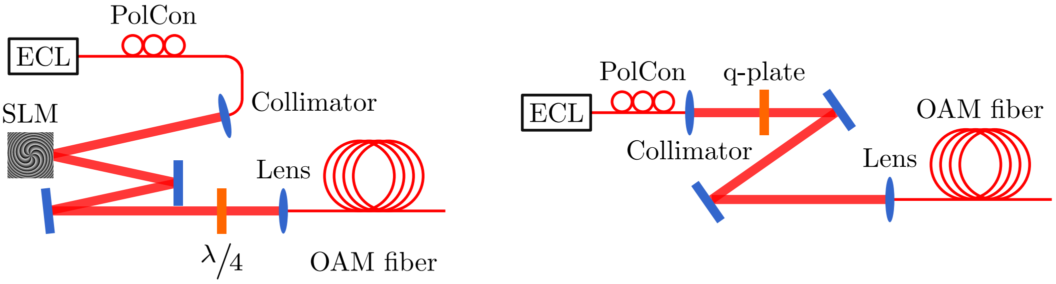

(a) Using SLM.

(b) Using q-plate.

Figure 3.4: Experimental setups for excitation of OAM modes in fiber. ECL: external cavity laser, PolCon: polarization controller, SLM: spatial light modulator, $\lambda/4$: quarter-wave plate.

In the case where a q-plate is used, the setup is simpler, since it replaces both the SLM and quarter-wave plate. Additionally, a single q-plate can generate a set of two degenerate OAM modes, depending on the input polarization state. A q-plate is a liquid crystal based half-wave plate with a fast axis rotating as a function of the azimuthal angle, described by

$$\alpha(\phi) = q\phi + \alpha_0, \tag{3.2}$$

where $\alpha(\phi)$ is the fast axis angle, q is a half-integer, and α_0 is an offset. The q-plate generates a polarization dependent set of free-space OAM modes, by transforming the light such that an input of σ^- is converted to $L = -2q, \sigma^+$ and σ^+ is converted to $L = +2q, \sigma^-$. Thus, the sign of the q-value dictates if the q-plate generates spin-orbit aligned, or spin-orbit anti-aligned modes. In both cases, a superposition of circular polarizations at the input is converted to a superposition of two degenerate OAM modes at the output. As with the SLM based setup, the beam is aligned using two mirrors, and focused into the fiber.

3.4 OAM fiber coupling using Fourier optics

Free-space propagation of OAM beams is not trivial, and the ideal choice of lenses can not be estimated in the same way as for Gaussian beams. Typically, free-space OAM beams are described as Laguerre–Gaussian modes [30], which, to some degree, can be treated analytically. However, using a setup as described in Fig. 3.4 does not result in a pure Laguerre–Gaussian mode, but rather a so-called circular beam [41], which is a superposition of several Laguerre–Gaussian modes [42].

Thus, in order to estimate the ideal parameters for excitation of OAM modes, the setup can be analyzed using Fourier Optics [43]. As source, a collimated Gaussian beam, is used

$$U(x, y) = \exp\left[-\frac{x^2 + y^2}{\omega_0^2}\right], \tag{3.3}$$

where U is the electric field, (x, y) are the transverse Cartesian coordinates, and ω_0 is the beam waist. As described in Sec. 2.1.2, the fundamental mode in a step-index fiber is a

Bessel function, and the collimator is not ideal. Despite this, a collimated Gaussian beam is used as an approximation.

This is multiplied with the phase mask on the SLM, as given in Eq. (3.1), and then propagates in free-space. The free-space propagation is modeled using Rayleigh-Sommerfeld diffraction

$$U(x, y, z + \Delta z) = \mathcal{F}^{-1}\left\{\mathcal{F}\left\{U(x, y, z)\right\} H(f_x, f_y, \Delta z)\right\}, \tag{3.4}$$

where $\mathcal{F}$ denotes the Fourier transform, and $\mathcal{F}^{-1}$ denotes the inverse Fourier transform. Δz is the propagation distance, and (f_x, f_y) are the frequency domain coordinates. The transfer function H is given by

$$H(f_x, f_y, \Delta z) = \exp\left[i2\pi\frac{\Delta z}{\lambda}\sqrt{1-(\lambda f_x)^2-(\lambda f_y)^2}\right]. \tag{3.5}$$

The focusing lens is modeled as a spherical lens, of focal length f

$$\theta_{\mathrm{lens}}(x, y) = \frac{k}{2f}\left(x^2 + y^2\right), \tag{3.6}$$

where $k = 2\pi/\lambda$ is the wavenumber. Intensity outside the clear aperture of the lens is set to zero, and the field is free-space propagated to the fiber end facet using Eq. (3.4). The quarter-wave plate is handled using Jones calculus [44]. The SLM can only modulate x polarized light, and thus the polarization of U before the quarter-wave plate is

$$\boldsymbol{U} = U\begin{pmatrix}1\\0\end{pmatrix}. \tag{3.7}$$

The Jones matrix for a quarter-wave plate rotated at an angle ϕ is

$$\boldsymbol{M}(\phi) = \exp\left(\frac{-i\pi}{4}\right)\begin{pmatrix}\cos(\phi)^2 + i\sin(\phi)^2 & (1-i)\sin(\phi)\cos(\phi)\\(1-i)\sin(\phi)\cos(\phi) & \sin(\phi)^2 + i\cos(\phi)^2\end{pmatrix}, \tag{3.8}$$

and setting $\phi = \pm\pi/4$ results in circularly polarized light. The matrix-vector product $\boldsymbol{M}(\pm\pi/4)\boldsymbol{U}$ then transforms U to σ^+ or σ^- polarization. It is noted that the position of the quarter-wave plate in the model is changed compared to the real setup, in order to simplify computations. Finally, the overlap integral of the free-space field, and the transverse part of the fiber mode is calculated as

$$\eta = \frac{|\int \boldsymbol{E}_{1,\perp}\cdot\boldsymbol{E}_{2,\perp}\,\mathrm{d}A|^2}{\int|\boldsymbol{E}_{1,\perp}|^2\,\mathrm{d}A\int|\boldsymbol{E}_{2,\perp}|^2\,\mathrm{d}A}. \tag{3.9}$$

Here $\boldsymbol{E}_1$ and $\boldsymbol{E}_2$ are the two electric fields, in this case the free-space field, and the fiber mode, respectively, and $\perp$ signifies that only the transverse part of the fields is used in the calculation. The fiber mode is calculated as described in Sec. 2.1.3.

3.4.1 Implementation

In practice, this method is implemented numerically in Matlab, with the main goal to estimate which focal length should be chosen for the focusing lens right before the air-core fiber.

The size of the beam from the collimator was analyzed using an InGaAs camera, and based on this, $\omega_0 = 3.5\,\mathrm{mm}$ was chosen. The propagation from the collimator to the SLM was ignored, since the beam was assumed to be perfectly collimated. The distance from the SLM to the fiber end facet was set to 0.8 m, which corresponds to the typical distance used in the experiments included in this thesis. Varying this distance affects the coupling efficiency slightly, but in an effort to reduce the number of variables that need optimization, it is kept constant. Four different lenses with focal lengths of 4.6 mm, 6.24 mm, 8.15 mm, and 11.0 mm are modeled, corresponding to the focal lengths of molded aspheric lenses available from Thorlabs. The clear apertures of the lenses are 5.07 mm, 5.0 mm, 8.0 mm, and 6.59 mm, respectively. The free-space propagation distance between the lens and the fiber is varied for each simulation, in order to find the distance resulting in the strongest possible coupling.

A numerical grid with a side length of $2^{10} = 1024$ points is chosen, and the pixel pitch is set to 12.5 µm, corresponding to the pixel size of the SLM. The numerical domain is zero padded such that the total side length is $2^{11} = 2048$ points, in order to avoid aliasing. The large difference in physical size between the SLM and the fiber end facet was handled by using a two step Fourier propagation algorithm [45], allowing a change in the spatial domain during propagation. At the fiber end facet, a pixel pitch of 39 nm was chosen, leading to a side length of 40 µm.

The modes of the air-core fiber are solved as described in Sec. 2.1.3, and interpolated onto the same numerical grid, and the overlap integrals between the generated free-space mode and each of the 12 guided OAM modes are calculated. The simulation is repeated for each of the 4 lenses, and for $L = \pm 5$, $L = \pm 6$, and $L = \pm 7$ with the quarter-wave plate rotation fixed, leading to excitation of 6 modes with a single polarization.

3.4.2 Results

First, the case where no lensing is applied to the SLM is analyzed, which makes it equivalent to the case where a q-plate is used. The results are plotted in Fig. 3.5. It is seen that in this case, the 6.24 mm lens delivers the best results, focusing all the modes in the same place, resulting in overlaps from 0.53 to 0.56, equivalent to a coupling loss in the range $-2.7\,\mathrm{dB}$ to $-2.5\,\mathrm{dB}$. The 8.15 mm lens also delivers usable results, however, a splitting into two peaks is observed. The right peak results in coupling losses in the range $-4.4\,\mathrm{dB}$ to $-4.1\,\mathrm{dB}$ at the same propagation distance. It is seen that good coupling is not possible using the 4.6 mm and 11.0 mm lenses.

The simulations are repeated with lensing added to the SLM. This effectively creates a two-lens system, enabling adjustment of the ring diameter in the focal plane. SLM focal lengths of 500 mm, 600 mm, 800 mm, 1000 mm, 1500 mm, 2000 mm, 3000 mm, 5000 mm, 0 mm, −5000 mm, −3000 mm, −2000 mm, −1500 mm, −1000 mm, −800 mm, −600 mm

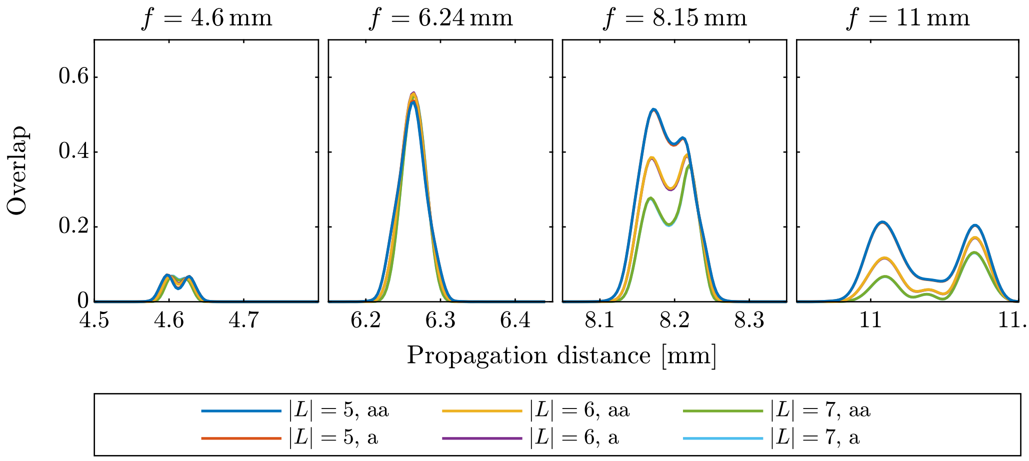

Figure 3.5: Overlap integrals between the generated free-space field, and the desired fiber mode, in the case where a q-plate, or an SLM with no lensing is used.

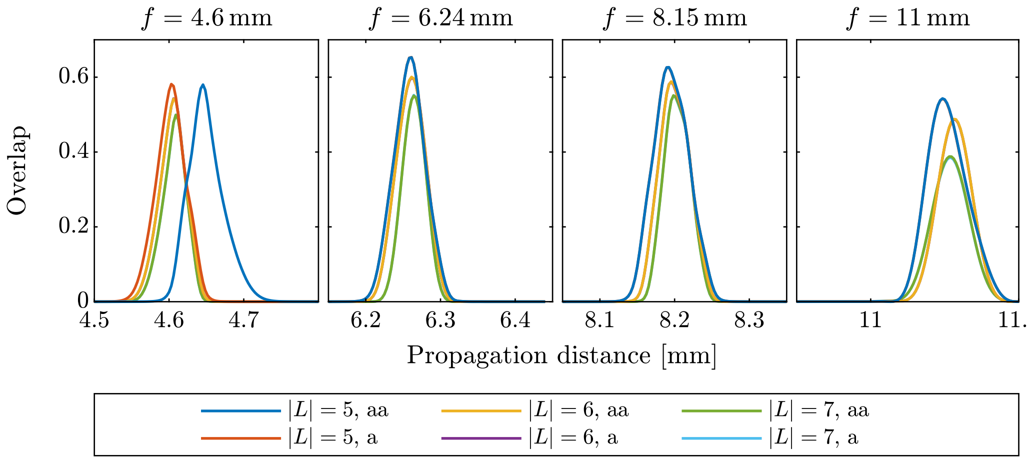

Figure 3.6: Overlap integrals between the generated free-space field, and the desired fiber mode, in the case where the optimal SLM lens is used.

and −500 mm are simulated, and the best results for all of the physical lenses are shown in Fig. 3.6. It is seen that performance across all of the lenses is significantly improved, but that the 6.24 mm lens and the 8.15 mm lens still deliver the best results. The 6.24 mm lens results in coupling losses of −2.0 dB, −2.2 dB and −2.6 dB for the $|L| = 5$, $|L| = 6$, and $|L| = 7$ modes, respectively. This is achieved using a focal length of 5000 mm for the $|L| = 5$ and $|L| = 6$ modes, while no lensing is needed for the $|L| = 7$ modes. The 8.15 mm lens results in losses of −2.2 dB, −2.4 dB and −2.6 dB using focal lengths of −3000 mm, −2000 mm and −1500 mm for the $|L| = 5$, $|L| = 6$, and $|L| = 7$ modes, respectively.

In practice it was found that both the 6.24 mm and the 8.15 mm lens deliver excellent results, with the 8.15 mm performing slightly better, presumably because of the larger clear aperture. In the laboratory, coupling losses of down to −2.5 dB for the $|L| = 5$ modes, and −3.0 dB for the $|L| = 7$ modes, were measured using an SLM with lensing and the 8.15 mm lens.

3.5 Characterization of air-core OAM fiber

For the experiments presented in this thesis, two different samples of the air-core OAM fiber were used. The two fibers both have a length of 1.2 km and are manufactured by OFS, from the same type of preform. However, due to variations in the drawing process, the properties of the fibers are slightly different.

The best sample supports 12 OAM modes, and was used for the communications experiment, described in Ch. 4. This sample was not available for the remaining experiments, and therefore a sample supporting 8 OAM modes was used. In the following, the two samples are experimentally characterized by performing loss measurements, and time of flight analysis. Additionally, mode images are presented for the 12-mode fiber.

3.5.1 Loss measurements

The loss measurements were performed by using a tunable ECL, scanning through the wavelength range from 1440 nm to 1600 nm. The 6 modes were excited cleanly using a SLM, as described in Sec. 3.3, the purity of the modes was confirmed using time of flight measurements, and the SLM settings for each of the modes were saved. The input power was recorded using a power meter connected to a 10 dB tap, and the wavelength was recorded using a wavelength meter. The output power was recorded using a 2nd power meter. This process was done for each mode, using the spool of fiber. Afterwards, the fiber was cut to ~ 1 m, without touching the input end, making sure that the mode excitation stays constant. The measurements were then repeated using the short fiber. Afterwards, the measurements for the long and the short fiber were corrected for fluctuations in the ECL using data from the wavelength meter and the reference power meter, before finally calculating the loss by simple subtraction.

The measured loss in the 12-mode fiber is plotted in Fig, 3.7. It is seen that the propagation loss in the C-band is ~ 0.8 dB/km, and is similar for all modes. At short wavelengths, the loss is significantly larger, and a clear separation between the modes is observed, with

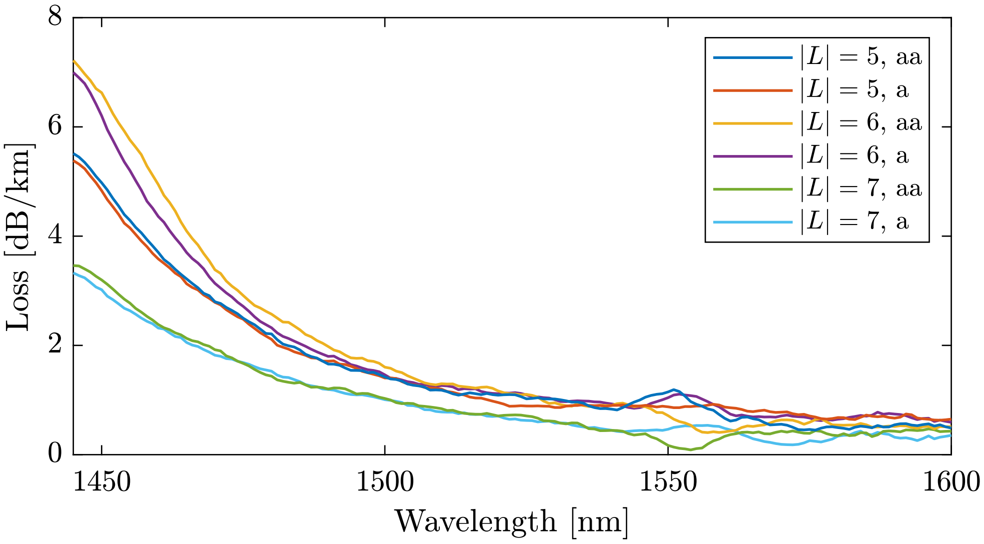

Figure 3.7: Measured loss in the 12-mode air-core fiber.

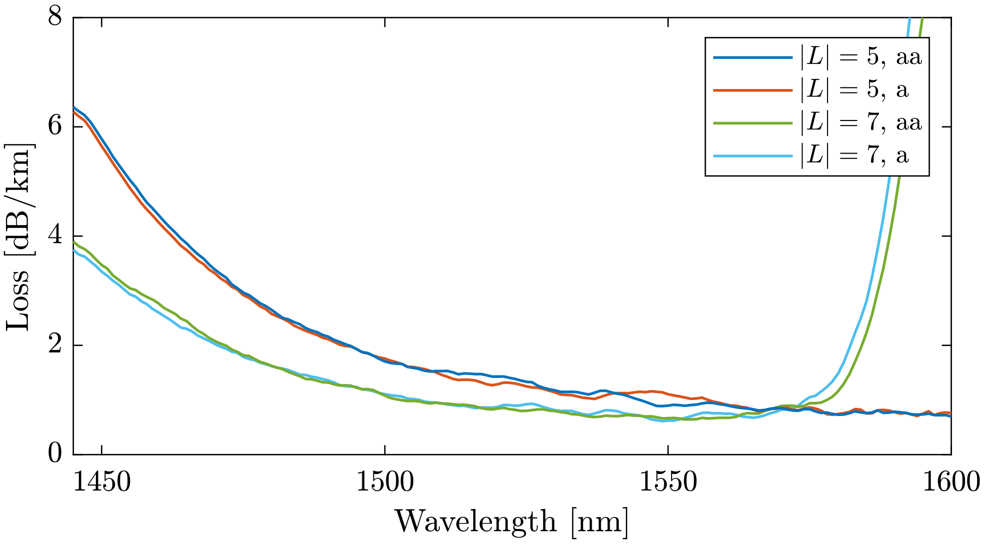

Figure 3.8: Measured loss in the 8-mode air-core fiber.

the $|L| = 6$ having the highest loss, the $|L| = 5$ modes in the middle, and the $|L| = 7$ modes showing the lowest loss. The high loss at short wavelengths is presumably caused by water absorption.

The loss measurements for the 8-mode fiber are plotted in Fig. 3.8. The loss is seen to be comparable to the 12-mode fiber, with a few key differences. It is seen that the $|L| = 7$ cuts off at $\sim 1580\,\mathrm{nm}$, meaning that fiber does not guide these modes at longer wavelengths. Additionally, the short wavelength loss is larger in the 8-mode fiber, while the loss in the C-band is comparable.

3.5.2 Time of flight measurements

Time of flight measurements are a useful way of characterizing the purity of mode excitation [46], provided that the fiber under test (FUT) is sufficiently long. As seen in Fig. 3.3, the different modes propagate with different group velocities (β_1), and this can be used to analyze which modes are excited at the fiber input. It can also, to some degree, be used to analyze distributed mode coupling in the fiber. The main advantage of time of flight measurements compared to interferometric methods such as S^2 imaging [47] or C^2 imaging [48], is that time of flight measurements are truly real time, which has not been achieved for the interferometric methods [49].

Time of flight measurements were performed by launching a mode locked laser with a wavelength of 1558 nm, and a full width at half maximum (FWHM) pulse with of 1.7 ps. The pulses are transform limited solitons, and thus assuming a sech^2 shape with a time bandwidth product of 0.315 yields a spectral FWHM of 1.5 nm. Using the calculated dispersion values from Fig. 3.3(b), the pulse with at the fiber end is estimated to $\sim 150\,\mathrm{ps}$. The repetition rate is 15 MHz, and the pulses are launched into the air-core fiber using an SLM, as shown in Fig. 3.4(a). At the fiber end, the output is focused onto a free-space InGaAs photodetector (PD), with a bandwidth of 5 GHz, connected to a fast digital sampling oscilloscope. In this setup, it is important that the wavelength of the pulsed laser is close to the wavelength at which the setup will be used after alignment, i.e. within the C- and L-bands for the purpose of this thesis. This ensures that the setup is aligned for the wavelength where it will be used.

The resolution in time is determined by the pulse width of the laser, and the bandwidth of the PD and the oscilloscope. In this case, the PD is the slowest part, and thus, the temporal resolution is expected to be $\sim$200 ps. As seen in Tab. 3.1, the minimum expected group delay difference in the air-core fiber is 0.7 ns, and thus, the resolution is sufficient to characterize mode excitation in this fiber. The resolution could be improved by up to an order of magnitude by using a faster PD, and using longer pulses to avoid dispersion. Even with an order of magnitude improvement in resolution, the time of flight method is not suitable for characterization of short ($\sim$1 m to 10 m) fibers, but is excellent for real time input alignment in the 1.2 km air-core fiber.

The time of flight measurements of the 12-mode fiber are shown in Fig. 3.9. The figure is split into two parts, where the top panel shows the 6 measured impulse responses, normalized and plotted on a linear scale, with an offset for clarity. The location of each of the peaks is marked with a vertical black line, and the values are tabulated in Tab.

Table 3.2: Relative mode delays for the 12-, and 8-mode air-core fibers, measured using time of flight.

Mode	**12-mode fiber time [ns]**	**8-mode fiber time [ns]**
$\lvert L\rvert = 5$, aa	0.0	0.0
$\lvert L\rvert = 5$, a	0.6	0.8
$\lvert L\rvert = 6$, aa	13.6	-
$\lvert L\rvert = 6$, a	14.6	-
$\lvert L\rvert = 7$, aa	27.3	30.5
$\lvert L\rvert = 7$, a	28.7	32.2

3.2. It is seen that the group velocity of the modes comes in 3 pairs of spin-orbit aligned, and spin-orbit anti-aligned modes, with a ~1 ns spacing, and ~15 ns spacing between the groups. These values are similar to the calculated values from Tab. 3.1. The bottom panel shows the impulse responses plotted individually on a logarithmic scale, making it easier to evaluate the purity of the modes. Here, a main peak, normalized to 0 dB is seen, followed by some ringing from the PD. Unfortunately this ringing obscures any anti-aligned to aligned coupling that may happen either during the mode excitation or distributed in the fiber. However, this can be estimated to be similar to the aligned to anti-aligned coupling, which can be identified as a shoulder to the left of the main peak of the aligned modes. This shoulder is largest for the $|L| = 5$ modes, as expected. Additionally, some coupling between the mode orders is observed. When exciting $|L| = 6$, aa, coupling of -19.3 dB to $|L| = 5$, aa is observed. In this case, no significant coupling to $|L| = 5$, a is seen. When exciting $|L| = 6$, a, the situation is reversed, and it is seen to couple to $|L| = 5$, a, but not $|L| = 5$, aa. In general, coupling to the nearest neighbor i.e. between the two modes with same $|L|$ and coupling between modes of different $|L|$ with same handedness is observed. In all cases, the modes have a purity of at least -17 dB, corresponding to 98 %, marked by the horizontal black line.

Time of flight measurements of the 8-mode fiber are seen in Fig. 3.10, and the relative mode delays are tabulated in Tab. 3.2. The general observations are similar to the case of the 12-mode fiber. Aligned to anti-aligned coupling, is seen to be slightly stronger, and thus it is assumed that anti-aligned to aligned coupling is also stronger. A mode purity of at least -17 dB, as measured in the 12-mode fiber, is also observed in the 8-mode fiber.

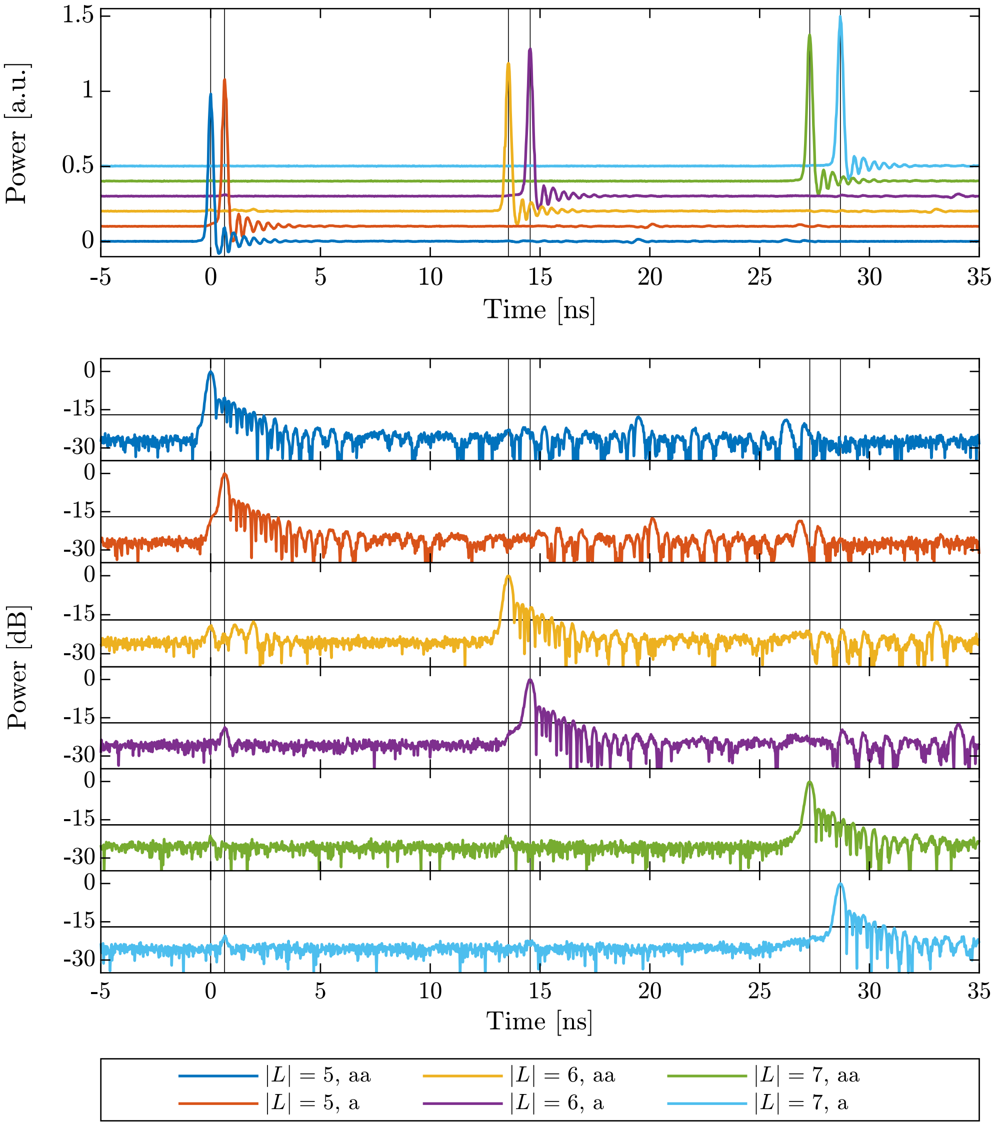

Figure 3.9: Time of flight measurements for the 12-mode fiber.

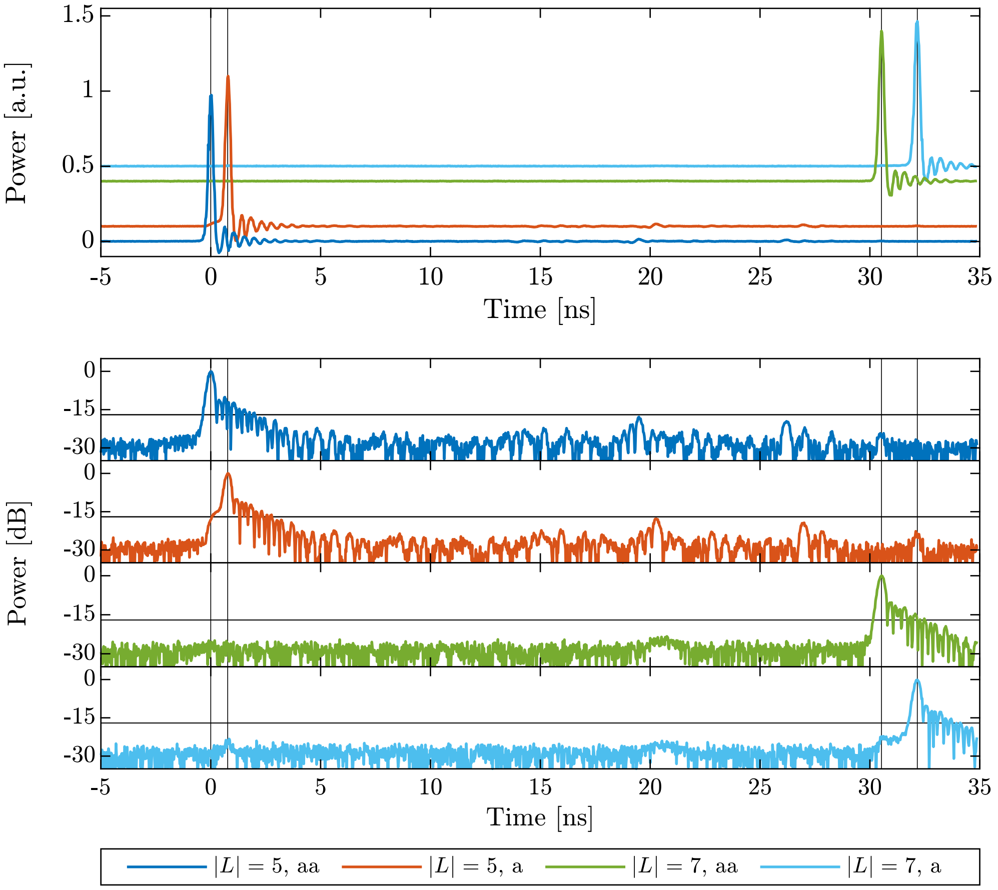

Figure 3.10: Time of flight measurements for the 8-mode fiber.

3.5.3 Mode images

The 12-mode fiber was also characterized visually, where the fiber end facet was imaged onto an InGaAs camera. In addition, the OAM modes were interfered with an expanded Gaussian beam, providing a phase reference. The sets of mode images (left), and the images with interference patterns (right) are shown in Fig. 3.11. It is seen that the intensity profiles of the modes are ring-shaped, and that the diameter of the ring increase with $|L|$. The smoothness of the rings is related to the purity of the mode, where a perfectly smooth ring would indicate a pure mode. The interference patterns reveal the phase of the rings, such that the number of "arms" of the spirals correspond to $|L|$, while the direction of the spirals correspond to the sign of L. Additionally, the spirals document that the light exiting the fiber does indeed carry OAM.

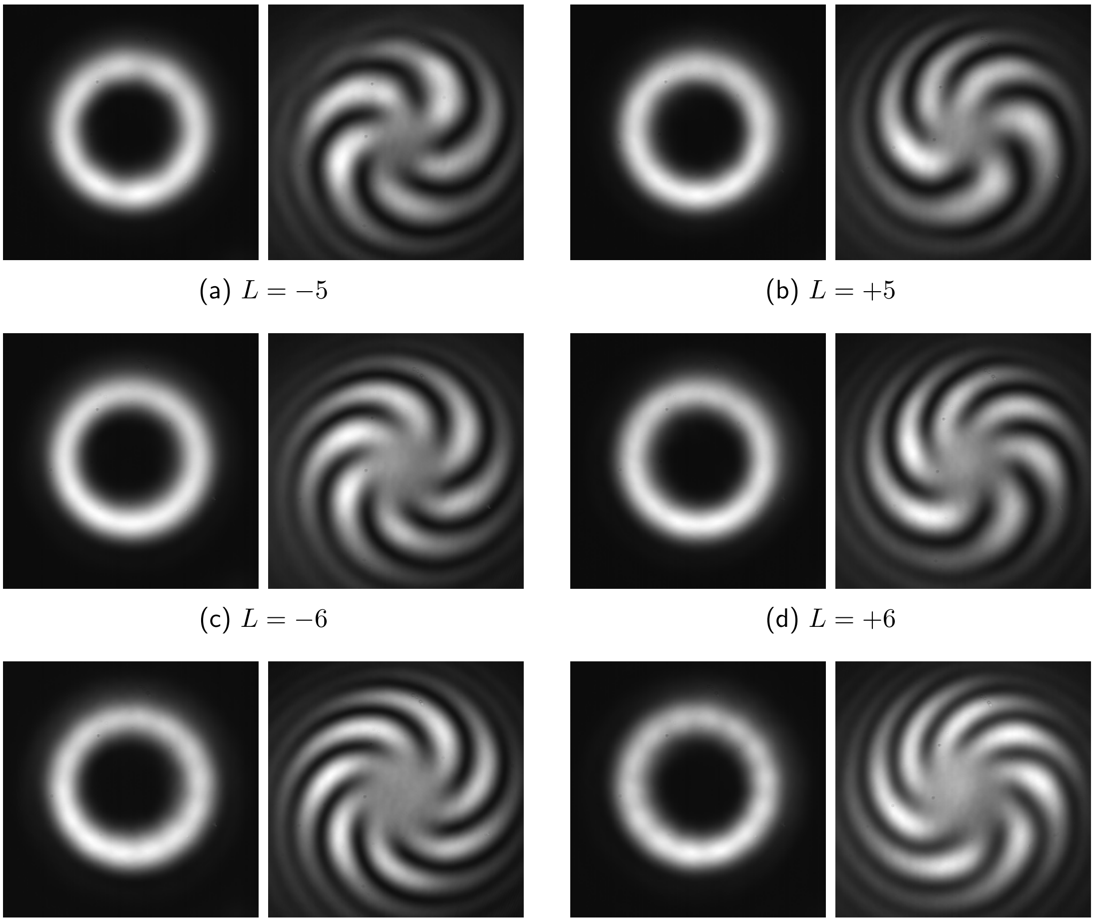

(a) $L = -5$

(b) $L = +5$

(c) $L = -6$

(d) $L = +6$

(e) $L = -7$

(f) $L = +7$

Figure 3.11: Camera images of OAM modes in the air-core fiber. The left image for each mode shows the intensity distribution, and the right image shows the phase, by interfering with an expanded Gaussian beam.

3.6 Conclusion

This chapter has introduced the air-core OAM fiber, and the modes of this fiber were solved using the theory described in Ch. 2.

Experimental setups for excitation of modes in the air-core fiber were presented, based on either SLMs or q-plates. These setups were analyzed using Fourier optics, and a theoretical coupling loss down to 2.0 dB was calculated. In practice this loss was 2.5 dB.

Two fiber samples were characterized experimentally, the 8-mode air-core fiber, and the 12-mode air-core fiber, both with a length of 1.2 km. The loss in the fibers was measured to ~0.8 dB/km in the C-band, and it was found to increase for shorter wavelengths. The mode purity was measured to be at least −17 dB, corresponding to 98 %, using the time of flight method. Finally, mode images showing the intensity distribution, and interference patterns showing the phase fronts of the OAM modes were presented.

Chapter 4

Optical communications using OAM modes

This chapter is based on results originally published in [50] and [51].

4.1 Introduction

In recent years, MDM has been explored extensively in order to increase the capacity of optical fiber links [13]. In MDM, several spatial modes propagate simultaneously in the same fiber core. During propagation, these fiber modes can mix in the presence of perturbations such as fabrication imperfections or bending. This mixing can be fully compensated using multiple-input multiple-output (MIMO) digital signal processing (DSP), in the absence of mode dependent loss. However, MIMO processing scales in complexity with N^2, where N is the number of modes, including polarization modes, such that e.g. 30 modes require 30×30 MIMO equalization [52].

Alternative schemes have been developed to reduce inter-modal mixing, and thus avoid or reduce the use of cost and power intensive MIMO processing. One proposal is mode-group multiplexing, where several groups of near-degenerate modes are used as data channels. This is achieved either by optically pre-compensating to launch a specific superposition of modes for a given fiber [53], or by reduced-complexity MIMO applied to the groups independently [54]. A second proposal is mode multiplexing, where every individual mode is used as a data channel in a fiber in which all degeneracies are broken, e.g. elliptical-core fibers [19]. In these cases, scalability in the number of modes have yet to be demonstrated.

Another option for MIMO free MDM is OAM modes. With appropriate fiber design, as described in Ch. 2 and Ch. 3, these modes are separated from their nearest neighbors in effective refractive index (n_{eff}), and have been shown to be propagation-stable on the order of kilometers [21].

Previously, MIMO-free data transmission has been demonstrated with four OAM modes over km-lengths of suitably designed optical fibers [35, 36]. Fiber transmission of eight OAM modes has also been demonstrated over longer lengths, though this required the use of MIMO [55]. However, considering that fibers supporting a larger number of OAM states have been designed and tested [37,38], the number of modes used for OAM MDM can be increased.

This chapter investigates MIMO-free MDM transmission of 12 OAM modes, which is the highest number of modes transmitted MIMO-free over an optical fiber longer than 1 km. wavelength-division multiplexing (WDM) compatibility is demonstrated, by using a 25 GHz spaced frequency comb with 60 channels modulated with 10 GBaud QPSK. All measured data channels achieve bit error rates (BERs) below the soft-decision forward error correction (SD-FEC) limit, and it is found that the system performance is limited by intermodal crosstalk. This crosstalk is analyzed, in terms of in-fiber crosstalk contributions, and mux/demux contributions, in order to identify which parts of the system is limiting the performance.

4.2 Experimental setup

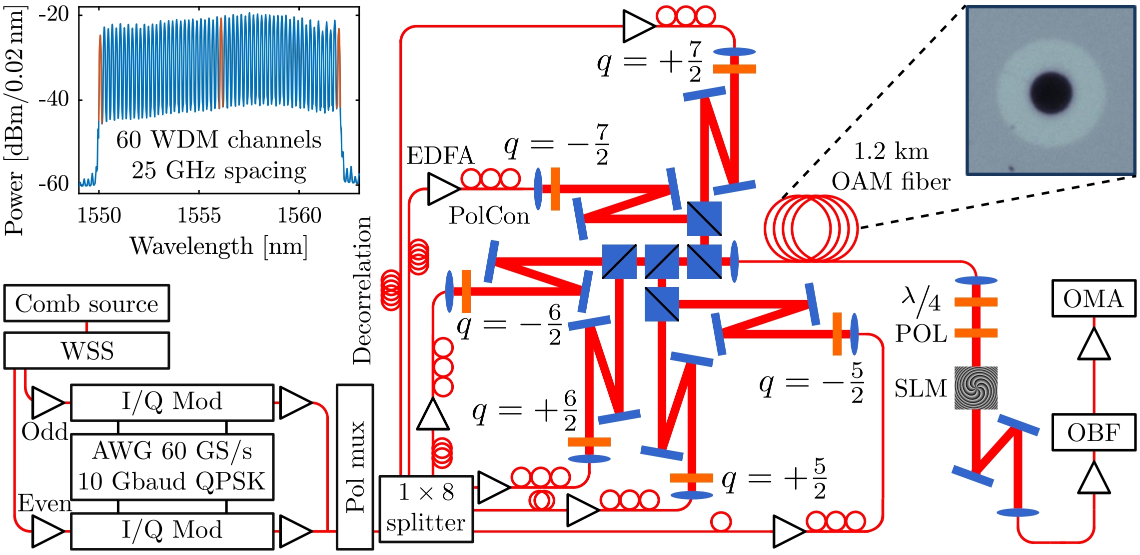

Figure 4.1: Schematic of the experimental setup, including the modulated spectrum (top left inset), and a microscope image of the OAM fiber (top right inset). WSS: wavelength selective switch, AWG: arbitrary waveform generator, I/Q Mod: I/Q modulator, SLM: spatial light modulator, OBF: optical band-pass filter, OMA: optical modulation analyzer, q: q-plate, PolCon: polarization controller, POL: linear polarizer, $\lambda/4$: quarter-wave plate.

The experimental setup is shown in Fig. 4.1. A frequency comb of 60 WDM channels with a 25 GHz spacing, spanning from 1550 nm to 1562 nm is generated, by using a 1544 nm continuous wave (CW) laser, which is phase- and then intensity modulated at 25 GHz. This creates initial sidebands, which are amplified and broadened in two stages of highly nonlinear fiber, resulting in a broad comb. The comb is long pass filtered at 1550 nm, since the part of the spectrum near the seed wavelength has low optical signal to noise ratio

(OSNR). The amplitude of the 60 WDM channels are equalized, and odd and even channels are split using a wavelength selective switch (WSS). The upper limit of 1562 nm was chosen since it is the maximum wavelength allowed by our erbium doped fiber amplifiers (EDFAs), while the lower limit of 1550 nm is chosen since the fiber does not support all 12 OAM modes at shorter wavelengths. The fiber was designed for enhanced intermodal splitting for OAM modes of $|L| = 5, 6$, and 7, which also determines the launched mode orders in the experimental system. This splitting is enabled via a ring fiber design with large refractive index steps [38].

Odd and even channels are separately amplified and modulated with 10 GBaud QPSK signals, before being amplified again, and recombined in a 3 dB polarization maintaining coupler. This results in 60 single-polarization WDM channels with odd and even decorrelation. Polarization multiplexing is emulated by splitting the signal in two, rotating and delaying one part by ~ 1.5 ns, and then recombining in a polarizing beam splitter (PBS). Finally, the signal is split in a 1x8 coupler, 2 outputs are discarded while the remaining 6 polarization multiplexed outputs are amplified separately and temporally decorrelated.

The 12 OAM modes are generated and multiplexed in free-space. Each of the 6 amplified outputs is passed through a polarization controller, collimated into free-space, and passed through a q-plate [40], which is a liquid crystal based half-wave plate with a fast axis rotating as a function of the azimuthal angle. The q-plate generates a polarization dependent set of free-space OAM modes, by transforming the light such that an input of σ^- is converted to $L = -2q, \sigma^+$ and σ^+ is converted to $L = +2q, \sigma^-$. Thus, the sign of the q-value dictates if the q-plate generates spin-orbit aligned, or spin-orbit anti-aligned modes. In both cases, a superposition of circular polarizations at the input is converted to a superposition of two degenerate OAM modes at the output.

The polarization of the light in each of the six outputs into free-space is adjusted, using the polarization controllers, in order to generate a linear combination of the degenerate states, such that the desired OAM modes are detected at the fiber output. This is needed such that the modes can be separated by the mode filter, which is described later. This means that each signal is not mapped onto a pure circular polarization state at the input of the fiber, but rather to a linear combination of the two degenerate modes. During transmission in the fiber, perturbations lead to a unitary transformation, rotating these polarizations, such that pure circular polarization states are detected at the output. This polarization rotation is similar to what happens in a single-mode fiber (SMF), although the perturbation required to achieve a polarization rotation is significantly larger in OAM modes [38]. This means that unlike in SMFs, the polarization does not have to be realigned even if the fiber is exposed to small movements.

All of the six beams are individually aligned using silver mirrors, and combined using five 3 dB plate beam-combiners, before being coupled into the OAM fiber using a lens ($f = 8$ mm), with a coupling loss of ~ 2.5 dB. Since the beams pass through a different number of beam combiners, the loss is different for each free-space path, therefore the signal powers are equalized using the six EDFAs. Ultimately this results in a total of 12 multiplexed modes; $L = \pm 5, \sigma^{\pm}$, $L = \pm 5, \sigma^{\mp}$, $L = \pm 6, \sigma^{\pm}$, $L = \pm 6, \sigma^{\mp}$, $L = \pm 7, \sigma^{\pm}$, and $L = \pm 7, \sigma^{\mp}$.

The 12-mode signal is transmitted over a 1.2 km OAM fiber [38] and at the output, the 12

OAM modes are measured one at a time, using a mode filter. This is achieved by passing the light through a circular polarizer comprising a quarter-wave plate with the fast axis oriented at 45° relative to the transmission axis of a linear polarizer. After this step, 6 of the 12 modes remain, each with unique L values. The desired mode is projected onto a mode with $L = 0$ using a SLM with a spiral phase pattern, generated from an azimuthal phase, matching the desired mode, and a parabolic phase, giving a lensing effect. This mode is coupled into a SMF, which acts as a pinhole, filtering the remaining five undesired modes [20].

Finally, the signal is amplified, and a single WDM channel is filtered out with a tunable band-pass filter. The signal, now containing only a single data channel, is amplified again, and sent to an optical modulation analyzer (OMA) that handles demodulation, digital signal processing, and error counting.

The system is aligned using a picosecond pulsed laser source and a 5 GHz free-space PD, to measure the temporal impulse response of each of the six paths independently [46]. Since the fiber modes have different β_1 values (inverse group speed), this reveals how much power is coupled into each of the 6 non-degenerate modes, with a dynamic range of $\sim 20\,\mathrm{dB}$. This process is described in Sec. 3.5.2. Afterwards, the polarization of each path is aligned by temporarily removing one output polarization from the polarization multiplexer, and adjusting the polarization controller such that projection into one degenerate state is minimized across the frequency comb, by using a circular polarizer and an optical spectrum analyzer. The polarization is stable, and thus does not need further adjustments during the process of alignment and data transmission. It is observed that while it is easy to get a strong suppression at a single wavelength, it is not always possible to achieve strong suppression of degenerate states across the entire comb. This may be due to either imperfect input coupling, or in-fiber mode coupling [56].

4.3 Results and discussion

The system performance was evaluated by measuring BERs at 3 different wavelengths, 1550 nm, 1556 nm, and 1562 nm, corresponding to the comb's shortest, center, and longest wavelength, respectively. All measurements were performed with all 60 wavelengths and 12 modes present in the fiber. The results are shown in Fig. 4.2, with example constellation diagrams, from the 3 different wavelengths, 3 different mode groups, and corresponding to low, middle, and high BERs. All 34 measured channels are below the SD-FEC of 2×10^{-2}, while 24 are below the hard-decision forward error correction (HD-FEC) threshold of 3.8×10^{-3}.

It is noted that data from the $L = \pm 6, \sigma^{\mp}$ (anti-aligned) modes is missing at 1550 nm. As seen in Fig. 4.3(a) this mode (top red line) experiences accidental degeneracies with double ringed, $m = 2$ modes (dashed black lines). This leads to significant multipath interference (MPI), and thus these two modes could not be detected at this wavelength. At the other two measured wavelengths, all 12 modes were detected. By design, this fiber should have experienced no mode crossing for any of the 12 modes. Thus, it is possible that future fabrications of this fiber would yield transmission in all 12 modes across the

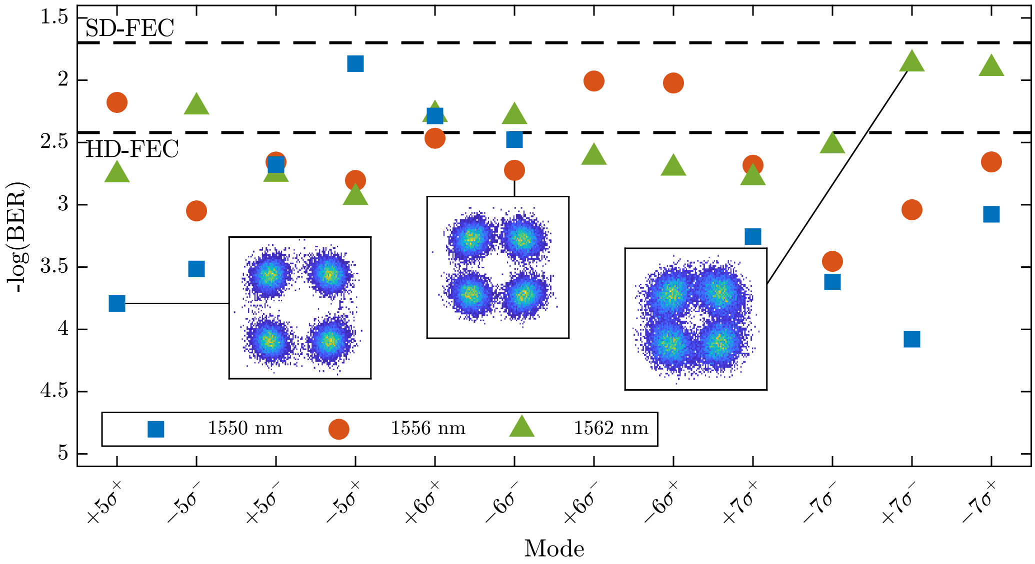

Figure 4.2: Measured BERs with example constellation diagrams, from the 3 different wavelengths, 3 different mode groups, and corresponding to low, middle, and high BERs (inset). All 34 measured modes are below the SD-FEC limit, and it is noted that data from the $L = \pm 6, \sigma^{\mp}$ (anti-aligned) modes is missing at 1550 nm, due to accidental degeneracies in the fiber.

C-band.

The main limitation to the system performance was intermodal crosstalk. In order to analyze this, the system transmission matrix was measured, and results are shown in Fig. 4.3(b). Each column corresponds to an output projection setting, while each row indicates which modes are launched and thus contribute to crosstalk at the receiver. It is seen that total crosstalk (top row in Fig. 4.3(b)) into each of the modes was measured to be between -10.3 dB and -11.8 dB. This crosstalk has two main contributions, namely fiber mode coupling, and crosstalk at the mux/demux. By comparing the middle and bottom rows in 4.3(b), it was found that the strongest parasitic contribution for the $|L| = 5$ modes is in-fiber crosstalk between the $|L| = 5$ spin-orbit aligned and anti-aligned modes (-12.8 dB), because this mode group has the smallest n_{eff} splitting of 6×10^{-5}. This analysis also reveals that the $|L| = 6$ and $|L| = 7$ modes are mainly limited by crosstalk from modes of different $|L|$. As seen in Fig. 4.3(a), the n_{eff} splitting between L and $L \pm 1$ is an order of magnitude larger than between modes with the same $|L|$. Therefore in-fiber mode coupling between adjacent OAM mode orders is unlikely to be significant at ~ 1 km [57], and thus it is concluded that this MPI is primarily due to imperfections in the free-space mux/demux. Furthermore, significant temporal drifting of the mux/demux was observed, leading to crosstalk increasing with time, thus limiting the number of measurements that could be performed before re-alignment was needed.

Assuming that all 30 WDM channels between 1550 nm and 1556 nm fail to carry the $|L| = 6$ spin-orbit anti-aligned modes, and thus only support 10 modes, while the 30 longer wavelength channels support 12 modes, the demonstrated system may potentially have a

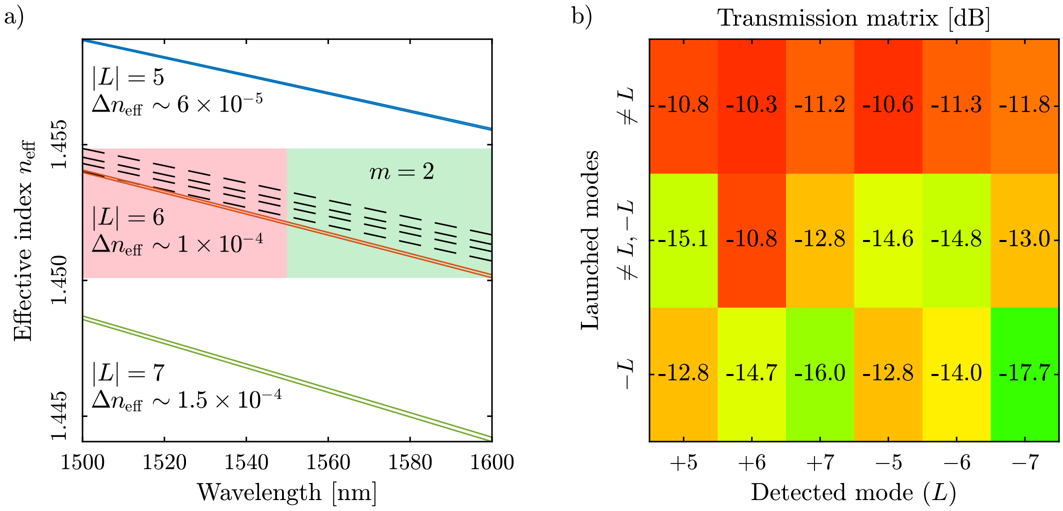

Transmission matrix [dB]

	$+5$	$+6$	$+7$	-5	-6	-7
$\neq L$	-10.8	-10.3	-11.2	-10.6	-11.3	-11.8
$\neq L, -L$	-15.1	-10.8	-12.8	-14.6	-14.8	-13.0
$-L$	-12.8	-14.7	-16.0	-12.8	-14.0	-17.7

Figure 4.3: a) Simulated n_{eff} as a function of wavelength, the red shaded area denotes the bandwidth where the $|L| = 6$ anti-aligned modes have strong MPI. b) System transmission matrix where each column corresponds to an output projection setting, while the rows correspond to modes launched. Each column is normalized to 0 dB in the desired mode with entries denoting crosstalk in dB. $-L$ indicates crosstalk from in-fiber nearest neighbors, $\neq L, -L$ indicates contributions from other mode orders, and $\neq L$ indicates total crosstalk. Crosstalk is measured using the frequency comb, yielding an average for the used optical spectrum.

total aggregate capacity of 10.56 Tbit/s after 20% forward error correction (FEC) overhead has been deducted for all channels. Compared to previous fiber-based OAM transmission systems, this corresponds to a 6-fold improvement in capacity compared to [35], or a 3-fold improvement in capacity, and a 12-fold improvement in distance compared to [58].

4.4 Crosstalk analysis

To improve the understanding of the crosstalk contributions, namely in-fiber crosstalk, and mux/demux crosstalk, they are further analyzed. In the mux, crosstalk comes mainly from misalignments, where the input beam is shifted compared to the fiber end facet. In order to compute how much power is coupled into each fiber mode, the normalized overlap integral between the free-space field and each fiber mode is computed for different spatial offsets. At perfect alignment, the input field is matched with a single fiber mode, and is orthogonal to the remaining modes. However, a misalignment (shift in spatial position) results in parasitic mode excitation.

To do this, the fiber modes were solved using a finite difference frequency domain mode solver. A total of 52 guided modes were found at 1555 nm (26 in each polarization), where 12 are the desired OAM modes, and the remaining 40 are lower order modes that do not propagate stably in the fiber, but must be included in these calculations. The overlap of each desired mode (simulating the input beam) with all of the 52 modes (simulating the fiber mode) is computed, then the input field is shifted along the x-axis, and the computations are repeated. Because of circular symmetry, shifting the input along a single axis is sufficient.

The results are shown in Fig. 4.4, where the maximum crosstalk contributions for the 12 desired modes are plotted. The crosstalk is split into contributions to modes with other $|L|$, and the same $|L|$ i.e. inter-group crosstalk and intra-group crosstalk, respectively. The maximum crosstalk is chosen as a figure of merit since it ensures that all spatial channels perform within a given threshold. The individual modes behave similarly to the maximum, and are within 1 dB of the maximum for the case of other $|L|$, and within 4 dB in the case

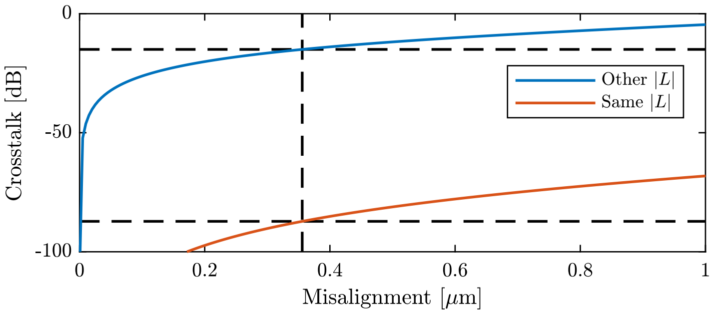

Figure 4.4: Simulated maximum crosstalk to modes with different $|L|$ and modes with the same $|L|$ as a function of input misalignment. Crosstalk is defined as the amount of power coupled to an undesired mode, divided by the power coupled to the desired mode.

of same $|L|$. It is seen that in order to have a maximum crosstalk of $-15\,\mathrm{dB}$ (corresponding to the measured values in Fig. 4.3(b)) the maximum allowed alignment error is $350\,\mathrm{nm}$. At this tolerance, the crosstalk contribution to modes with the same $|L|$ is $-87\,\mathrm{dB}$, thus concluding that misalignments in the mux/demux only affects crosstalk to modes with other $|L|$. This crosstalk mainly goes to neighboring modes with same polarization and same handedness, i.e. when trying to excite $L = +7\sigma^+$ the main undesired mode will be $L = +6\sigma^+$. This, along with the fact that the $|L| = 6$ modes have two neighbors, explains why they perform worse than the $|L| = 5$, modes, even though they have a larger n_{eff} splitting.

In addition to crosstalk from misalignments, crosstalk from polarization mixing in the free-space optics should also be considered. Since the fields are circularly polarized, it is impossible to align them to either the s- or p-axis of the optical components, as would be done with linear polarization. Therefore, any difference in the complex reflection (or transmission) coefficients of the mirrors and beam combiners transforms the polarization from circular to elliptical. This corresponds to a coupling between the two orthogonal polarization states σ^+ and σ^-, without affecting the OAM, thus resulting in crosstalk from spin-orbit aligned modes to spin-orbit anti-aligned modes. This crosstalk contribution is estimated to $\sim -25\,\mathrm{dB}$ based on time of flight measurements and specifications of the optical components. Compared to the measured spin-orbit aligned to spin-orbit anti-aligned crosstalk for the full system (shown in Fig. 4.3(b)), this is an order of magnitude lower. Thus, it is concluded that the majority of the crosstalk to modes with the same $|L|$ does not come from the mux/demux, and therefore must originate in the fiber.

To examine in-fiber crosstalk, further measurements were performed, by transmitting a set of four modes with the same $|L|$, and thereby only looking at crosstalk within this group. As concluded above, this should reduce the effects of mux/demux crosstalk by an order of magnitude. Since in-fiber crosstalk depends on the difference in effective refractive index, Δn_{eff}, the impact can be predicted by studying Fig. 4.3(a). It is seen that modes with different $|L|$ have $\Delta n_{\mathrm{eff}} \sim 5 \times 10^{-3}$, while the aligned and anti-aligned pairs have $\Delta n_{\mathrm{eff}} \sim 6 \times 10^{-5}$, $\Delta n_{\mathrm{eff}} \sim 1 \times 10^{-4}$, and $\Delta n_{\mathrm{eff}} \sim 1.5 \times 10^{-4}$ for $|L| = 5$, $|L| = 6$, and $|L| = 7$, respectively. Thus it is expected that in-fiber crosstalk should be most significant for the $|L| = 5$ modes, and least significant for the $|L| = 7$ modes, while in-fiber crosstalk to modes with different $|L|$ should be virtually nonexistent.

These results are shown in Fig. 4.5 using colored points, while the 12-mode results, from Fig. 4.2 are shown in black for comparison. It is seen that the BERs in the 4-mode case are better than in the 12-mode case. In the case of $|L| = 6$, and $|L| = 7$ all of measured 4-mode BERs are better than the corresponding 12-mode measurements, while in the case of the $|L| = 5$ modes, 8 of the 12 modes have lower BERs than the corresponding 12-mode measurements. Additionally, it is seen that the BERs match the predictions based on the simulated Δn_{eff}, thus confirming that in-fiber crosstalk is the limiting factor in the 4-mode measurements. This also means that mux/demux crosstalk was a main limiting factor in the 12-mode transmission, and thus if an ideal mux/demux was used, the 12-mode BERs could be expected to be as low as the 4-mode BERs. In the future, new multiplexers based on multi-plane light conversion [59], or photonic lanterns [60] could solve this problem.

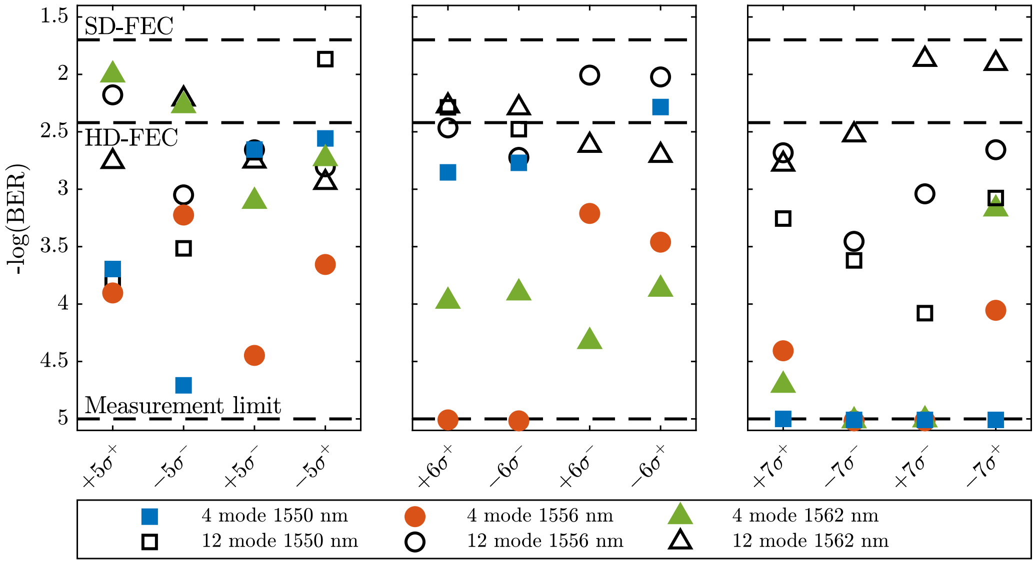

Figure 4.5: Measured BERs for sets of four modes with same $|L|$ (colored markers) and the 12-mode measurements from Fig. 4.2 for reference (black hollow markers).

4.5 Summary and Conclusion

12 OAM modes, each carrying a 10 GBaud QPSK signal have been transmitted over a 1.2 km air-core fiber. WDM compatibility was demonstrated by using a comb source with 60 WDM channels with 25 GHz spacing. This is the largest number of modes over which MIMO-free data has been transmitted over a fiber longer than 1 km. The most significant limitations encountered in this demonstration were the difficulties and drifts associated with aligning 6 free-space optical arms with high accuracy. Crosstalk was analyzed in terms of in-fiber contributions and contribution from the mux/demux, and it was concluded that the mux/demux was the main limiting factor. Thus it is expected that developments in mux/demux technologies would significantly enhance the system performances and capacity of MIMO-free data transmission using OAM fiber modes.

Chapter 5

Raman amplification of OAM modes

5.1 Introduction

Optical amplification is essential for many applications. In optical communications it is needed to transmit data over long distances, and in nonlinear optics it is needed to achieve high powers leading to large nonlinear phase-shifts. In many applications EDFAs are the preferred type of amplifiers, although, in order to fabricate an EDFA supporting a specific set of modes, an erbium doped fiber that can guide this set of modes must be fabricated. This is extremely difficult, but has been achieved for the first 6 LP modes [61]. It has also been shown in [62], that an EDFA for the 12-mode air-core OAM fiber is theoretically possible, although this has only been demonstrated in practice for modes with $|L| = 1$ [63].

Raman amplification is an alternative to the EDFA that offers several advantages. In the case of higher-order modes (HOMs), the possibility of amplification in the transmission fiber, means that no special doped fibers have to be fabricated. In the case of communications systems, Raman amplification can also offer a smoother power profile, i.e. $dP/dz \rightarrow 0$, leading to lower noise.

Raman amplification of OAM modes is especially interesting because the intensity profiles of the different OAM modes are nearly identical. This is very different from the case of LP modes, where e.g. the fundamental mode has the intensity maximum in the center of the fiber, while the LP_{11} mode has zero intensity in the center of the fiber, see Fig. 2.1. Raman amplification depends on the intensity overlap between the pump and the signal [64], and thus, if they are propagating in LP modes with little spatial overlap, the amplification will be small. Additionally, if different signal modes have a different overlap with the pump, the signals will be unevenly amplified, i.e. a mode dependence of the gain, also known as differential mode gain, is seen. The spatial intensity distribution of OAM modes, means that they have the potential to avoid these issues, making them ideal for multi-mode Raman amplification.

5.2 Raman theory

Typically Raman amplification in SMFs is treated in the scalar case, and is well described as [24, 65]

$$\frac{dP_s}{dz} = g(P_p^+ + P_p^-)P_s - \alpha_s P_s, \tag{5.1}$$

$$\pm\frac{dP_p^\pm}{dz} = -\frac{\omega_p}{\omega_s} g P_p^\pm P_s - \alpha_p P_p^\pm, \tag{5.2}$$

where P_s is the signal power P_p^+ is the forward propagating pump power, P_p^- is the backward propagating pump power, α_s and α_p are the fiber loss coefficients for the signal and the pump, respectively, and ω_s, ω_p are the angular frequencies of the signal and the pump, respectively. g is the Raman gain experienced by the signal, and is given as

$$g = \frac{g_R}{A_{\text{eff}}}, \tag{5.3}$$

where g_R is the Raman gain coefficient, which is determined by the fiber material composition, wavelengths and polarization states of the pump and the signal. In silica fibers, g_R is maximized when the pump frequency is ~13.2 THz larger than the signal frequency, and when the signal and the pump are co-polarized [65]. If the signal and pump polarizations are orthogonal, $g_R \sim 0$ [24]. A_{eff} is the effective mode area, which is assumed to be equal for the signal and the pump, and is calculated as

$$A_{\text{eff}} = \frac{\left(\int I \, \mathrm{d}A\right)^2}{\int I^2 \, \mathrm{d}A}, \tag{5.4}$$

where I is the intensity profile of the fiber mode. This set of coupled equations can be solved numerically. If the pump power is much larger than the signal power, the pump depletion term in Eq. (5.2) can be neglected, which allows an analytic solution

$$G_{\text{on}-\text{off}} = \exp\left(g P_0 L_{\text{eff}}\right), \tag{5.5}$$

where $G_{\text{on}-\text{off}}$ is the on-off gain, and P_0 is the total input pump power. The on-off gain is defined as the ratio between the output signal power when the pump is off, and the output signal power when the pump is on. This is different from the net gain, which is typically defined as the ratio of the input signal power and the output signal power. The difference between these two gain figures is the signal propagation loss. For distributed amplifiers, the on-off gain is typically used, because the transmission loss cannot be removed in any case. L_{eff} is the effective fiber length, which is less than the actual fiber length because of pump losses, and is given as

$$L_{\text{eff}} = \frac{1 - \exp\left(\alpha_p L\right)}{\alpha_p}. \tag{5.6}$$

For convenience, Eq. (5.5) is also given in dB, with the units of the variables as superscripts, since this will be used later

$$G_{\text{on}-\text{off}}^{\text{dB}} = \frac{10}{\ln(10)} \, g^{\mathrm{W}^{-1}\mathrm{m}^{-1}} \, P_0^{\mathrm{W}} \, L_{\text{eff}}^{\mathrm{m}}. \tag{5.7}$$

These equations cannot directly be used in the case where the pump and the signal propagate in different modes, since the different modes have different spatial intensity distributions. Additionally, the equations do not account for the case where the same mode has different intensity distributions at different wavelengths. In SMFs this is not a problem in general, but in some fibers supporting HOMs, this effect can be significant, especially close to the cutoff wavelength.

Here, we stay within the scalar theory, and consider the case where the pump has an intensity distribution I_p corresponding to a given mode and a given wavelength. The signal has the intensity distribution I_s, also corresponding to a given mode and a given wavelength.

The major difference in the case of different signal and pump modes is that the Raman overlap is not A_{eff} but rather the intensity overlap between the modes. Following the methods presented in [64, 66], but in the scalar case, rather than the full vectorial case, this overlap is written as

$$\bar{A}_{\text{eff}} = \frac{\int I_p \, \mathrm{d}A \int I_s \, \mathrm{d}A}{\int I_p I_s \, \mathrm{d}A}, \tag{5.8}$$

The material parameter g_R is also a function of the spatial position within the fiber, and thus should be included in this integral. For many fiber designs, this difference may be insignificant. However the air-core OAM fiber has an air core, a highly doped guiding region, and a silica cladding, and this means that the Raman activity of the materials is very different. Accounting for this, we get

$$\bar{g} = \frac{\int I_p I_s g_R \, \mathrm{d}A}{\int I_p \, \mathrm{d}A \int I_s \, \mathrm{d}A}. \tag{5.9}$$

5.2.1 Estimation of Raman gain in OAM fiber

In order to evaluate $\bar{g}$, using the theory described in the previous section, the intensity profiles of the desired modes, and the Raman gain coefficient as a function of the transverse spatial position in the fiber are needed. As described in Sec. 2.1.3, the refractive index profile of the fiber was measured, and using that data, the fiber modes were calculated using a full vectorial mode solver. This gives the $\boldsymbol{E}$ and $\boldsymbol{H}$ fields, and the intensity profiles are calculated from those, as the z component of the Poynting vector.

g_R is calculated using [67], where it was determined that for Germanium doped silica, the refractive index change relative to undoped silica is

$$\Delta n = 1.47 \times 10^{-3} \times \text{mol\%}\,\text{GeO}_2, \tag{5.10}$$

and in [68] the peak Raman gain coefficient is found to be

$$g_R = (1 + 0.08 \times \text{mol\%}\,\text{GeO}) \times g_{R,\,\text{SiO}_2}. \tag{5.11}$$

Thus, from the index profile, g_R can be calculated as

$$g_R(r) = [\Delta n(r) \times 54.4 + 1] \times g_{R,\ \text{SiO}_2}, \tag{5.12}$$

Table 5.1: Calculated Raman gains g, in units of $\mathrm{W}^{-1}\,\mathrm{km}^{-1}$ for all combinations of pump and signal modes.

	Pump OAM mode			
Signal OAM mode	**5a**	**7a**	**5aa**	**7aa**
5a	1.17	1.10	1.17	1.09
7a	1.13	1.14	1.14	1.13
5aa	1.17	1.10	1.17	1.10
7aa	1.13	1.13	1.13	1.13

with

$$g_{R,\,\mathrm{SiO_2}} \sim \frac{1\times10^{-19}\,\mathrm{m^2/W}}{\lambda_p}. \tag{5.13}$$

where λ_p is the pump wavelength [24]. This method of estimating g_R from Δn agrees with the investigations in [69] when the germanium concentration is ~20 %, which is the case in the air-core fiber. The results of these calculations are given in Tab. 5.1. It is noted the all pump and signal combinations results in similar theoretical gains, which is expected, because of the circular intensity profiles.

5.3 Raman amplification of OAM modes using a CW pump in a superposition of modes

This section examines the case where one or several signals, in pure OAM modes are amplified by a pump in a superposition of fiber modes. This section is based on results originally published in [70] and [71].

As described in Sec. 3.3 OAM modes are typically excited using either SLMs or q-plates. These devices are both based on liquid crystals, and therefore the power handling is limited. The SLMs used during the experiments in this thesis can handle average powers up to 1 W according to the manufacturer, and the q-plates have a similar power tolerance. If this power is exceeded, the liquid crystals starts to heat up, eventually reaching the boiling point, where the device is destroyed.

Raman amplification is a nonlinear process, and thus requires large pump powers. The effective mode area of the OAM modes in the air-core fiber is ~160 µm^2, and thus the pump power should be doubled compared to SMF. As a consequence, other methods of coupling the pump to the air-core fiber are needed. Here, the case where the pump is offset coupled to the air-core fiber, resulting in a superposition of modes, is examined.

5.3.1 Raman amplification of a single OAM mode using a CW pump

Experimental setup

The experimental setup is shown in Fig. 5.1, where a tunable ECL is launched into the 8-mode air-core fiber, using an SLM, as described in Sec. 3.3. Thus exciting a single

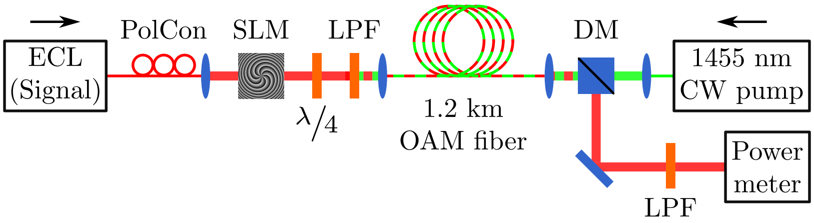

Figure 5.1: Schematic of the experimental setup. ECL: external cavity laser, PolCon: polarization controller, SLM: spatial light modulator, $\lambda/4$: quarter-wave plate, LPF: long-pass filter, DM: dichroic mirror.

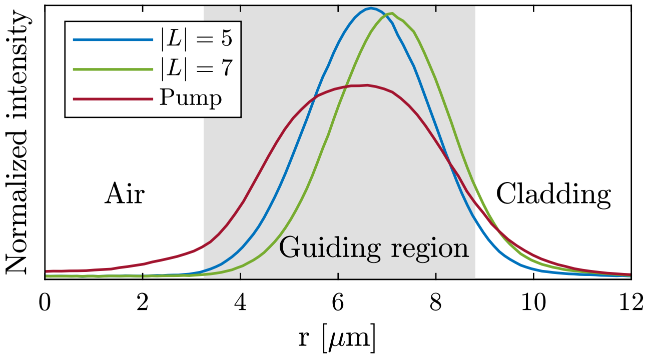

Figure 5.2: Radial intensity distributions of the $|L| = 5$ modes, the $|L| = 7$ modes, and the pump. Each curve is normalized such that the area, corresponding to the power, is unity.

OAM mode with purity of at least −17 dB, measured using time of flight, as described in Sec. 3.5.2. The fiber is backward pumped, using a 1455 nm unpolarized CW Raman laser, which is offset coupled to the fiber without any beam shaping. Thus the pump is not coupled to a pure fiber mode, but to a superposition of several modes. At the input end (for the signal) a long pass filter is used to make sure that the pump does not hit the SLM. At the output of the fiber, the signal is separated from the pump using a dichroic mirror and a long pass filter. The long pass filter is not strictly needed, but improves the spectral filtering significantly compared to only using the dichroic mirror. The signal power is measured using a free-space power meter.

The intensity distributions of the pump and the OAM modes are characterized using an InGaAs camera, and the averaged radial profiles are shown in Fig. 5.2. Each mode is normalized such that the area, corresponding to the power, is unity. It is seen that the intensity distributions do overlap, but that the pump is wider than the signals.

The input signal power is set to −20 dBm, and is swept from 1530 nm to 1570 nm with the pump turned off. The output power is recorded. The pump is turned on and the signal is swept again. This is repeated for pump powers between 15 dBm and 25 dBm, which is the maximum output power from the used pump. Finally, the signal is turned off, and the pump power is swept while the amplified spontaneous emission (ASE) power is recorded.

The pump propagation loss and coupling loss are calculated by measuring the input power and the output power, followed by cutting back the fiber to a length of ∼1 m, without changing the input end, and then measuring the output power again, and subtracting the results. This yielded a pump coupling loss of 0.8 dB, and a pump propagation loss of 6 dB/km. This propagation loss does not correspond with the measurements shown in Fig. 3.8, because the pump is in a superposition of modes.

The on-off gain can then be calculated by subtracting the ASE power from the amplified signal power, and dividing by the unamplified signal power, all in linear units

$$G^{\text{lin}}_{\text{on}-\text{off}} = \frac{P^{\text{W}}_{\text{sig, pump on}} - P^{\text{W}}_{\text{ASE, pump on}}}{P^{\text{W}}_{\text{sig, pump off}}}. \tag{5.14}$$

Results

The results are shown in Fig. 5.3, where the left panel shows a power sweep averaged over the peak wavelengths, and the right panel shows a wavelength sweep at maximum pump power. Triangle markers indicate modes with σ^+ polarization, while circles indicate modes with σ^- polarization. The colors indicate the handedness i.e. spin orbit aligned or spin orbit anti-aligned of the modes, using the same convention as the previous chapters. The black lines in the left panels are least squares linear fits to the $|L| = 5$ and $|L| = 7$ modes, with the top line being the $|L| = 5$ modes.

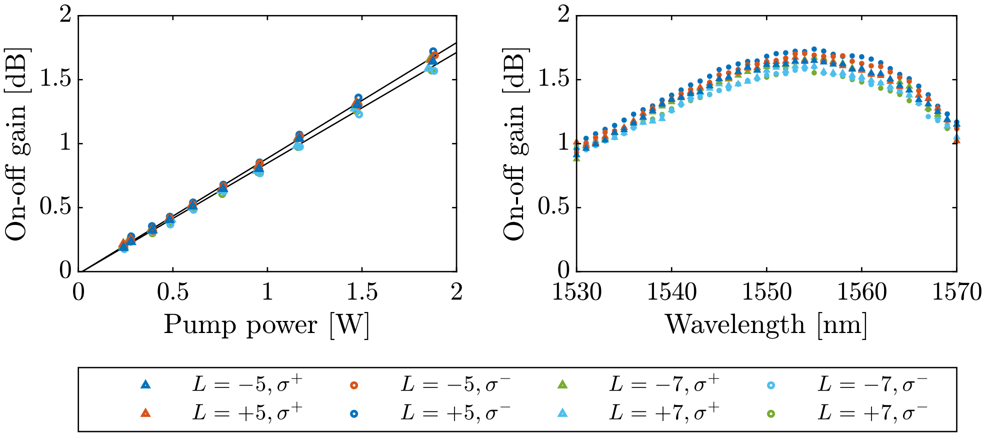

Figure 5.3: Results of the Raman amplification measurements. The left panel shows a power sweep, and the right panel shows a wavelength sweep.

It is seen that the gain in dB is linear with the pump power, as predicted by Eq. (5.7). Furthermore, it is seen that the $|L| = 5$ modes exhibit a slightly larger gain than the $|L| = 7$ modes. No consistent dependence of polarization or handedness is observed, which is expected since an unpolarized pump was used. The gain difference is examined by fitting a line to the $|L| = 5$ and the$|L| = 7$ modes, respectively. The slope is found to be 0.90 dB/W, for the $|L| = 5$ modes, and 0.86 dB/W, for the $|L| = 7$ modes, leading to a differential mode gain of 0.04 dB/W.

The expected gain can be estimated by evaluating Eq. (5.9) using g_R as computed in Sec. 5.2.1 and the experimentally measured intensity profiles presented in Fig. 5.2. This leads to an expected gain of 1.05 dB/W and 0.97 dB/W for the $|L| = 5$ and $|L| = 7$ modes, respectively. Thus the measured gain is on average 13 % lower than expected.

Peak gain is observed for a wavelength of 1555 nm, corresponding to a frequency offset of 13.25 THz, thus agreeing with the theory.

5.3.2 Simultaneous Raman amplification of several OAM modes using a CW pump

Experimental setup

The investigations of the previous section are expanded by launching several modes simultaneously. This is done in order to examine, if in this case, one mode may "steal" the gain from another mode, resulting in a large differential mode gain. This situation is most likely to happen if $\bar{g}$ is different for the co-propagating modes, and the pump is depleted. The experimental setup is modified as shown in Fig. 5.4, enabling excitation of all four $|L| = 7$ modes at the same time. The signal ECL is launched into a 3 dB splitter, and the paths are decorrelated using 10 m SMF. The paths are aligned to the axes of a fiber PBS, and the outputs are decorrelated using 5 m SMF. This creates two orthogonal polarization states in each of the two outputs, effectively emulating a polarization multiplexed signal. Coherence control is enabled on the ECL, to ensure that the used 5 m of decorrelation is sufficient. The two outputs are collimated, and q-plates are used for mode excitation, since each q-plate allows excitation of two modes, thereby reducing the number of free-space beams by a factor of two, compared to using SLMs. The two beams are combined in a beam splitter, and are coupled to the 8-mode OAM fiber.

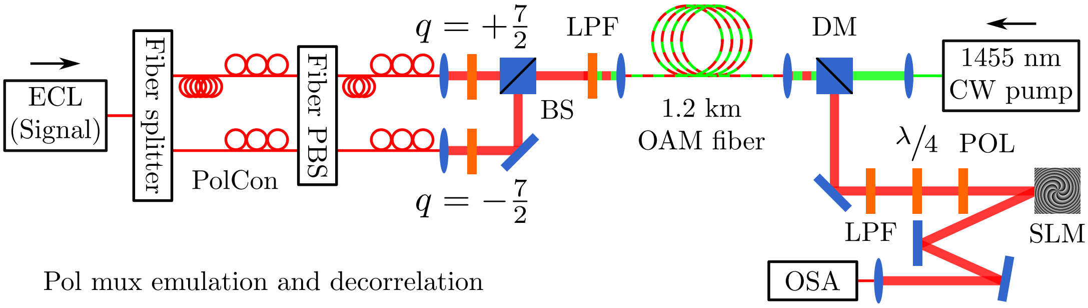

Figure 5.4: Schematic of the experimental setup. ECL: external cavity laser, PolCon: polarization controller, BS: beam splitter, LPF: long-pass filter, DM: dichroic mirror, $\lambda/4$: quarter-wave plate, POL: linear polarizer SLM: spatial light modulator, optical spectrum analyzer (OSA): optical spectrum analyzer.

At the output, the modes are demultiplexed, using a circular polarizer comprised of a quarter-wave plate and a linear polarizer and an SLM that projects each mode onto a Gaussian-like mode that can be coupled to a SMF. This creates a mode filter, enabling measurement of the gain in each mode. Finally, the power is measured using an OSA.

Compared to the setup used in the previous section, the OSA enables spectral filtering of the out of band ASE, thereby improving the measurements. The pump launching scheme using offset coupling, dichroic mirror and long pass filters, is identical to the previous setup.

In addition to the pictured setup, a modification where the signal is amplified using two EDFAs after the fiber PBS, was also used in order to investigate the effects of gain saturation.

Results

The results are seen in Fig. 5.5. The left panel shows the results when the four modes are propagating together in the fiber, with an input power of $-20\,\text{dBm}$ each, resulting in a total signal power of $-14\,\text{dBm}$. In this case, the fit shows a slope of $0.86\,\text{dB/W}$ which is identical with the case where a single mode was excited at a time. However, with four modes propagating simultaneously in the fiber, the difference between the largest gain and the smallest gain is $0.16\,\text{dB}$, while it was $0.09\,\text{dB}$ in the previous case. This shows that there may be some interaction between the modes, but that it is minimal.

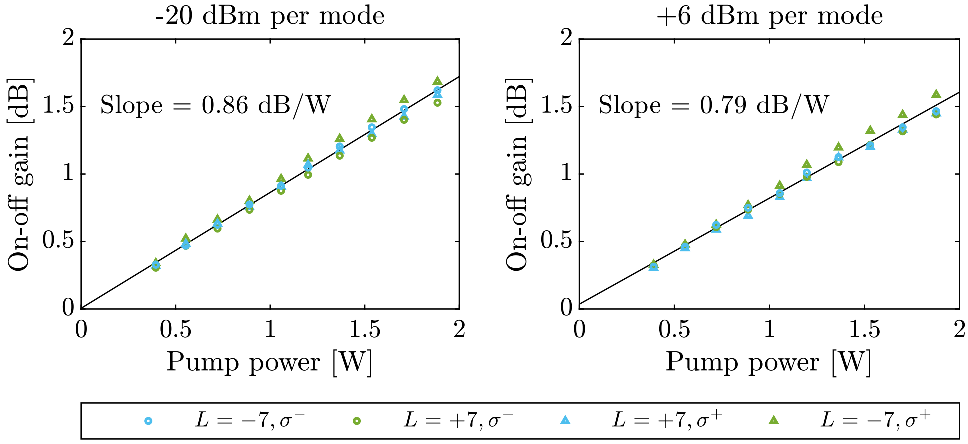

Figure 5.5: Results of the Raman amplification measurements. The left panel shows a power sweep with a signal power of $-20\,\text{dBm}$ per mode, and the right panel shows a power sweep with a signal power of $6\,\text{dBm}$. Gain saturation of $0.05\,\text{dB/W}$ is observed.

The right panel shows the case where two EDFAs are used to boost the signal power to $6\,\text{dBm}$ per mode. In this case, the slope is decreased to $0.79\,\text{dB/W}$, showing a degree of gain saturation. The differential mode gain is $0.15\,\text{dB}$, showing that the modes also share the gain well in the slightly saturated case. The measured spectral dependence is identical to the previous experiment, and is therefore not repeated here.

5.3.3 Scalability

It is clear that Raman amplification in the air-core fiber requires large pump powers in order to reach significant gains. Using the measured gain per pump power, it is estimated that in order to reach a gain of ~15 dB, a pump power of 17 W is needed. This would lead to a gain of 15.4 dB for the $|L| = 5$ modes, and 14.7 dB for the $|L| = 7$ modes, resulting in a differential mode gain of 0.7 dB.

In theory, there is no reason why scaling the pump power should not work, although, in practice, it may be difficult. Alternatively, the gain could be increased by reducing the fiber loss at the pump wavelength, leading to a significantly longer effective length.

5.4 Raman amplification of an OAM mode using a pump in a single OAM mode

The previous section described the situation where an unpolarized pump in a superposition of modes amplified an OAM mode. In order to better understand the nonlinear dynamics on a more fundamental level, this section examines the situation where a signal propagating in a single, pure OAM mode, is amplified by a pump, also propagating in a single pure OAM mode.

As previously explained, the liquid crystal based SLMs and q-plates cannot handle large average powers, and therefore a scheme using a pulsed pump and a pulsed signal is adopted. A CW pump is emulated by using a long pump pulse and a short signal pulse. The pulses are then timed such that even though the group velocities for the pump and the signal are different, the signal always propagates "inside" the pump, as shown in Fig. 5.6.

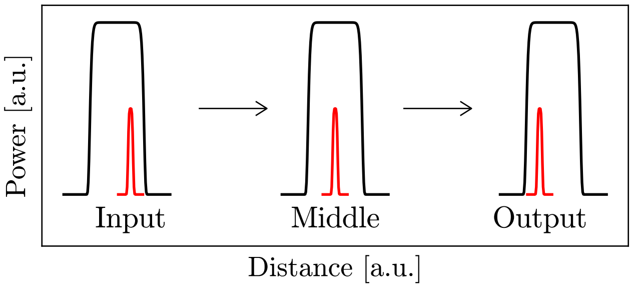

Figure 5.6: Sketch of the principle of the pulsed Raman amplification measurements, in the case where the pump (black) propagates faster than the signal (red).

5.4.1 Experimental setup

The experimental setup is shown in Fig. 5.7. Two tunable ECLs are used as pump and signal sources, respectively. The pump is set to 1470 nm, and the signal is set to 1571.7 nm in order to achieve a 13.2 THz frequency difference. This set of wavelengths is chosen because the fiber propagation loss decreases with the wavelength as shown in Fig. 3.8, and thus a long pump wavelength is desirable. Minimizing the pump loss, in turn maximizes the effective Raman length, as described in Eq. (5.6), thereby maximizing the Raman gain. However, the $|L| = 7$ modes have wavelength cutoff at $\sim$ 1580 nm, and thus the signal has to be below this wavelength.

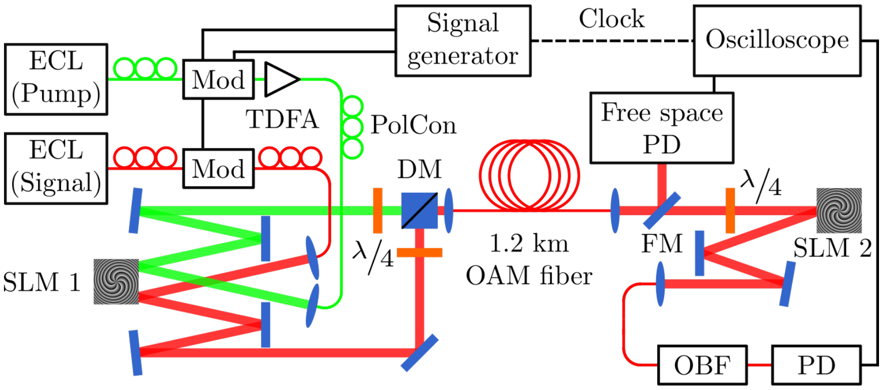

Figure 5.7: Schematic of the experimental setup. Red indicates the signal path, and green indicates the pump path. ECL: external cavity laser, MOD: modulator, TDFA: thulium doped fiber amplifier, PolCon: polarization controller, DM: dichroic mirror, $\lambda/4$: quarter-wave plate, SLM: spatial light modulator, FM: flip mirror, PD: photodetector, OBF: optical band-pass filter.

The signal and pump are modulated using standard telecom intensity modulators, driven directly using an radio frequency (RF) signal generator. The signal is modulated to 1 ns pulses, while the pump is modulated to 50 ns pulses. The period is set to 50 µs in order to achieve a duty cycle of 1/1000. The long pump pulse is needed because the maximum walk-off between the fastest pump mode and the slowest signal mode is ∼41 ns in the 1.2 km fiber. Using a 1 ns signal pulse, this means that the minimum pump duration should be 42 ns, but, 50 ns is chosen to allow for rise- and fall times and to add some tolerance for temporal misalignment.

The pump is amplified in a thulium doped fiber amplifier (TDFA), resulting in flat topped pulses with a peak power of 12 W. The signal and the pump are separately collimated and sent into free-space, where they hit SLM 1 in separate spots, allowing for independent pump and signal modes. This SLM is coded with a phase pattern as in Eq. (3.1), with the addition of a blazed grating in order to isolate the diffraction orders spatially, leading to larger mode purity and additionally making the SLM act as a linear polarizer. The blazed grating increases the wavelength sensitivity of the mode excitation, but this is not a problem when monochromatic light is used. The beams are passed through separate quarter-wave plates in order to achieve circular polarization, and combined using a dichroic mirror. The combined beam is focused into the fiber through an aspheric lens with a focal length of 8 mm.

At the output of the fiber, the light is collimated using another 8 mm lens, and detected using either a 5 GHz free-space PD, or a 10 GHz fiber coupled PD. In the case of the fiber coupled PD, the light is passed though a mode filter consisting of a quarter-wave plate and SLM 2. This is programmed with a phase pattern similar to the one used on SLM 1, matching the selected signal mode. Additionally, an optical band-pass filter is used to filter out the pump and ASE, and an electrical 3 GHz low-pass filter (not pictured) is used to reduce the noise. In the case of the free-space PD, a long pass filter is inserted (not pictured) to filter out the pump, but the ASE is not filtered out. In both cases, the signals are digitized using a fast oscilloscope.

The setup is spatially aligned using time of flight measurements, where both the pump and the signal are switched to a 1 ns pulse duration, and detected using the free-space PD. The temporal alignment of the pump and signal pulses is also done using the free-space PD, at the fiber output end, using measured relative propagation delays of all pump and signal combinations.

For each signal and pump mode combination, 50 waveforms consisting of 4096 data-points are acquired, with the pump on, and with the pump off. The sampling window is set to 2 ns, to ensure that the entire signal pulse is captured, and the central 400 points, corresponding to 0.2 ns are used for calculating the gain. This ensures that only the part where the signal pulse has a flat top is used. The gain is calculated by dividing each pump on trace, by the corresponding pump off trace, and then averaging across the resulting 400×50 data points.

The setup is characterized to determine the pump loss, in order to be able to calculate the Raman gain, $\bar{g}$. It is found that the loss in the free-space path was 1.5 dB for the $|L| = 5$ modes, and 1.8 dB for the $|L| = 7$ modes. This is mainly caused by diffraction loss at the SLM. The coupling loss is 2.5 dB and 3.1 dB, while the propagation loss is 4.2 dB and 3.0 dB for the $|L| = 5$ and $|L| = 7$ modes, respectively. Before each series of measurements, the pump power is measured using a −20 dB tap and a fiber PD, as well as using the free-space PD at the output. A fiber attenuator and a free-space neutral density (ND) filter, respectively, is used, and the PDs are characterized, by doing a power sweep with a CW source and a power meter.

Measurements are performed for all 64 combinations of 8 signal modes and 8 pump modes. For each combination the signal is measured in both of the degenerate modes in order to allow for polarization rotation, as observed in Ch. 4, and the results are averaged.

5.4.2 Results

The on-off gain is measured, as described above, and the Raman gain g is calculated using Eq. (5.5). The results are shown in Fig. 5.8, with the 8 signal modes on the vertical axis, and the pump modes on the horizontal axis. A large difference in gain is observed, with a minimum of $0.08\,\mathrm{W}^{-1}\,\mathrm{km}^{-1}$ and a maximum of $0.75\,\mathrm{W}^{-1}\,\mathrm{km}^{-1}$. It is seen that the diagonal, corresponding to having the signal and the pump in the same mode, results in the largest gains, while the super- and sub-diagonal, corresponding to having the signal and the pump in degenerate mode pairs, but with opposite polarizations, show the lowest gains. This corresponds with the expected polarization dependence. Excluding these fields, the remainder of the matrix has a minimum gain of $0.30\,\mathrm{W}^{-1}\,\mathrm{km}^{-1}$, a maximum gain of $0.44\,\mathrm{W}^{-1}\,\mathrm{km}^{-1}$, and an average gain of $0.37\,\mathrm{W}^{-1}\,\mathrm{km}^{-1}$.

It is noted that the case where the pump and signal are both in the $|L| = 7$, a modes, the gain is opposite compared to what is expected, i.e. the gain is larger when the pump and the signal is launched with opposite polarizations.

From previous investigations, as described in Ch. 4, it is well known that polarization rotations happen, when propagating through long sections of air-core OAM fiber. However

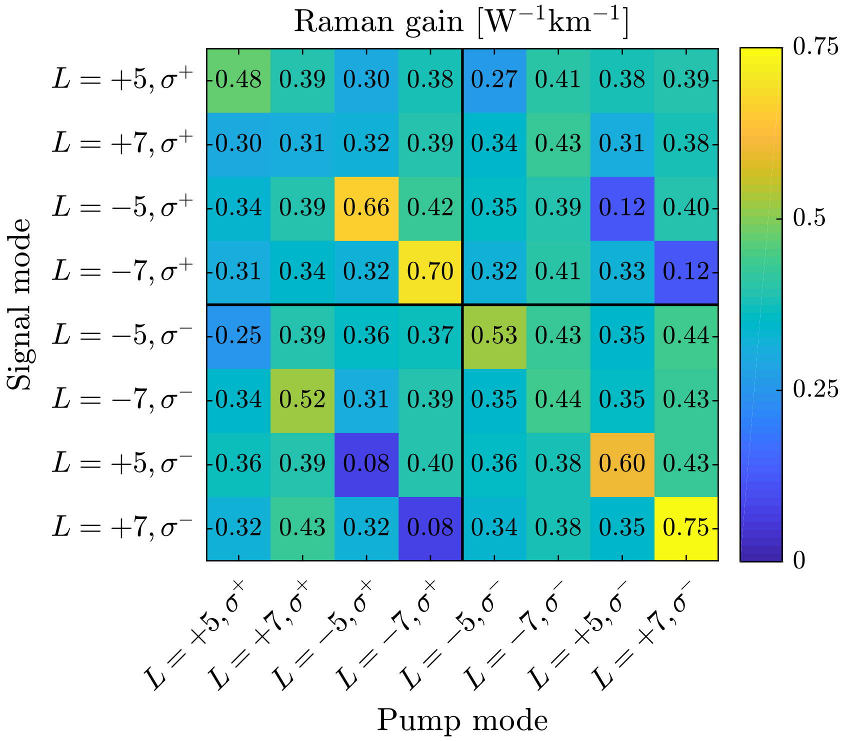

Signal mode \ Pump mode	$L=+5,\sigma^+$	$L=+7,\sigma^+$	$L=-5,\sigma^+$	$L=-7,\sigma^+$	$L=-5,\sigma^-$	$L=-7,\sigma^-$	$L=+5,\sigma^-$	$L=+7,\sigma^-$
$L=+5,\sigma^+$	0.48	0.39	0.30	0.38	0.27	0.41	0.38	0.39
$L=+7,\sigma^+$	0.30	0.31	0.32	0.39	0.34	0.43	0.31	0.38
$L=-5,\sigma^+$	0.34	0.39	0.66	0.42	0.35	0.39	0.12	0.40
$L=-7,\sigma^+$	0.31	0.34	0.32	0.70	0.32	0.41	0.33	0.12
$L=-5,\sigma^-$	0.25	0.39	0.36	0.37	0.53	0.43	0.35	0.44
$L=-7,\sigma^-$	0.34	0.52	0.31	0.39	0.35	0.44	0.35	0.43
$L=+5,\sigma^-$	0.36	0.39	0.08	0.40	0.36	0.38	0.60	0.43
$L=+7,\sigma^-$	0.32	0.43	0.32	0.08	0.34	0.38	0.35	0.75

Figure 5.8: Results of the pulsed Raman measurements. The largest Raman gain is observed in the diagonal, corresponding to identical pump and signal modes.

it is also known that if two orthogonal states with the same wavelength e.g. $L = +7, \sigma^+$ and $L = -7, \sigma^-$ are launched, they remain orthogonal during the entire propagation. In other words, the transformation is unitary, otherwise these orthogonal states could not be used for multiplexing. In Ch. 4, however, a relatively narrow spectrum was used, while here the difference between the signal and the pump is 13.2 THz. Thus, it is concluded that while a signal, or a pump launched into e.g. $L = +7, \sigma^+$ remains orthogonal to a signal or a pump launched into $L = -7, \sigma^-$, respectively, during the entire propagation, a signal launched into $L = +7, \sigma^+$ does not necessarily remain orthogonal to a pump launched into $L = -7, \sigma^-$. Previous investigation [38] suggests that polarization rotation can be completely avoided if the fiber length is reduced to ~10 m, but this would also reduce the Raman gain by two orders of magnitude, and thus it is not a viable option in this case.

In order to avoid the complications relating to the polarization rotation, the four datapoints for each degenerate mode pair are averaged, effectively returning to an unpolarized pump. These averaged results are shown in Fig. 5.9. It is seen that that gain is relatively uniform, but slightly lower across all signal modes when the $|L| = 5$ modes are pumped. In order to evaluate if the measured Raman gains, correspond to the theory of Sec. 5.2 the gains are compared to the values displayed in Tab. 5.1. These values are for the co-polarized case, and thus should be halved, in the unpolarized case. This results in an average expected Raman gain of 0.57 W^{-1} km^{-1}, while the averaged measured Raman gain is 0.37 W^{-1} km^{-1}. This corresponds to the measurements being 34 % lower than expected.

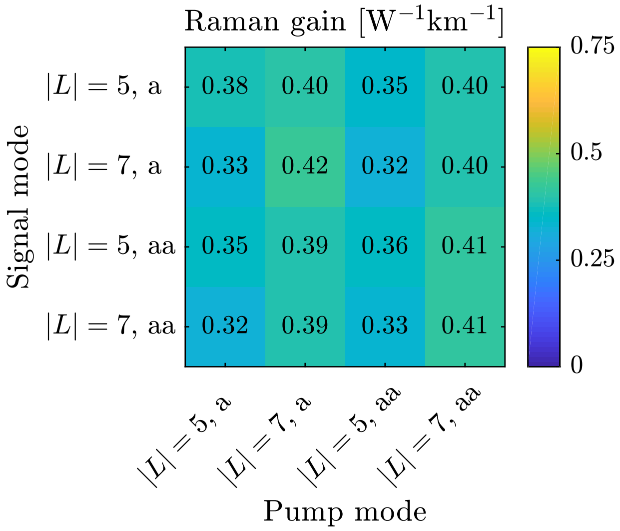

Figure 5.9: Raman gains averaged across polarizations. Similar gains are seen for all combinations.

5.5 Conclusion

Raman amplification of OAM modes was examined in the case where a CW pump in a superposition of modes, was used to amplify one or several pure OAM modes, and in the case where a pump in a pure OAM mode, amplified a signal in a pure OAM mode. The results were compared to a scalar theory, and it was found that in practice the gain was lower than expected. Based on this investigation, it is clear that Raman amplification of OAM modes with low mode dependent gain is possible, but that it requires a significant amount of pump power.

Chapter 6

Few-mode Kramers-Kronig receiver

This chapter is based on experiments performed during the external research stay at NICT in Japan. The results are originally published in [72] and [73].

6.1 Introduction

In recent years, space-division multiplexing (SDM) has attracted significant attention as a way to increase data rates in optical fibers [13]. Moreover, the attractiveness of SDM stems from the potential for integration with high scalability of optical hardware, such as optical amplifiers [74] or optical switches [75] as well as sharing processing resources.

In this chapter, we propose a novel coherent receiver, capable of handling few-mode SDM signals with a front-end structure that is scalable to large numbers of modes. The receiver concept is based on mixing the local oscillator (LO) light with all incoming modes simultaneously, before polarization- and mode-demultiplexing. Detection can be performed using single-ended PDs with a coherent Kramers-Kronig (KK) detection scheme, adapted to few-mode systems [76], which allows reconstruction of the full optical field in the digital domain.

By performing LO mixing and polarization splitting directly on few-mode signals, substantial hardware savings are achieved, compared to traditional receiver structures that are based on mode demultiplexing followed by conventional coherent receivers for each of the spatial modes.

6.2 Few-mode Kramers-Kronig front-end

Fig. 6.1 shows a comparison between the principles of different KK receiver schemes and the proposed scheme. Fig. 6.1(a) shows the conventional single-mode polarization division multiplexing (PDM)-KK receiver [77, 78], where the signal is split into two polarization components by a PBS and combined with a co-polarized LO.

(a) Conventional PDM-KK receiver.

(b) Simplified PDM-KK receiver.

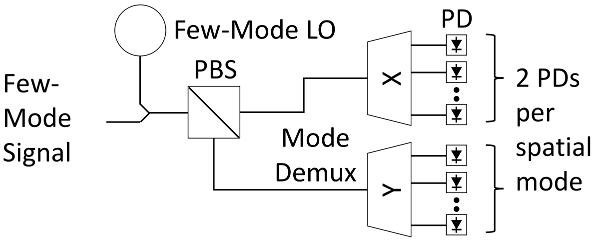

(c) Few-mode PDM-KK receiver.

Figure 6.1: Principle of the few-mode PDM-KK receiver compared to previous PDM-KK receivers.

Fig. 6.1(b) shows a variation of this scheme where the signal is first mixed with an LO which is aligned at 45 degrees with the polarization axis of the PBS [76]. In this way, the outputs of the PBS correspond to the two signal polarization components, co-polarized with equal power components of the LO. Compared to the scheme in Fig. 6.1(a), this reduces the number of 3 dB couplers from 3 to 1.

In the proposed receiver, Fig. 6.1(c), the signal and LO are replaced by a few-mode signal and a few-mode LO. The outputs of the PBS are then single-polarization spatial modes, consisting of co-polarized components of the signal and LO modes. The receiver uses two mode demultiplexers, one for each polarization component. It is noted that although the required mode demultiplexers are dependent on the number of received modes, the signal-LO mixing and polarization splitting are done independently of the number of modes. In addition, a few-mode band-pass filter can be added at the receiver input, to accommodate dense WDM transmission schemes.

Comparing these 3 receiver structures, they all use the same number of PDs, and the LO source can be split and amplified to enable scaling. Scheme (a) and (b), requires a single mode demultiplexer, while scheme (c) requires two. However, only in the case of scheme (c), scaling in the number of spatial modes, is possible without the number of PBSs and 3 dB couplers, rapidly increasing.

6.3 Single wavelength experiment

This section describes an experiment, demonstrating the few-mode KK receiver principle, as explained in the previous section.

6.3.1 Experimental setup

The experimental setup is shown in Fig. 6.2. A narrow-linewidth ($\leq$ 100kHz) ECL at 1546.6 nm is modulated with a 24.5 GBaud PDM-quadrature-amplitude modulation (QAM) signal with root-raised cosine pulses and a roll-off of 0.01, using a dual polarization (DP)-IQ modulator, driven by a 4 channel 49 GS/s arbitrary waveform generator (AWG). The signal is amplified using an EDFA, and attenuated with a variable optical attenuator (VOA). The signal is split in a 3×3 coupler, and the 3 paths are decorrelated by adding two optical delays of 100 ns and 200 ns, respectively, creating 3 spatial channels. The 3 DP signals are multiplexed using a 3D waveguide, mapping the signals onto the LP_{01}, $\mathrm{LP}_{11\mathrm{a}}$ and $\mathrm{LP}_{11\mathrm{b}}$ modes of a 3-mode fiber. The signal is transmitted through a 55 km graded-index 3-mode fiber link, with a loss of 12 dB [79, 80].

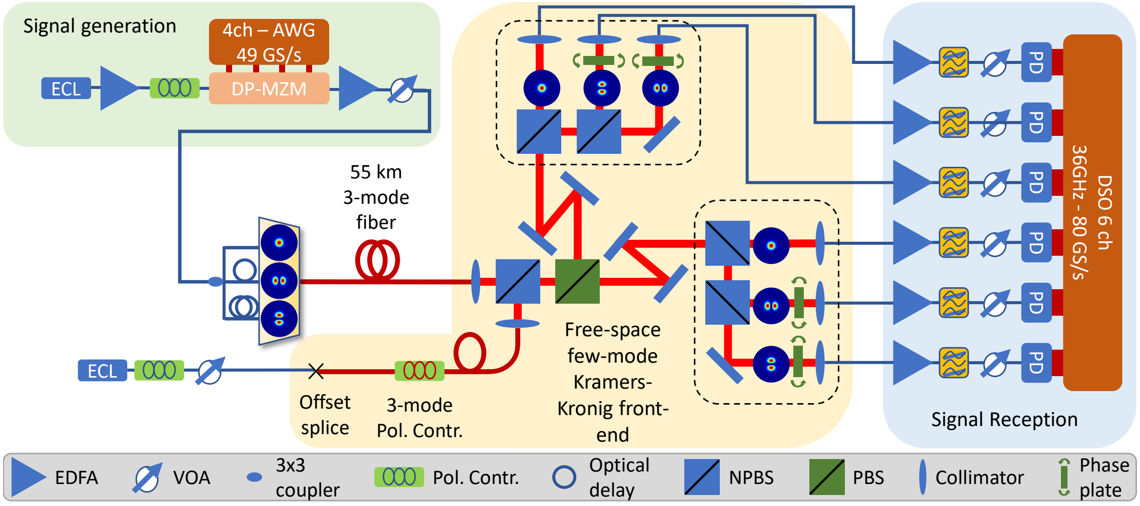

Figure 6.2: Experimental setup of the single wavelength PDM-KK receiver.

The free-space KK receiver consists of 3 stages; LO generation, LO combination, and finally mode demultiplexing. In order to generate the 3-mode LO, a 25 kHz linewidth ECL is tuned at a 12.5 GHz offset from the signal center-wavelength, and passed through a VOA and polarization controller. The SMF output of the polarization controller, is offset spliced to a 5 m segment of graded-index 3-mode fiber in order to excite a superposition of modes. The 3-mode fiber is inserted in a fiber polarization controller with 3×17.5 mm diameter loops in a configuration of 1-2-1 turns. This provides a controlled method to perturb the fiber, and thereby adjust the LO polarization and mode superposition at the fiber output. The 3-mode LO and the 3-mode signal are each collimated into free-space where they are combined in a 3 dB beam splitter. The two collimators have variable focus, and are mounted on stages allowing for x, y, yaw and pitch adjustment. Using these adjustments, the LO and signal beams are co-aligned.

Demultiplexing of the 6 data signals is achieved by passing the beam through a PBS, and then splitting the modes in two separate free-space demultiplexers, marked with dashed lines in Fig. 6.2. Before these demultiplexers, two sets of two dielectric mirrors are used to allow independent steering of the two beams. These demultiplexers operated by splitting the beam in a 3 dB beam splitter, and focusing one part into a SMF. The SMF acts as a pinhole, filtering away the LP_{11} modes. The second beam is split in an additional 3 dB beam splitter, and each output beam is passed though a phase plate. These phase plates converts the LP_{11} mode content, aligned with the axis of the phase plate, to a Gaussian-like intensity profile, that can be coupled to SMF, while converting any LP_{01} content to a LP_{11}-like intensity profile, that is filtered away by the SMF. The two phase plates are adjusted to have a relative angle of 90°, while the remaining parts of the demultiplexers are fixed, and thus cannot be optimized.

The demultiplexing loss for the LP_{01} mode is 4.8 dB while the loss for the LP_{11} modes is 9.0 dB, leading to an average loss of 7.0 dB. The beam splitters gives the demultiplexer a minimum loss of 3 dB for the LP_{01} mode and 6 dB for the LP_{11} modes, before any loss from fiber coupling, and thus the measured losses are as expected.

The LO is aligned such that the power ratios of LO and signal at each of the 6 outputs are identical. This is achieved with the same average loss as the signal, thus confirming that the scheme for generating a 3-mode superposition of the LO is effective. Additionally, it is done with a loss of 1.2 dB from the offset splice and polarization control stage, which is significantly less compared to what can be achieved using a dedicated multiplexer, and similar to what can be expected if using a custom phase plate or computer generated hologram on an SLM to achieve this superposition.

Each of the 6 SMF outputs has a signal to LO ratio of 14 dB, and is individually preamplified and band-pass filtered to reduce the ASE power. The signal is detected using 6 × 40 GHz PDs, and digitized and stored for offline processing with a 6-channel real-time oscilloscope operating at 80 GS/s. The DSP consists of a KK front end operating at 4 samples per symbol to compute the optical fields of the signals, followed by a few-mode digital receiver. The latter consists of a resampling stage to 2 samples per symbol, followed by a least-mean squares 6×6 MIMO equalizer with 117 taps. The equalizer taps are computed using a data-aided algorithm. After convergence, the update of the equalizers is switched to a decision directed algorithm. Carrier recovery is performed within the equalizer loop.

6.3.2 Results

Constellation diagrams of the 6 received modes after transmission are shown in Fig. 6.3. The average Q-factor is 8.5 dB, and the error vector magnitudes (EVMs) are 13.7 %, 13.5 %, 16.2 %, 16.1 %, 17.9 % and 19.2 % for the LP_{01}x, LP_{01}y, LP_{11a}x, LP_{11a}y, LP_{11b}x and LP_{11b}y modes, respectively. It is noted that the LP_{01} modes performs better than the LP_{11} modes, most likely due to their lower demultiplexing loss. Tests are also performed in a back to back configuration, with 1 m of 3-mode fiber. Here, the average Q-factor is 8.9 dB, and thus a 0.4 dB transmission penalty is measured.

The estimated impulse response of the system, computed by running the inverse of the MIMO equalizer, is shown in Fig. 6.4, for both transmission and back to back configurations. In the back to back case, there are two distinct peaks, presumably corresponding the LP_{01} and LP_{11} modes. In the transmission case, the overall shape of the impulse response is preserved, although it is slightly smoothed and the temporal extent is increased

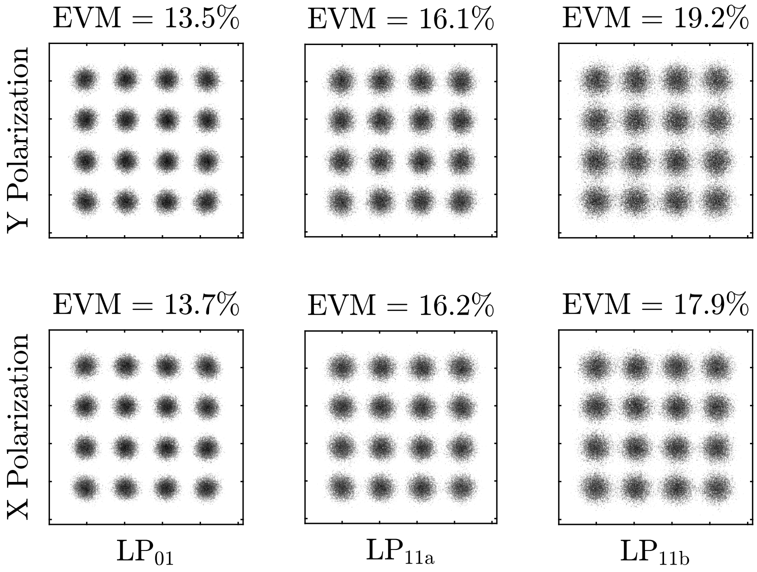

Figure 6.3: Constellations of the received signals.

by ∼0.15 ns. Since the spread of approximately 0.5 ns is present in both cases, it is mainly attributed to different path-lengths in the free-space part of the receiver.

Fig. 6.5 shows the squares of the frequency domain singular values of the channel, calculated as in [81]. A spread can be observed between the six tributaries, and the system mode dependent loss (MDL), here defined as the ratio of the maximum to the minimum of the frequency-averaged squared singular-values, reached 5.6 dB. This is mainly attributed to the demultiplexers. A non-symmetric behavior of the frequency-domain singular values was also observed, in contrast to previous observations with standard coherent receivers [80, 81]. This asymmetry is supposedly induced by the frequency-response of the PDs, as well as the oscilloscope. While the current free-space implementation of the few-mode KK receiver induces a considerable performance penalty, a further reduction of loss and MDL, should be possible when using better mode demultiplexers.

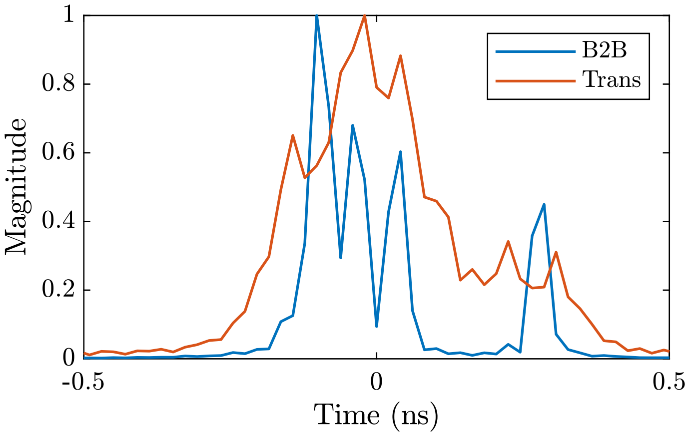

Figure 6.4: Estimated impulse response of the system.

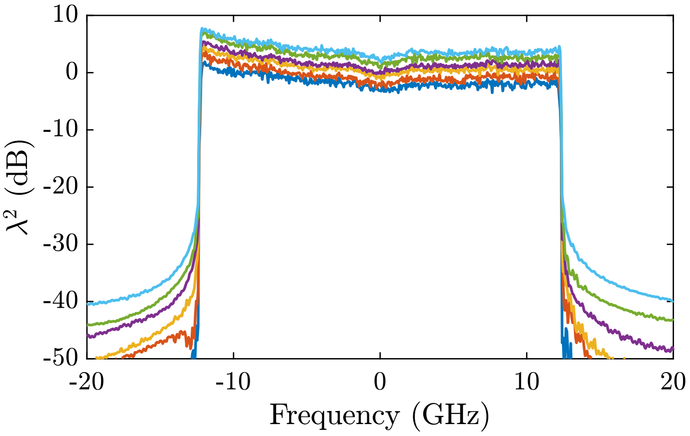

Figure 6.5: Singular values square of the frequency-domain channel matrix.

6.4 WDM experiment

In this section, the few-mode KK receiver from the previous section is extended to WDM operation. Furthermore, the optical amplifiers are removed in order to simplify the setup, and thereby make the receiver more attractive in low cost scenarios.

6.4.1 Experimental setup

The experimental setup is shown in Fig. 6.6. A frequency comb generates carrier lines with 25 GHz spacing. A tunable filter is used to select a pair of neighboring lines which are split, independently modulated in two DP-IQ modulators and optically decorrelated before recombination in a 3 dB coupler. The modulators are driven by a four channel AWG, generating 24.5 GBaud root-raised cosine shaped 16-QAM signals with a roll-off factor of 0.01.

The remaining comb spectrum is modulated in a third DP-IQ modulator, driven by a single electrically decorrelated AWG, generating 24.5 GBaud root-raised cosine shaped 16-QAM dummy channels. A MEMS based optical processor is used to flatten the optical spectrum, as well as to generate the spectral channel assignment, consisting of two adjacent channels with a 25 GHz guard band. The test and dummy channels are separately amplified before combination in a 3 dB coupler with VOAs used for power equalization. The resulting optical spectrum, shown in Fig. 6.7, consists of 16 × 24.5 GBaud channels, occupying a spectrum of 575 GHz. This configuration enables positioning the LO such that the frequency offset to the center of the test channel is 12.5 GHz, while the frequency offset from the center of the nearest neighboring channel is 37.5 GHz. The signal is transmitted through a 55 km graded-index 3-mode fiber link, with a loss of 12 dB [79, 80]. The total launch power into the 3-mode fiber is 19.8 dBm.

After transmission, the 3-mode signals are collimated into free-space, and filtered using a free-space optical band-pass filter in order to select a WDM channel under test. The LO generation and combination is identical to the single-wavelength experiment described in the previous section, except that it is now amplified using an EDFA. As before, polarization demultiplexing is done with a PBS, producing two 3-mode light waves with co-polarized signal and LO modes. Mode demultiplexing is handled using two mode de-

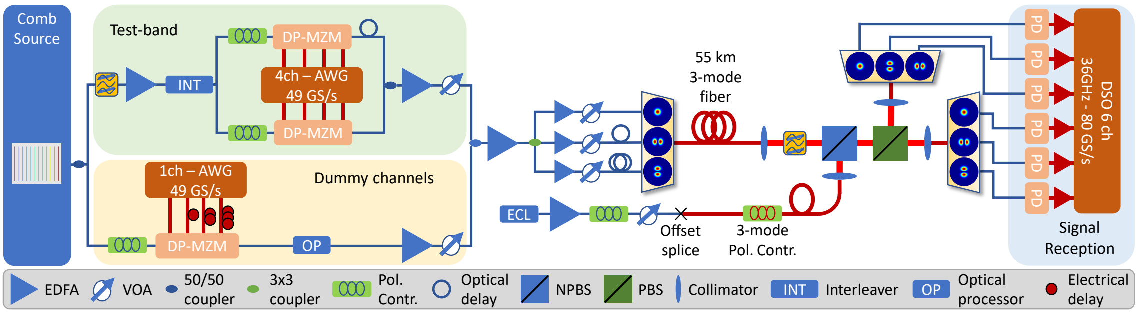

Figure 6.6: Experimental setup of the WDM few-mode KK receiver.

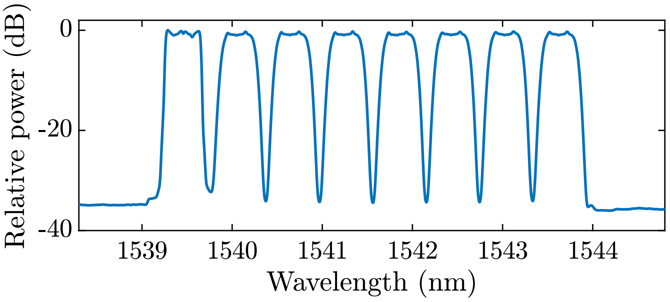

Figure 6.7: Spectrum before transmission, consisting of 16 WDM channels arranged in 8 pairs.

multiplexers based on 3D waveguides, which leads to a fiber coupling and demultiplexing loss of 2.6 dB. This is significantly better than the free-space demultiplexers used in the single-wavelength experiment, and additionally the MDL is less than 1 dB. LO alignment is optimized to achieve similar electrical powers for all of the six demultiplexed channels. After transmission and receiver losses, the input power to each PD is -17.6 dBm per wavelength channel with an LO power of 5 dBm to each PD.

The signals are detected using 6×40 GHz PDs, amplified using electrical amplifiers before being digitized and stored for offline processing in a 6-channel real-time oscilloscope operating at 80 GS/s. The DSP consists of a KK front-end operating at 4 samples per symbol to compute the optical fields of the signals, followed by a few-mode digital receiver. The latter consists of a resampling stage to 2 samples per symbol, followed by a least-mean squares 6×6 MIMO equalizer with 117 taps. The equalizer taps are computed using a data-aided algorithm. After convergence, the update of the equalizers are switched to a decision directed algorithm. Carrier recovery is performed within the equalizer loop.

6.4.2 Results

Fig. 6.8(a) shows the Q-factors of the 16 measured spatial super channels, ranging between 5.4 dB and 7.8 dB. Fig. 6.8(b) shows the resulting data-rates for each channel on the left axis and the required code-rates on the right axis. The higher values are calculated with the generalized mutual information (GMI) [82], indicating the achievable data-rates assuming an ideal code and bit-wise decoding. To assess the data-rates under more realistic conditions, a coding scheme similar to [80], is also implemented using soft-decision low-density parity-check (LDPC) codes [83] to reduce the BER below 2.18×10^{-5} and a further outer HD-FEC with 2.7 % overhead [84] to guarantee error-free transmission. Code-puncturing is implemented, for finer code-rate granularity. The average measured data-rate after LDPC decoding was 548.9 Gbit/s, and the total data-rate is 8.8 Tbit/s, leading to a spectral efficiency of 15.3 bit/s/Hz.

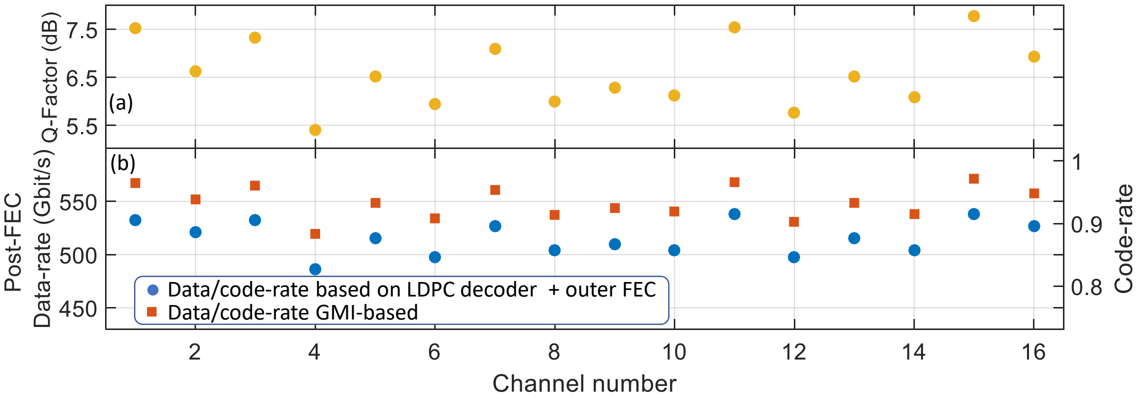

Figure 6.8: Results of the measurements. The top panel (a) shows the Q-factors of the 16 measured spatial super channels, ranging between 5.4 dB and 7.8 dB. The bottom panel (b) shows the data-rates for each channel on the left axis and the required code-rates on the right axis.

6.5 Conclusion

An SDM receiver, which is highly scalable in the number of modes, has been demonstrated. This was done by transmitting 16 WDM spatial super channels over 55 km 3-mode fiber, without the need for optical pre-amplification in the receiver. The receiver made use of KK detection, reducing the number of required PDs by a factor of two. This receiver design may be attractive for short-reach metro or inter-data center links, where low cost is important.

Chapter 7

Conclusion

This thesis has presented the theoretical background for modes in optical fibers, and several experiments were performed demonstrating the use of HOMs for communications purposes.

Starting with Maxwell's equations, a brief introduction to electromagnetic theory was provided, leading to the eigenvalue equations for modes in optical fibers. These equations were discretized, in order to be able to solve the guided modes in a fiber, for a measured refractive index profile. The scalar approximation, leading to LP modes was also examined.

The theory was used to characterize the air-core OAM fiber, supporting stable propagation of 12 OAM states, $L = \pm 5, \sigma^{\pm}$, $L = \pm 5, \sigma^{\mp}$, $L = \pm 6, \sigma^{\pm}$, $L = \pm 6, \sigma^{\mp}$, $L = \pm 7, \sigma^{\pm}$, and $L = \pm 7, \sigma^{\mp}$. Mode excitation in this fiber was examined, using SLMs and q-plates, and the experimental setups for mode excitation were analyzed using Fourier optics. Theoretical coupling losses down to 2.0 dB were found, while in practice the lowest achievable loss was 2.5 dB. Experimental characterizations of the air-core fiber were performed, the loss was measured, and found to be ~0.8 dB/km in the C-band, with increasing loss at shorter wavelengths. The purity of modes was examined using the time of flight method, and excitation of modes with at least −17 dB, corresponding to 98 % was found to be achievable. Finally, the intensity- and phase distributions of the modes were studied.

The 1.2 km, 12-mode air-core OAM fiber was used in a transmission experiment, resulting in the largest number of simultaneously transmitted fiber modes, without the need of MIMO processing. The crosstalk of the system was analyzed, and found to be the main limiting factor of the achievable data-rates. It was concluded that the crosstalk could be significantly improved by using a better multiplexing technique.

Raman amplification of OAM modes, in the air-core fiber was studied experimentally, as a possible alternative to a complicated OAM EDFA. It was found that Raman amplification in the air-core fiber is possible, and that the Raman gain can compensate the propagation loss. However, the large loss at the pump wavelength, and the large effective area of the fiber modes resulted in a need for large pump powers, in order to extract meaningful gains.

A novel receiver structure, utilizing SDM resource sharing, and KK detection, was proposed. This was successfully demonstrated in transmission experiments with LP modes in graded-index few-mode fiber (FMF), in both the single-wavelength case, and the WDM case.

Thus, this thesis has examined SDM using both OAM and LP modes, corresponding to two different scenarios. OAM modes are offering uncoupled channels, over short propagation lengths, and thus there is no need for MIMO processing, leading to low latency and power consumption. LP mode based systems, on the other hand, requires MIMO processing, but can be implemented using simpler fibers, and offers the possibility of MDM in long distance communications systems.

Continuing the work within the field of SDM using OAM modes, it would be interesting to explore propagation of these modes in longer fibers, and thereby explore the distance limit of MIMO-free MDM. Increasing the number of modes would also be highly interesting. Currently this is limited by the available fibers, but also by the multiplexing and demultiplexing techniques. Therefore new, and more practical mode multiplexers and demultiplexers for OAM modes will enable significant progress in this field.

Bibliography

[1] K. Kao and G. Hockham, “Dielectric-fibre surface waveguides for optical frequencies,” Proceedings of the Institution of Electrical Engineers **113**, 1151–1158 (1966).

[2] F. P. Kapron, D. B. Keck, and R. D. Maurer, “RADIATION LOSSES IN GLASS OPTICAL WAVEGUIDES,” Applied Physics Letters **17**, 423–425 (1970).

[3] R. Mears, L. Reekie, I. Jauncey, and D. Payne, “Low-noise erbium-doped fibre amplifier operating at 1.54μm,” Electronics Letters **23**, 1026 (1987).

[4] C. E. Shannon, “A Mathematical Theory of Communication,” Bell System Technical Journal **27**, 379–423 (1948).

[5] P. P. Mitra and J. B. Stark, “Nonlinear limits to the information capacity of optical fibre communications,” Nature **411**, 1027–1030 (2001).

[6] E. B. Desurvire, “Capacity Demand and Technology Challenges for Lightwave Systems in the Next Two Decades,” Journal of Lightwave Technology **24**, 4697–4710 (2006).

[7] A. Ellis, Jian Zhao, and D. Cotter, “Approaching the Non-Linear Shannon Limit,” Journal of Lightwave Technology **28**, 423–433 (2010).

[8] R. Kashyap and K. Blow, “Observation of catastrophic self-propelled self-focusing in optical fibres,” Electronics Letters **24**, 47–49 (1988).

[9] A. Chralyvy, “Plenary paper: The coming capacity crunch,” in *2009 35th European Conference on Optical Communication,* (2009), p. 1.

[10] D. J. Richardson, “Filling the light pipe,” Science **330**, 327–328 (2010).

[11] T. Morioka, “New Generation Optical Infrastructure Technologies: “EXAT Initiative” Towards 2020 and Beyond,” in *2009 14th OptoElectronics and Communications Conference,* (IEEE, 2009), pp. 1–2.

[12] R.-J. Essiambre and R. W. Tkach, “Capacity Trends and Limits of Optical Communication Networks,” Proceedings of the IEEE **100**, 1035–1055 (2012).

[13] D. J. Richardson, J. M. Fini, and L. E. Nelson, “Space-division multiplexing in optical fibres,” Nature Photonics **7**, 354–362 (2013).

[14] K. Saitoh and S. Matsuo, "Multicore Fiber Technology," Journal of Lightwave Technology **34**, 55–66 (2016).

[15] B. J. Puttnam, R. S. Luis, E. Agrell, G. Rademacher, J. Sakaguchi, W. Klaus, G. M. Saridis, Y. Awaji, and N. Wada, "High Capacity Transmission Systems Using Homogeneous Multi-Core Fibers," Journal of Lightwave Technology **35**, 1157–1167 (2017).

[16] K.-i. Kitayama and N.-P. Diamantopoulos, "Few-Mode Optical Fibers: Original Motivation and Recent Progress," IEEE Communications Magazine **55**, 163–169 (2017).

[17] D. Soma, Y. Wakayama, S. Beppu, S. Sumita, T. Tsuritani, T. Hayashi, T. Nagashima, M. Suzuki, H. Takahashi, K. Igarashi, I. Morita, and M. Suzuki, "10.16 Peta-bit/s Dense SDM/WDM transmission over Low-DMD 6-Mode 19-Core Fibre Across C+L Band," in *2017 European Conference on Optical Communication (ECOC),* (IEEE, 2017), pp. 1–3.

[18] R. Ryf, S. Randel, A. H. Gnauck, C. Bolle, A. Sierra, S. Mumtaz, M. Esmaeelpour, E. C. Burrows, R.-J. Essiambre, P. J. Winzer, D. W. Peckham, A. H. McCurdy, and R. Lingle, "Mode-Division Multiplexing Over 96 km of Few-Mode Fiber Using Coherent 6x6 MIMO Processing," Journal of Lightwave Technology **30**, 521–531 (2012).

[19] L. Wang, R. M. Nejad, A. Corsi, J. Lin, Y. Messaddeq, L. Rusch, and S. LaRochelle, "Linearly polarized vector modes: enabling MIMO-free mode-division multiplexing," Optics Express **25**, 11736 (2017).

[20] A. M. Yao and M. J. Padgett, "Orbital angular momentum: origins, behavior and applications," Advances in Optics and Photonics **3**, 161 (2011).

[21] S. Ramachandran and P. Kristensen, "Optical vortices in fiber," Nanophotonics **2**, 455–474 (2013).

[22] P. Gregg, P. Kristensen, and S. Ramachandran, "13.4km OAM state propagation by recirculating fiber loop," Optics Express **24**, 18938 (2016).

[23] D. Griffiths, *Introduction to electrodynamics* (Prentice Hall, 1999), 3rd ed.

[24] G. P. Agrawal, *Nonlinear Fiber Optics* (Elsevier Inc., 2012), 5th ed.

[25] K. Okamoto, *Fundamentals of optical waveguides* (Elsevier, 2006), 2nd ed.

[26] R. Song, J. Zhu, and X. Zhang, "Full-vectorial modal analysis for circular optical waveguides based on the multidomain Chebyshev pseudospectral method," Journal of the Optical Society of America B **27**, 1722 (2010).

[27] J. Lægsgaard, "Introduction to dielectric waveguides," (2014).

[28] R. A. Beth, "Mechanical Detection and Measurement of the Angular Momentum of Light," Physical Review **50**, 115–125 (1936).

[29] J. H. Poynting, “The Wave Motion of a Revolving Shaft, and a Suggestion as to the Angular Momentum in a Beam of Circularly Polarised Light,” Proceedings of the Royal Society A: Mathematical, Physical and Engineering Sciences **82**, 560–567 (1909).

[30] L. Allen, M. W. Beijersbergen, R. J. C. Spreeuw, and J. P. Woerdman, “Orbital angular momentum of light and the transformation of Laguerre-Gaussian laser modes,” Physical Review A **45**, 8185–8189 (1992).

[31] D. L. Andrews and M. Babiker, eds., *The Angular Momentum of Light* (Cambridge University Press, Cambridge, 2012).

[32] K. Y. Bliokh, F. J. Rodríguez-Fortuño, F. Nori, and A. V. Zayats, “Spin–orbit interactions of light,” Nature Photonics **9**, 796–808 (2015).

[33] S. Ramachandran, P. Kristensen, and M. F. Yan, “Generation and propagation of radially polarized beams in optical fibers.” Optics letters **34**, 2525–2527 (2009).

[34] N. Bozinovic, S. Golowich, P. Kristensen, and S. Ramachandran, “Control of orbital angular momentum of light with optical fibers,” Optics Letters **37**, 2451 (2012).

[35] N. Bozinovic, Y. Yue, Y. Ren, M. Tur, P. Kristensen, H. Huang, A. E. Willner, and S. Ramachandran, “Terabit-scale orbital angular momentum mode division multiplexing in fibers.” Science (New York, N.Y.) **340**, 1545–8 (2013).

[36] R. M. Nejad, K. Allahverdyan, P. Vaity, S. Amiralizadeh, C. Brunet, Y. Messaddeq, S. LaRochelle, and L. A. Rusch, “Mode Division Multiplexing Using Orbital Angular Momentum Modes Over 1.4-km Ring Core Fiber,” Journal of Lightwave Technology **34**, 4252–4258 (2016).

[37] C. Brunet, P. Vaity, Y. Messaddeq, S. LaRochelle, and L. a. Rusch, “Design, fabrication and validation of an OAM fiber supporting 36 states.” Optics express **22**, 26117–27 (2014).

[38] P. Gregg, P. Kristensen, and S. Ramachandran, “Conservation of orbital angular momentum in air-core optical fibers,” Optica **2**, 267 (2015).

[39] P. Gregg, P. Kristensen, A. Rubano, S. Golowich, L. Marrucci, and S. Ramachandran, “Spin-Orbit Coupled, Non-Integer OAM Fibers: Unlocking a New Eigenbasis for Transmitting 24 Uncoupled Modes,” in *Conference on Lasers and Electro-Optics,* (OSA, Washington, D.C., 2016), p. JTh4C.7.

[40] L. Marrucci, C. Manzo, and D. Paparo, “Optical spin-to-orbital angular momentum conversion in inhomogeneous anisotropic media,” Physical Review Letters **96**, 1–4 (2006).

[41] M. a. Bandres and J. C. Gutiérrez-Vega, “Circular beams.” Optics letters **33**, 177–179 (2008).

[42] G. Vallone, “On the properties of circular beams: normalization, Laguerre–Gauss expansion, and free-space divergence,” Optics Letters **40**, 1717 (2015).

[43] J. Goodman, *Introduction to Fourier Optics* (Roberts & Company, 2005), 3rd ed.

[44] R. C. Jones, “A New Calculus for the Treatment of Optical SystemsI Description and Discussion of the Calculus,” Journal of the Optical Society of America **31**, 488 (1941).

[45] D. G. Voelz, *Computational Fourier Optics: A MATLAB Tutorial* (SPIE, 2011).

[46] M. Nakazawa, M. Yoshida, and T. Hirooka, “Nondestructive measurement of mode couplings along a multi-core fiber using a synchronous multi-channel OTDR,” Optics Express **20**, 12530 (2012).

[47] J. W. Nicholson, A. D. Yablon, S. Ramachandran, and S. Ghalmi, “Spatially and spectrally resolved imaging of modal content in large-mode-area fibers,” Optics Express **16**, 7233 (2008).

[48] D. N. Schimpf, R. a. Barankov, and S. Ramachandran, “Cross-correlated (Cˆ2) imaging of fiber and waveguide modes,” Optics Express **19**, 13008 (2011).

[49] J. Demas and S. Ramachandran, “Sub-second mode measurement of fibers using Cˆ2 imaging,” Optics Express **22**, 23043 (2014).

[50] K. Ingerslev, P. Gregg, M. Galili, F. Da Ros, H. Hu, F. Bao, M. A. U. Castaneda, P. Kristensen, A. Rubano, L. Marrucci, S. Ramachandran, K. Rottwitt, T. Morioka, and L. K. Oxenløwe, “12 Mode, MIMO-Free OAM Transmission,” in *Optical Fiber Communication Conference,* (OSA, Washington, D.C., 2017), p. M2D.1.

[51] K. Ingerslev, P. Gregg, M. Galili, F. Da Ros, H. Hu, F. Bao, M. A. Usuga Castaneda, P. Kristensen, A. Rubano, L. Marrucci, K. Rottwitt, T. Morioka, S. Ramachandran, and L. K. Oxenløwe, “12 mode, WDM, MIMO-free orbital angular momentum transmission,” Optics Express **26**, 20225 (2018).

[52] N. K. Fontaine, R. Ryf, H. Chen, A. V. Benitez, J. E. Antonio Lopez, R. A. Correa, B. Guan, B. Ercan, R. P. Scott, S. J. Ben Yoo, L. Grüner-Nielsen, Y. Sun, and R. J. Lingle, “30x30 MIMO Transmission over 15 Spatial Modes,” in *Optical Fiber Communication Conference Post Deadline Papers,* (OSA, Washington, D.C., 2015), 1, p. Th5C.1.

[53] F. Feng, X. Jin, D. O’Brien, F. Payne, Y.-m. Jung, Q. Kang, P. Barua, J. K. Sahu, S.-U. Alam, D. J. Richardson, and T. D. Wilkinson, “All-optical mode-group multiplexed transmission over a graded-index ring-core fiber with single radial mode,” Optics Express **25**, 13773 (2017).

[54] J. Carpenter, B. C. Thomsen, and T. D. Wilkinson, “Degenerate Mode-Group Division Multiplexing,” Journal of Lightwave Technology **30**, 3946–3952 (2012).

[55] G. Zhu, Z. Hu, X. Wu, C. Du, W. Luo, Y. Chen, X. Cai, J. Liu, J. Zhu, and S. Yu, "Scalable mode division multiplexed transmission over a 10-km ring-core fiber using high-order orbital angular momentum modes," Optics Express **26**, 594 (2018).

[56] L. Wang, P. Vaity, S. Chatigny, Y. Messaddeq, L. A. Rusch, and S. LaRochelle, "Orbital-Angular-Momentum Polarization Mode Dispersion in Optical Fibers," Journal of Lightwave Technology **34**, 1661–1671 (2016).

[57] R. Maruyama, N. Kuwaki, S. Matsuo, and M. Ohashi, "Experimental Investigation of Relation Between Mode-Coupling and Fiber Characteristics in Few-Mode Fibers," in *Optical Fiber Communication Conference,* (OSA, Washington, D.C., 2015), p. M2C.1.

[58] X. Wang, S. Yan, J. Zhu, Y. Ou, Z. Hu, Y. Messaddeq, S. LaRochelle, L. A. Rusch, D. Simeonidou, and S. Yu, "3.36-Tbit/s OAM and Wavelength Multiplexed Transmission over an Inverse-Parabolic Graded Index Fiber," in *Conference on Lasers and Electro-Optics,* (OSA, Washington, D.C., 2017), p. SW4I.3.

[59] G. Labroille, B. Denolle, P. Jian, P. Genevaux, N. Treps, and J.-F. Morizur, "Efficient and mode selective spatial mode multiplexer based on multi-plane light conversion," Optics Express **22**, 15599 (2014).

[60] Z. S. Eznaveh, J. C. Alvarado Zacarias, J. E. Antonio Lopez, Y.-m. Jung, K. Shi, B. C. Thomsen, D. J. Richardson, S. Leon-Saval, and R. A. Correa, "Annular Core Photonic Lantern OAM Mode Multiplexer," in *Optical Fiber Communication Conference,* vol. 1 (OSA, Washington, D.C., 2017), p. Tu3J.3.

[61] Y. Jung, E. L. Lim, Q. Kang, T. C. May-Smith, N. H. L. Wong, R. Standish, F. Poletti, J. K. Sahu, S. U. Alam, and D. J. Richardson, "Cladding pumped few-mode EDFA for mode division multiplexed transmission," Optics Express **22**, 29008 (2014).

[62] Q. Kang, P. Gregg, Y. Jung, E. L. Lim, S.-u. Alam, S. Ramachandran, and D. J. Richardson, "Amplification of 12 OAM Modes in an air-core erbium doped fiber," Optics Express **23**, 28341 (2015).

[63] Y. Jung, Q. Kang, S. Yoo, R. Sidharthan, D. Ho, P. Gregg, S. Ramachandran, S. Alam, and D. Richardson, "Optical Orbital Angular Momentum Amplifier based on an Air-Core Erbium Doped Fiber," in *Optical Fiber Communication Conference Postdeadline Papers,* (OSA, Washington, D.C., 2016), 1, p. Th5A.5.

[64] M. D. Turner, T. M. Monro, and S. Afshar V., "A full vectorial model for pulse propagation in emerging waveguides with subwavelength structures part II: Stimulated Raman Scattering," Optics Express **17**, 11565 (2009).

[65] J. Bromage, "Raman Amplification for Fiber Communications Systems," Journal of Lightwave Technology **22**, 79–93 (2004).

[66] S. Afshar V. and T. M. Monro, "A full vectorial model for pulse propagation in emerging waveguides with subwavelength structures part I: Kerr nonlinearity," Optics Express **17**, 2298 (2009).

[67] Y. Y. Huang, A. Sarkar, and P. C. Schultz, “Relationship between composition, density and refractive index for germania silica glasses,” Journal of Non-Crystalline Solids **27**, 29–37 (1978).

[68] S. Davey, D. Williams, B. Ainslie, W. Rothwell, and B. Wakefield, “Optical gain spectrum of GeO2-SiO2 Raman fibre amplifiers,” IEE Proceedings J Optoelectronics **136**, 301 (1989).

[69] J. Bromage, K. Rottwitt, and M. Lines, “A method to predict the Raman gain spectra of germanosilicate fibers with arbitrary index profiles,” IEEE Photonics Technology Letters **14**, 24–26 (2002).

[70] K. Ingerslev, P. Gregg, M. Galili, P. Kristensen, S. Ramachandran, K. Rottwitt, T. Morioka, and L. K. Oxenlowe, “Raman amplification of OAM modes,” in *2017 Conference on Lasers and Electro-Optics Europe & European Quantum Electronics Conference (CLEO/Europe-EQEC),* (IEEE, 2017), pp. 1–1.

[71] K. Ingerslev, P. Gregg, M. Galili, P. Kristensen, S. Ramachandran, K. Rottwitt, T. Morioka, and L. K. Oxenlowe, “Raman amplification of OAM modes,” in *4th International Conference on Optical Angular Momentum (ICOAM 2017),* (2017).

[72] K. Ingerslev, G. Rademacher, R. S. Luis, B. J. Puttnam, W. Klaus, S. Shinada, Y. Awaji, K. Rottwitt, T. Morioka, L. K. Oxenløwe, and N. Wada, “Free-Space Few-Mode Kramers-Kronig Receiver,” in *Photonics in Switching and Computing (PSC) 2018,* (2018).

[73] K. Ingerslev, G. Rademacher, R. S. Luis, B. J. Puttnam, W. Klaus, T. A. Eriksson, S. Shinada, Y. Awaji, R. Maruyama, K. Aikawa, T. Morioka, and N. Wada, “A Scalable SDM Receiver Enabled by Few-Mode Domain Spectral Filtering and LO-Signal Mixing,” in *(Submitted to) Optical Fiber Communication Conference,* (Unpublished, 2019).

[74] J. Sakaguchi, W. Klaus, B. J. Puttnam, J. M. D. Mendinueta, Y. Awaji, N. Wada, Y. Tsuchida, K. Maeda, M. Tadakuma, K. Imamura, R. Sugizaki, T. Kobayashi, Y. Tottori, M. Watanabe, and R. V. Jensen, “19-core MCF transmission system using EDFA with shared core pumping coupled via free-space optics,” Optics Express **22**, 90 (2014).

[75] J. Salazar-Gil, R. Lingle, R. Ryf, Chang Liu, S. Leon-Saval, Y. Sun, S. Chandrasekhar, J. Bland-Hawthorn, B. Ercan, D. Sinefeld, S. Randel, M. Montoliu, A. Gnauck, M. Esmaeelpour, D. Marom, M. Blau, J. Dunayevsky, N. Fontaine, and L. Gruner-Nielsen, “Wavelength-selective Switch for Few-mode Fiber Transmission,” in *39th European Conference and Exhibition on Optical Communication (ECOC 2013),* (Institution of Engineering and Technology, 2013), 1, pp. 1224–1226.

[76] R. S. Luís, G. Rademacher, B. J. Puttnam, S. Shinada, H. Furukawa, R. Maruyama, K. Aikawa, and N. Wada, “A Coherent Kramers-Kronig Receiver for 3-Mode Few-Mode Fiber Transmission,” in *44th European Conference On Optical Communication (ECOC),* (2018), p. Mo3F.3.

[77] A. Mecozzi, C. Antonelli, and M. Shtaif, “Kramers–Kronig coherent receiver,” Optica **3**, 1220 (2016).

[78] C. Antonelli, A. Mecozzi, M. Shtaif, X. Chen, S. Chandrasekhar, and P. J. Winzer, “Polarization Multiplexing With the Kramers-Kronig Receiver,” Journal of Lightwave Technology **35**, 5418–5424 (2017).

[79] R. Maruyama, N. Kuwaki, S. Matsuo, and M. Ohashi, “Two mode optical fibers with low and flattened differential modal delay suitable for WDM-MIMO combined system,” Optics Express **22**, 14311 (2014).

[80] G. Rademacher, R. S. Luís, B. J. Puttnam, T. A. Eriksson, E. Agrell, R. Maruyama, K. Aikawa, H. Furukawa, Y. Awaji, and N. Wada, “159 Tbit/s C+L Band Transmission over 1045 km 3-Mode Graded-Index Few-Mode Fiber,” in *Optical Fiber Communication Conference Postdeadline Papers,* (OSA, Washington, D.C., 2018), 1, p. Th4C.4.

[81] G. Rademacher, R. Ryf, N. K. Fontaine, H. Chen, R.-J. Essiambre, B. J. Puttnam, R. S. Luis, Y. Awaji, N. Wada, S. Gross, N. Riesen, M. Withford, Y. Sun, and R. Lingle, “Long-Haul Transmission Over Few-Mode Fibers With Space-Division Multiplexing,” Journal of Lightwave Technology **36**, 1382–1388 (2018).

[82] A. Alvarado, E. Agrell, D. Lavery, R. Maher, and P. Bayvel, “Replacing the Soft-Decision FEC Limit Paradigm in the Design of Optical Communication Systems,” Journal of Lightwave Technology **34**, 707–721 (2016).

[83] Eur. Standard ETSI EN 302 307 V1.2.1, “Digital Video Broadcasting (DVB); Second generation framing structure, channel coding and modulation systems for Broadcasting, Interactive Services, News Gathering and other broadband satellite applications (DVB-S2),” (2009).

[84] I. C. Society, “IEEE standard for Ethernet,” (2016).